# Ferromagnetic/antiferromagnetic exchange bias nanostructures for ultimate spintronic devices

Kamil Akmaldinov

## To cite this version:

Kamil Akmaldinov. Ferromagnetic/antiferromagnetic exchange bias nanostructures for ultimate spintronic devices. Condensed Matter [cond-mat]. Université Grenoble Alpes, 2015. English. NNT : 2015GREAY009 . tel-01161786

HAL Id: tel-01161786
https://theses.hal.science/tel-01161786
Submitted on 9 Jun 2015

UNIVERSITÉ DE GRENOBLE

# THÈSE

Pour obtenir le grade de

## DOCTEUR DE L'UNIVERSITÉ DE GRENOBLE

Spécialité : **Physique**

Arrêté ministériel : 7 août 2006

Présentée par

## Kamil AKMALDINOV

Thèse dirigée par **Vincent BALTZ**
codirigée par **Bernard DIENY**

préparée au sein du **Laboratoire SPINTEC**
et de la société **Crocus Technology**
dans **l'École Doctorale de Physique de Grenoble**

# Ferromagnetic/antiferromagnetic exchange bias nanostructures for ultimate spintronic devices

Thèse soutenue publiquement le **6 février 2015**,
devant le jury composé de :

**M. Manuel BIBES**
Directeur de recherche du CNRS, Rapporteur
**M. Robert STAMPS**
Professeur de l'Université de Glasgow, Rapporteur
**M. Olivier BOURGEOIS**
Directeur de recherche du CNRS, Membre
**M. Luc LECHEVALLIER**
Maître de conférences de l'Université de Cergy-Pontoise, Membre
**Mme Clarisse DUCRUET**
Ingénieur R&D chez Crocus Technology, Membre
**M. Vincent BALTZ**
Chargé de recherche du CNRS, Membre

*Université Joseph Fourier / Université Pierre Mendès France / Université Stendhal / Université de Savoie / Grenoble INP*

# Contents

# INTRODUCTION

The research presented here is focused on ferromagnetic/antiferromagnetic (F/AF) exchange bias (EB) nanostructures for ultimate spintronics devices and more specifically for the improvement of thermally-assisted random access memories (TA-MRAM) now developed by the CROCUS technology company. It was conducted within the SPINTEC laboratory (spintronics and technology of compounds), joint research unit between French institutions: University of Grenoble Alpes, CNRS, CEA (INAC) in the frame of a joint research and development program between the CROCUS technology company and the SPINTEC laboratory. Such a program financially supported this PhD thesis under a CIFRE grant (*Convention Industrielle de Formation par la REcherche*).

Basically, a MRAM comprises a magnetic tunnel junction, an exchange biased reference layer and a storage layer. The specificity of a TA-MRAM is that the storage layer is also exchange biased for improved data retention. The bit writing scheme of every memory cell involves additional heating to temporarily unblock the exchange bias coupling between the F and AF stacks of the storage layer. To ensure stable device functioning and to compete with other memory types the memory cell to memory cell parameters dispersion such as the exchange bias loop shift and the write power should be as low as possible. It is well-known, that EB can be strongly affected by diverse external conditions - from the deposition rates and layers thicknesses to annealing temperatures and fields. It becomes even more critical when talking about nano-dimensional structures, where the shape and the size of a bit also matters. No doubts, all these parameters should be taken into account to control the variability and in the literature there are numerous studies focused on shape, growth and fabrication reasons for cells dispersions. Apart from that, it is widely recognised that EB is strongly dependent on the F-AF interfacial quality and in particular on the amount of highly unstable regions - spin-glass like phases. It was supposed few years ago that randomly spread spin-glass like phases at the F/AF interface or within the bulk of the AF layer significantly contribute to the distributions of EB properties in devices after processing. This PhD thesis aimed at factually addressing this point. The manuscript is therefore structured as follows:

Chapter 1 introduces the exchange bias phenomenology and state-of-art. It covers early theoretical suggestions considering ideal systems and to more complicated systems accounting for interfacial spin-glass like phases. It continues with the description of nowadays macroscopic picture based on both experimental findings and theoretical view.

The latter assumes a granular model coupled to F/AF spin-glass like phases and will be used throughout. Finally, and given the description of today's macroscopic view, this chapter ends with a paragraph about the recent way proposed to quantify spin-glass like phases via bimodal blocking temperature distributions.

Chapter 2 first introduces to the reader some of the basic principles in use in spintronics devices such as giant- and tunnel magnetoresistance and spin transfer torque. In a second step devices employing the EB phenomenon are described. In particular, the chapter ends with a focus on TA-MRAM devices and sets the issues to be addressed in the frame of this PhD thesis: i) better understanding and finding ways to tune the amount of F/AF spin-glass like phases and ii) factually comparing the amount of spin-glasses spread over F/AF thin films and bit-cell dispersions of EB in corresponding TA-MRAM.

Chapter 3 therefore studies the origin of the spin-glass like regions and more specifically the role of Mn-diffusion. First, in collaboration with the 'groupe de physique des matériaux' (GPM) of Rouen, atom probe microscopy was used for direct inspection of the spatial distribution of species in the stack. This work was the object of a publication: Ref. [1]. Then, we report a study where barriers to limit Mn-diffusion were used and significantly affected the amount of spin-glass like phases. This last part was dealt with in Ref. [2].

Chapter 4 is focused on the insights of spin-glass like phases for applications. On the one hand, it shows the use of composite AF materials to respond to an industrial need and in particular to provide an ideal material for a TA-MRAM storage layer with better stability than FeMn at rest temperature but requiring less write power consumption than IrMn. In addition to showing the potential benefits of employing such composite materials for applications it is yet another way to tune the amount of spin-glass like phases. This part was the object of Ref. [3]. In the second part of this chapter, we factually prove that spin-glass-like phases spread over the F/AF storage layer are the main cause of bit-distributions once the film is nanofabricated into 1kb TA-MRAM device. This last part will be reported in Ref. [4].

Although defined in the text, the acronyms and abbreviations are reminded at the end in the glossary. Finally, preliminary works also dealt with in the frame of the present PhD thesis are shown in the appendices: 1 - use of single barrier to Mn-diffusion, 2 - tuning the interface vs volume contributions via ion irradiations and 3 - comparing blocking temperature distributions and x- ray dichroism results.

.

# Chapter 1.

# Introduction to ferromagnetic / antiferromagnetic exchange bias

In this chapter the phenomenology as well as selected theoretical models describing exchange bias are first discussed. They are useful for the further understanding of today's macroscopic view that is described in a second step and then used throughout the manuscript. Given today's macroscopic view, the distributions of blocking temperatures and in particular the recent way to measure these latter and thus to quantify F/AF spin-glass like phases is extensively described.

## 1.1. Exchange bias phenomenology

### 1.1.1. Discovery

In 1956 Meiklejohn and Bean [5], discovered the exchange anisotropy, more often referred to as exchange bias (EB). The effect arises from the coupling between the ferromagnetic (F) and antiferromagnetic (AF) spins at the interface. It results in a shift of the F hysteresis loop along the magnetic field axis with respect to the applied magnetic field. Figure 1.1 shows Meiklejohn and Bean's original finding. Note already that when the coercive field is larger than the hysteresis loop shift, the F magnetization will return to a fixed direction at remanence. EB thus sets a reference direction. Using a torque magnetometer Meiklejohn and Bean have also shown that EB relates to unidirectional anisotropy, as shown in Figure 1.2.

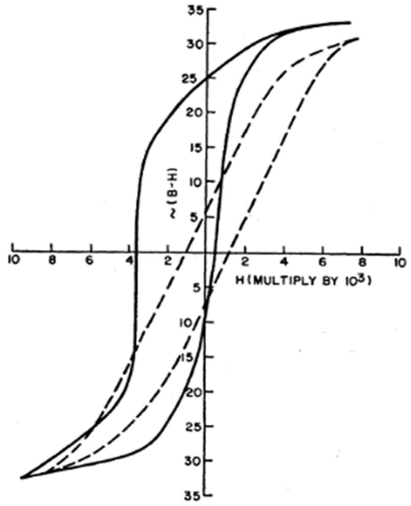

**Figure 1.1**

*Hysteresis loops for oxide-coated Co particles measured at 77K. Dashed and solid line correspond to zero-field cooled (ZFC) and field-cooled (FC) measurements respectively. After* [5]

Actually, Meiklejohn and Bean were studying oxidized Co particles with a diameter of 100 nm and cooled through the Néel Temperature ($T_N$) in the presence of a saturating magnetic field. The Néel temperature is the critical temperature above which the magnetic state of a material transits from AF to paramagnetic. It is intrinsic to the AF and relates to the AF-AF exchange stiffness. Note already that EB is temperature dependent and vanishes at $T_N$. Actually it vanishes at a lower temperature usually referred to as blocking temperature ($T_B$). This latter is linked to F/AF interactions and it is the temperature above which an AF grain is no more stable (i.e. no more pinned) when cycling the F magnetization. $T_B$ not only relates to the F-AF interfacial exchange stiffness but also to the AF grain core properties like the AF grain anisotropy energy: KV, where K and V are the AF anisotropy and volume, respectively. Given that, $T_B$ is also influenced by size effects via V, thus resulting in $T_B$ distributions for polycrystalline films due to grains sizes dispersions. We will further see that $T_B$ distributions provide many more information than simply the grains sizes distribution. Prior to that, we will explain in the next paragraph how to set EB for the simple case of a single grain.

### 1.1.2. Setting exchange bias

Figure 1.2 represents 3 distinct magnetic configurations with a corresponding torque (top row) and a hysteresis loop (middle row). The first column (a - b) shows a typical hysteresis loop for a single F slab: symmetric with respect to the origin of the axes. Two stable remanence states evidence the presence of uniaxial anisotropy. That is confirmed by torque measurements which obey a sin(2ϕ) law, ϕ – being the angle between magnetization and applied field. The origin of such magneto-crystalline anisotropy primarily arises from spin-orbit interaction (Note that this is not the single mechanism responsible for the anisotropy formation, some of them will be discussed lately in present manuscript). In Figure 1.2 (c-d), the AF layer is now in contact with F layer without any (neither magnetic nor temperature) treatments. The corresponding hysteresis loop is wider and the torque has a higher amplitude. That translates in $H_C$ and anisotropy increment respectively. The above described changes arise from the interaction between the F and AF materials.

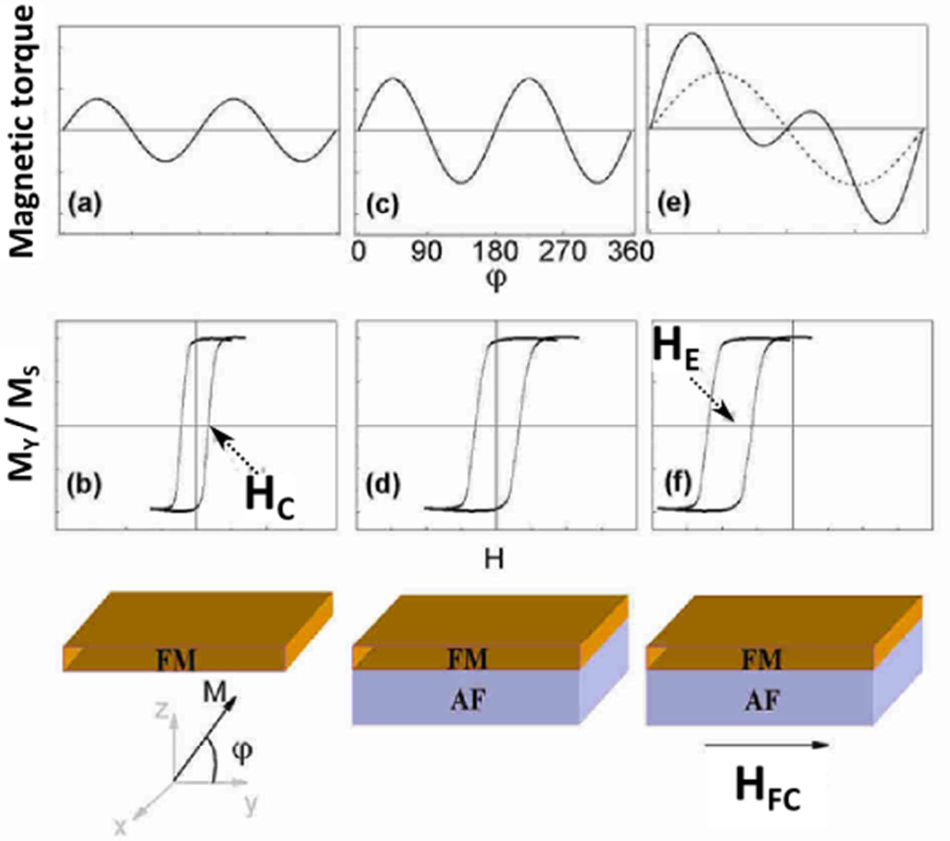

**Figure 1.2**

*Schematic representation of the F-AF system evolution from single F-material (a-b), through intermediate state when the AF is in contact with the F (c-d), and then to the exchange biased sandwich after FC across $T_B$ (e-f). Adapted from* [6], [15].

Figure 1.2 (e-f) shows how the system evolved from an ‘as-deposited’ to a FC state (c-d). Indeed, after cooling the system from above the blocking temperature with an applied field the loop shifts and loses its symmetry with respect to the origin of the axes. The torque curve switches from a sin(2ϕ) behaviour to a sin(ϕ) character. This is caused by a new energy term, favouring only one preferred magnetization direction in the F-layer thus bringing to the system a new “unidirectional” anisotropy.This brief description was aimed to point out some basic peculiarities of magnetization process occurring with F/AF sandwiches and the necessary conditions to set up a unidirectional anisotropy. More details will be discussed lately.

In Figure 1.3 the intuitive picture of the establishment of EB and of the loop shift mechanism are shown schematically. The top sketch demonstrates the initial state of the system (left) with the AF material in the paramagnetic state due to the T, higher than its ordering temperature ($T_N$). The transition from this state takes place once the system is cooled down though this temperature with an applied magnetic field. Due to the interfacial interactions AF spins adopt F-layer spins orientation. The neighbouring spin lattices follow the interfacial pattern in a way to produce zero bulk magnetization, i.e. with staggered orientations, see Figure 1.3(1). This configuration also corresponds to the saturation curve on the hysteresis loop. Cycling the field for this structure, at the point where it changes sign (2) the F-spins start to rotate, whereas with a sufficiently large anisotropy AF spins remain stable. Because of the interactions between AF and F spins at the interface the latter experience a torque from the former spins, trying to keep them in initial position (3). Exactly this interfacial interaction establishes the unidirectional anisotropy, favouring F-spins to be aligned in one single direction. Finally, when the applied field is strong enough to counteract the anisotropy – the F-layer is reversed (4). Note that, if the AF anisotropy is sufficiently weak, the $H_C$ increase effect will be observed only, with no loop shift, similarly to Figure 1.2 (c-d).

Also note that the above picture is intuitive and that reality goes beyond that, as we will discuss later. In particular, in order to set EB, it is not necessary to reach $T_N$. Breaking the F/AF interaction by raising the temperature up to $T_B$ is enough. After FC, the AF is not perfectly staggered but accommodates the F/AF interaction and the spin frustrations introduced by defects as will be detailed later (roughness, grain boundaries, etc.)

Despite the simplicity of this phenomenological explanation, it is hard to draw an accurate and universal picture. In the following sections the state-of-art from early suggestions to nowadays model will be discussed.

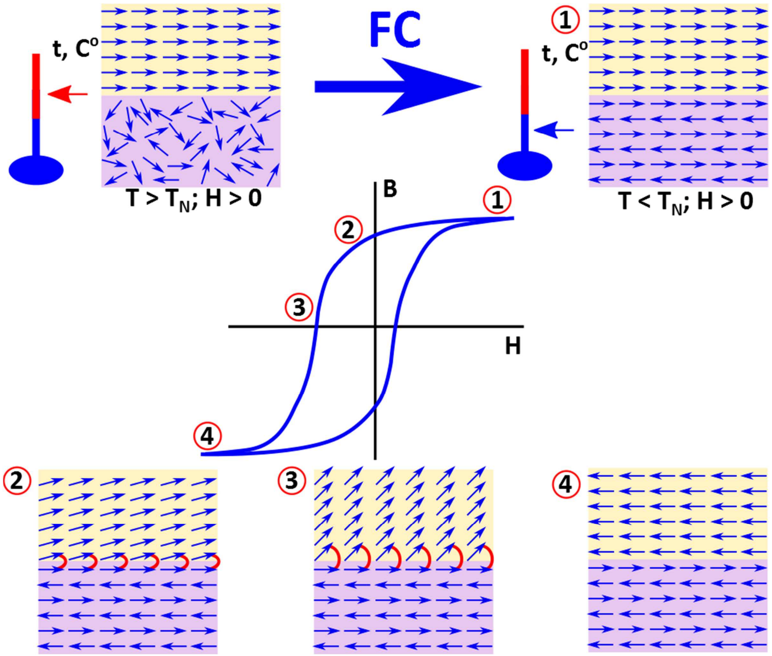

**Figure 1.3**

*Schematic diagram of the F and AF moments during field cooling and then at different steps of the hysteresis loop.*

## 1.2. Theoretical models

### 1.2.1. Meikeljohn and Bean intuitive picture

In their early and intuitive model Meikeljohn and Bean [7] considered coherent rotation of two coupled macrospins describing the F layer and the AF uncompensated layer. Based on that, the following equation for the energy per unit area could be written:

$$\varepsilon = -HM_F t_F \cos(\theta - \beta) + K_F t_F sin^2(\beta) + K_{AF} t_{AF} sin^2(\alpha) - J_{F/AF}\cos(\beta - \alpha) \tag{1.1}$$

where H is the applied magnetic field, $M_F$ is the saturation magnetization in the F, $t_F$ and $t_{AF}$ are the thicknesses of the F and AF layers, $K_F$ and $K_{AF}$ are the magnetic anisotropies in the F and the AF and $J_{F/AF}$ is the exchange coupling constant at the interface, $\alpha$, $\beta$ and $\theta$ are the angles between the spins in the AF and the AF easy axis (see Figure 1.4), the direction of the spins in the F and the F easy axis and the direction of H and the F easy axis, respectively, as shown in Figure 1.4.

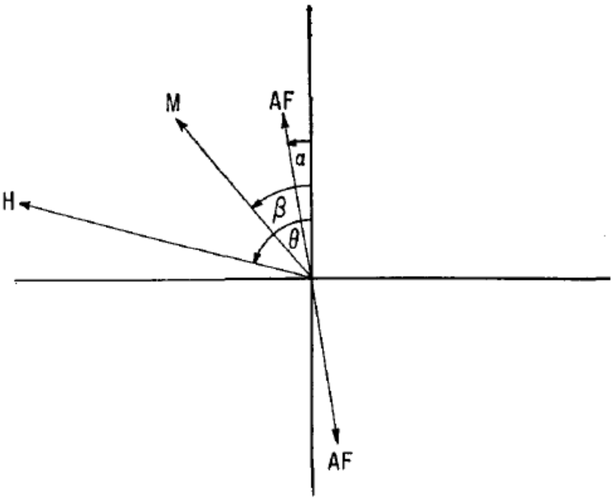

**Figure 1.4**

*Scheme introducing the important parameters introduced in the model of Meiklejohn and Bean. After* [8].

By considering that the AF anisotropy is large compared to the F one $K_F << K_{AF}$, the AF spins will remain fixed meaning that $\alpha \approx 0$ and $\sin\alpha \approx 0$. Taking the energy partial derivatives with respect to angles α and β, the exchange bias field writes:

$$H_E = -\frac{J_{F/AF}}{\mu_0 M_F t_F} \tag{1.2}$$

The above equation qualitatively reflects the magnetic behaviour, but quantitatively it is orders of magnitude larger than experiments. Despite that the Meiklejohn and Bean's model correctly predicts the sign of the exchange bias field. In addition, there is very important result hidden in the denominator of Equation (1.2) since $H_E$ obey the ratio $(1/t_F)$ (for instance [9–11]), that gives the clue about interfacial origin of the effect [12] and which is proven in many experimental investigations. This question will be considered in details in Section 1.2.4.

As an implement and based on this previous intuitive model, Meiklejohn later considered a finite AF anisotropy, since this could explanation the rotational hysteresis observed in torque measurements. He found that EB occurs when $K_{AF}t_{AF}/J_{F/AF}\geq 1$ meaning that the AF remains still rigid when the F is cycled. Else, if $K_{AF}t_{AF}/J_{F/AF}<1$ the AF spins follow the F magnetization reversal. As a consequence, the loop shift is zero and an increase of coercivity is observed. Although resulting from a toy-model, this shows that the AF (or an AF grain/domain) can be dragged by the F reversal depending on the relative strength of the inner AF energy $K_{AF}t_{AF}$ and the F/AF interfacial coupling. As a consequence of this funding, we understand that for a given $J_{F/AF}$, a thicker AF will be more stable over the F magnetization reversal. We will reuse these notions later on when discussing blocking temperature and blocking temperature distributions.

Meiklejohn and Bean's macroscopic and qualitative approach underlines the necessity of AF interfacial uncompensated magnetization for EB. It probably lacks a mesoscopic and microscopic level interpretations. In the following, we will discuss some of the theories taking into account such considerations.

### 1.2.2. Néel/Mauri domain wall model

In an attempt to reduce the theoretical value of hysteresis loop shift, Néel implemented the Meiklejohn and Bean's theoretical approach by introducing the concept of a planar domain wall forming during the magnetization reversal, rather than a coherent rotation. Basically, the AF domain wall will store a fraction of the exchange coupling energy and the exchange bias field will be reduced. Néel obtained a differential equation that gave a picture of the magnetization profile in the AF:

$$JS^2\frac{d^2\theta}{di^2} - 4K\sin\theta = 0 \tag{1.3}$$

where θ is the angle between m and the easy axes, and J and K are the interfacial exchange constant and anisotropy energy, respectively. His study mostly suffers from the fact that the thickness of the layers should be at least about hundreds of nanometers, therefore it could not explain the phenomena in thin films. Later, Mauri [13] completed this idea of a domain wall forming in the AF when cycling the F magnetization.

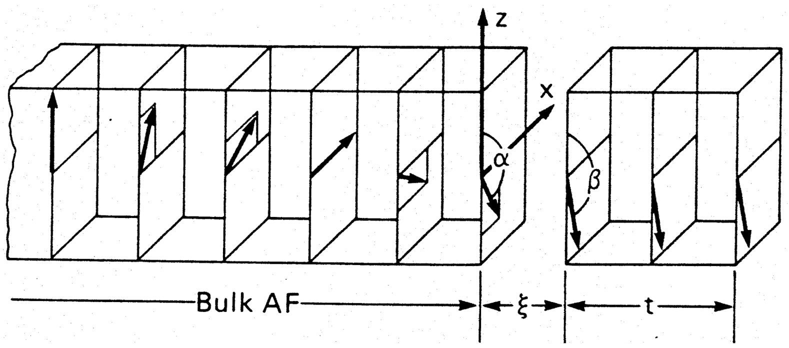

**Figure 1.5**

*Sketched representation of a DW formation in the AF according to the model of Mauri model* [13].

As illustrated in Figure 1.5, in his approximation the domain wall (DW) formation caused by the magnetization reversal of the F layer is considered in the vicinity of the F/AF interface. Focusing on the DW in the AF layer Mauri first studied the energy of the wall: $2\sqrt{A_{AF}K_{AF}}$ with $A_{AF}$ and $K_{AF}$ the AF exchange stiffness and anisotropy, respectively and he derived the following total magnetic energy:

$$\delta = 2\sqrt{A_{AF}\,K_{AF}}(1-\ \cos\alpha) + A_{12}/\xi[1-\cos(\alpha-\beta)] \\ + K_F t\cos^2(\alpha-\beta) + HM(1-\cos\beta) \tag{1.4}$$

where $K_F$, and M are the anisotropy and magnetization of the F layer; α, β are the angles between the AF anisotropy axis (z axis) and the AF and F magnetization respectively. At a distance ξ from the interface, a F of thickness t follows the AF rotation. The first term reflects the AF DW energy term, the second is the F/AF exchange energy, the third corresponds to the F anisotropy energy and the last accounts for the magnetostatic energy. The previous equation can be rewritten in units of domain wall energy per unit surface ($2\sqrt{A_{AF}K_{AF}}$):

$$\delta = (1-\cos\alpha) + \lambda[1-\ \cos(\alpha-\beta)] + \mu\cos^2\beta + k(1-\cos\beta) \tag{1.5}$$

with

$$\lambda = \frac{A_{12}}{\xi 2\sqrt{A_{AF}K_{AF}}} = \frac{J_{F/AF}}{2a\sqrt{A_{AF}K_{AF}}} \tag{1.6}$$

The latest equation for λ reflects a very intuitive physical picture since it is a proportion between interfacial energy and AF stiffness, i.e. the influence of F torque experienced by AF layer. Therefore Mauri acknowledges two possible situations: i) a weak coupling ($\lambda << 1$) that does not involve DW creation because $J_{ex} << \sqrt{A_{AF}K_{AF}}$ thus giving very limited values for $H_E$; and ii) a strong coupling ($\lambda >> 1$) resulting in a 180° DW in the AF. Accordingly, the two following exchange values can be calculated for strong and weak coupling respectively:

$$\begin{gathered}\text{for}\,\lambda \ll 1, \qquad H_E = -2\left(\frac{\sqrt{A_{AF}K_{AF}}}{M_S t_{FM}}\right) \\ \text{for}\,\lambda \gg 1, \qquad H_E = -\left(\frac{J_{F/AF}}{M_S t_{FM}}\right)\end{gathered} \tag{1.7}$$

To summarize, the Néel/Mauri concept predicts more reasonable values for EB when the AF layer is thick enough. The main drawbacks of this model are: 1) the formation of AF DW is subject to strong coupling and to weak AF anisotropy for AF domain wall formation, otherwise it would be more energetically favourable to form domain walls in the F layer; 2) the interface is supposed to be ideal; 3) the model does not explain $H_C$ enhancement. In practice, some F/AF bilayers meet all the criteria to form exchange springs in the AFM and this was observed experimentally, for example in Co/NiO bilayers. It is important to note that the Néel/Mauri model introduces the concept of AF reconfiguration over F magnetization reversal and this will be used in the forthcoming chapters.

### 1.2.3. Magnetic frustrations: Malozemoff's random field and Takano models

In addition to the above mentioned magnetic reconfiguration, on a microscopic scale the exchange anisotropy depends on a large number of parameters. In particular some models among which the Malozemoff's [14] random field model and Takano model evidenced the role of magnetic frustrations and we will now deal with such models. The role of such frustrations is significant and part of my PhD thesis work will show quantitative measurements of that.

Contrary to the previously discussed models assuming perfectly smooth interfaces at the atomic level, the theory developed by Malozemoff takes into account a more realistic situation. For example, numerous experimental studies use sputtered stacks, with a non-zero roughness due to the deposition process. Examples of defects due to roughness and of the subsequent magnetic frustrations are depicted in Figure 1.6.

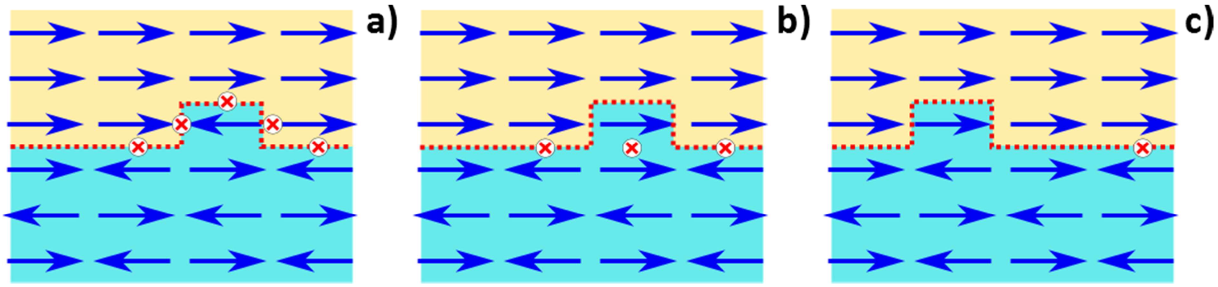

**Figure 1.6**

*Schematic side view representation of possible interfacial spins frustrations for F/AF sandwiches. Adapted from* [14]

Malozemoff used the notion of interfacial random-field as an explanation for the exchange anisotropy in this case. He argued that the roughness generates random field acting from the F layer onto the AF layer. If a domain wall in the F propagates under an external magnetic field, and if the interfacial energy in one AF region (σ1) is not the same as the interfacial energy in the neighbouring AF region (σ2), then the exchange bias field can be calculated by the equilibrium condition between the interfacial energy difference Δσ and the applied field pressure $2HM_Ft_F$ [14]:

$$H_E = {}^{\Delta\sigma}/_{2M_Ft_F} \tag{1.8}$$

In fact, due to the presence of atomic scale randomness of the interface and to the concomitant magnetic frustrations, it is more energetically favourable for the AF layer to break up into domains in order to minimize the net random unidirectional interfacial anisotropy. As a result a perpendicular domain wall is permanently formed in the interface and in the bulk AF, see Figure 1.7. This contrasts with the previously discussed models with in-plane and reversible domain walls.

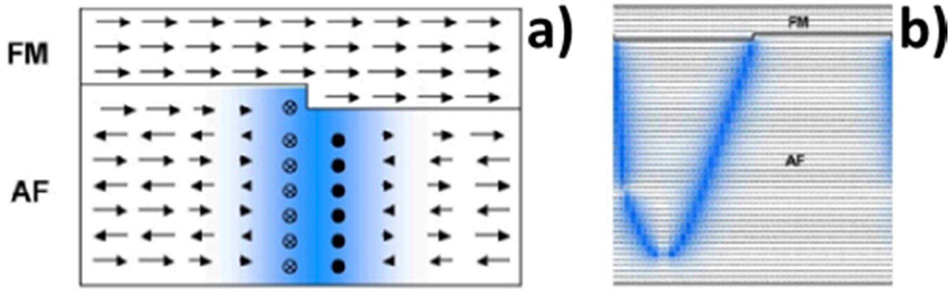

**Figure 1.7**

*(a) Formation of an AF-domain wall due to an atomic step at the F/AF interface andresponsible for geometrical-induced spin frustration. (b) More realistic bubble like domain wall. After* [15]

The Malozemoff's random field model shows the influence of spin-glasses on EB since magnetic frustrations resulting from atomic steps lead to AF domain walls. In some implementations it leads to AF bubbles as shown in Figure 1.7b). Apart from roughness (atomic steps), other sources of magnetic frustrations such as interfacial and core stacking faults are taken into account in other models such as the domain state model by Nowak et al [16]. The idea of such spin-glass like phases influencing exchange bias was actually early pointed out by Takano and Berkowitz [17] who also observed and modelled this effect. Such studies are briefly evoked below. We will see later on that such spin-glass like phases play an important role in the macroscopic model that we will further describe and use to interpret our findings. In addition, Takano extended the notion of spin-glasses to the case of polycrystalline films. He claimed that EB and in particular for NiFe/CoO bilayers arises from uncompensated interfacial AF spins, that result from interfacial frustrations that lead to spin-glass like phases. Let's first describe his experimental result. Figure 1.8 shows the thermoremanent magnetization (TRM) signal for field cooled (FC) and (ZFC) zero field cooled CoO/MgO multilayers. For the FC curve two distinct regions should be distinguished. First, a "plateau" between 50K and 200K where the magnetization does not depend on temperature. And second, for T < 50K, where a peak is observed. The magnitudes of these two scales are independent on CoO thickness, while the effect is higher with increasing number of repetitions. This observation evidences that the effect is coming from the interface, rather than from the bulk of the AF. Additionally, when the sample was cooled down to 100K in the presence of field, and further cooled to 10K without external field, the low-T peak disappears. The latest statement postulates that for the alignment of low-T spins responsible for the increase, a moderate FC is required below 100K. The authors suppose that a part of interfacial spins responsible for the increase at low-T are weakly coupled to the bulk of the AF, taking into account the critical temperature of 100K which is lower than $T_N$ for the CoO. In contrast, the “plateau” part is due to another population of spins, with much larger anisotropy field.

Note that the above ZFC-FC TRM data cannot measure the frustrations in a F/AF interface. In fact, for ZFC-FC measurements of a F/AF bilayers the small signal coming from the AF uncompensated spins would be masked by the F much larger signal. In paragraph 1.3, we will describe and then use another technique to directly quantify the amount of spin-glass like phases of F/AF bilayers.

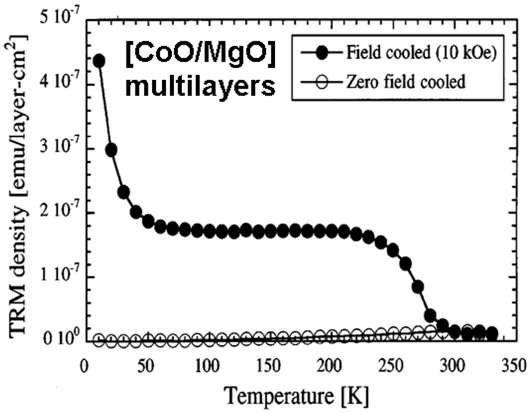

**Figure 1.8**

*FC (empty symbols) and ZFC (black circles) ’magnetization’ as a function of temperature for a $[CoO/MgO]_{15}$ multilayer. After* [17].

Following the above experiments, in the model proposed by Takano [18], he considered a rough AF interface and a polycrystal with single domain CoO crystallite, see Figure 1.9. The simulations predicted about 1% of uncompensated interfacial spins that contribute to the exchange bias. This explained the reason why the experimentally observed values of loop shift are orders of magnitude smaller compared to those calculated with some of the early models. In addition, the model calculates an inverse relationship between the exchange bias field and the grain diameter.

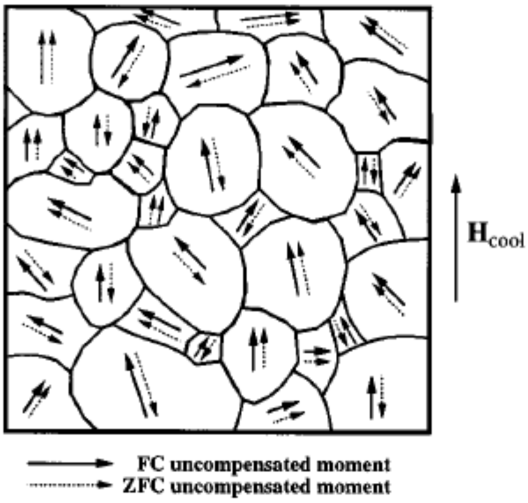

**Figure 1.9**

*Schematic of uncompensated AF moments of uniaxial AF grains in a polycritalline AF. The uncompensated AF moments point randomly 'up' or 'down' in the ZFC case; whereas in the FC case all the uncompensated AF moments havea component along the direction of the cooling field. After* [17].

### 1.2.4. Todays' macroscopic picture: granular model plus spin-glass like phases

Although literature on microscopic models bring forward some of the microscopic mechanisms accounting for the EB macroscopic consequences and given the complexity of the class of spin-glass systems discussed above, providing a universal microscopic model for EB is illusory. Yet, at the macroscopic level, it is commonly accepted since the $90^{ies}$ that a granular model [19] coupled to interfacial spin-glass shall account for the EB properties. This vision is for example clearly depicted by Berkowitz and Takano in Figure 1.10 of their 1999 review paper [20] and used in Refs. [21] and [22] to account for experimental results. In fact, different terminologies now describe the same idea: SG-like phases; SG-like regions; spin clusters but it is implemented in different ways in models: i) by a smooth thermal variation of the F/AF interfacial coupling $C^*(T)$ [22] that indirectly and partly results from the SG-like phases distributions or ii) directly by the SG-like phases distributions [21]. However, the use of a single $C^*(T)$ fails in reproducing bimodal $DT_B$ [22].

Up to now, we were mainly focusing on the principles of EB almost regardless of thermal effects. Since further down we will deal with thermally activated process and with polycrystals, let's now describe the macroscopic picture that we will use for the following of the manuscript (granular model with spin-glass like phases) and its thermal dependence. This vision is influenced by Fulcomer and Charap and by Berkowitz and Takano and was extensively described in [21].

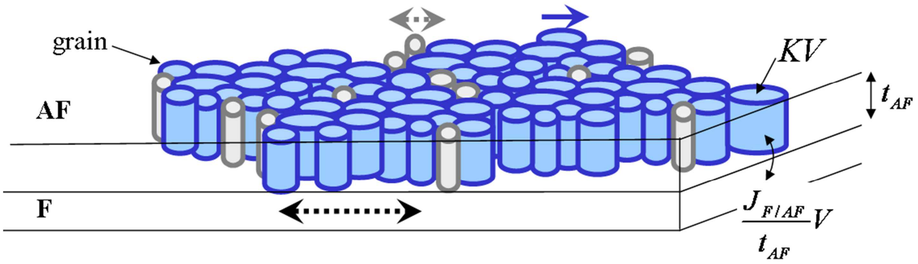

**Figure 1.10**

*Sketch of a polycrystalline F/AF bilayer at a given temperature, $T_M$. To ease the reading, only the AF grains are sketched. Blue color indicates the grains pinned at $T_M$, thus contributing to the EB, while grey refers to unstable grains. After* [93].

The granular model was initially proposed by Fulcomer and Charap [19,23] when studying the progressive oxidization of NiO/Ni, thus resulting in AF grains of different sizes. Based on the Stoner-Wohlfarth [24] reversal calculations, they considered the energy barrier for the AF grains to reverse and straightforwardly found that, for a given temperature the contribution of each AF grain to the loop shift depends on the size of the grain. The EB was affected both by the size and number of the grains, in a good agreement with their experiments. They used the simplified description of the F/AF bilayer sketched in Figure 1.10. The AF layer is viewed as an assembly of almost uncoupled grains. The pinning energy of each grain is KV, where K is the anisotropy energy per unit of volume and V is the volume of the AF grain. Each AF grain is coupled to the F layer by an effective exchange interaction per unit area $J_{F/AF}$ [20,25,26]. After the initial FC process to set EB (see Chapter 1.1.2), all the grains are oriented towards the FC direction. In fact, the external field polarizes the F magnetization so that the AF spin lattice of each grain adopts a magnetic ordering which satisfies as much as possible the F/AF interfacial exchange interactions to minimize the total energy. From this state, if a strong enough field is applied to reverse the F layer magnetization, all the AF grains are then subjected to the torque coming from the exchange interaction with the F spins. The criteria of reversibility for each grain depends on its intrinsic pinning (KV), the coupling to the F ($J_{F/AF}$) and the thermal activation energy. The latter can be expressed as follows: $\log(\tau/\tau_0)k_BT$, where τ is a characteristic time of experiment (~ 1s), $\tau_0$ is the attempt time (~$10^{-9}$s) and $k_B$ is a Boltzmann constant. The criterion for stability of a given AF grain spin lattice is related to the comparison between: $(K - J_{F/AF}/t_{AF})V$ and $\log(\tau/\tau_0)k_BT$, $t_{AF}$ being the AF thickness. The blocking temperature ($T_B$) of an AFM grain is thus defined by: $(K-J_{F/AF}/t_{AF})V \propto \mathrm{Log}(\tau/\tau_0)k_BT_B$. For a given temperature, and according to Fulcomer and Charap, the grains can be split in three groups: i) the superparamagnetic grains that due to thermal fluctuation do not contribute to $H_E$ but only to $H_C$; ii) the AF grains with high anisotropy, holding their orientation while cycling the magnetization of the F. These AF grains were called "frozen spins" and hence were responsible for the loop shift; and iii) the last group consisted of grains with weaker anisotropy and strongly coupling to the F thus being responsible for both $H_C$ and $H_E$. The loop shift can be expressed as:

$$M_S H_E t_F = \int_{stable\ grains} \frac{J_{F/AF}V}{t_{AF}} P(V)dV \tag{1.9}$$

where $M_S$ and $t_F$ are the saturation magnetization and thickness of the F layer respectively.

It was however argued that the temperature dependence of EB is more complicated than the above picture and there are several reasons for that [21]. Neither the AF anisotropy, nor the interfacial coupling are thermally independent. The AF anisotropy is assumed to vary as the 3rd power of the AF sublattice magnetization which results in a higher intrinsic grain energy at lower temperatures. Concerning the interfacial coupling it strongly depends on the interfacial quality. More precisely, interfacial roughness may result in the co-existence of both positive and negative couplings with F-lattice even within a single grain trough the interface. Such kind of disorder may further be interpreted as an interfacial exchange frustration as it was explained in Chapter 1.2.3, as well as a spin-glass-like ordering [18,27]. There are various factors that may cause frustrations. Among them the growth-related issues, grain boundaries, texture and interfacial intermixing [16,28–30] can be listed. Important here is that if the frustration degree is high, these AF spins may behave as a spin-glass. The freezing temperature, $T_F$ is a threshold below which these AF regions have a spin-glass behaviour and above becoming a spin liquid. Therefore this results in effective variations of $J_{F/AF}$. For instance, above $T_F$ a F and an AF region with interfacial frustrations may be completely decoupled and this even if the AF core is frozen, whereas below $T_F$ the F and AF re-couple. To conclude, because of the frustrations distributed all over the F/AF interface, there exist a distribution of interfacial coupling $J_{F/AF}$, which was expressed like $D(J_{F/AF})$. This other factor also contributes to the thermal dependence of EB. Taking into account this temperature-dependent distribution $D(J_{F/AF})$, Equation 1.9 writes:

$$M_S H_E t_F = \iint_{stable\ grains} \frac{J_{F/AF} V}{t_{AF}} P(V) D(J_{F/AF}) dV dJ_{F/AF} \qquad (1.10)$$

Such a D($J_{F/AF}$) could be measured experimentally and gave a way to quantify the amount of spin-glass like regions in F/AF bilayers. This will be discussed below.

## 1.3. Quantifying the amount of spin-glass like phases

In this paragraph, based on the above discussed macroscopic model, the distributions of blocking temperatures and in particular the procedure to measure these latter is extensively described. The reasons of this is the following: blocking temperature distributions measure both the amount of F/AF spin-glass like phases and the stability of the AF grains and this was widely used during my PhD work, as shown later.

Although interfacial spin-glasses (SG) have been known for long as an exchange bias key ingredient [20] few quantitative data are available and no versatile technique existed until recently for their quantitative measurement, i.e. routinely available, fast and compatible with most F/AF bilayers. We discussed above (Paragraph 1.2.3) the case of TRM ZFC-FC which cannot probe F/AF interfaces. Note also that, X-ray magnetic dichroism [31] measures the amount of spin-glasses since the absorption from left- and right-circular polarized light and its further treatment and analysis gives the ratio between rotatable and frozen spins. Yet, with this technique require large scale synchrotron facilities, not routinely available and may suffer from stacking constraints related to elements absorptions that would mask the relevant AF spins signal.

Next, the measurement of blocking temperature distributions is detailed. It is a versatile recent technique that measures the amount of spin-glass. The technique is based on the one proposed by Soeya [32], but with an extension to the very low temperature to access information on the low-freezing spin-glass like regions. For the sake of the simplicity the term AF entities refers both to the grains and to the spin-glasses. The measurements are taken at fixed measuring temperatures ($T_M$) and are followed by specific field cooling procedures that consist in applying incremental field cooling process which results in a gradual reorientation of the AF entities. The successive steps are described below and sketched in Figure 1.11. Typical raw hysteresis loops that I measured during the procedure (with $T_M$ = 4K) are shown in Figure 1.12 for the example of a Si/SiO2// Ta(3nm)/Cu(3nm) / Co(3nm) /IrMn(7nm) /Pt(2nm) sample. The small linear contribution to the loops with negative slope is ascribed to the diamagnetic response of the sample holder and substrate.

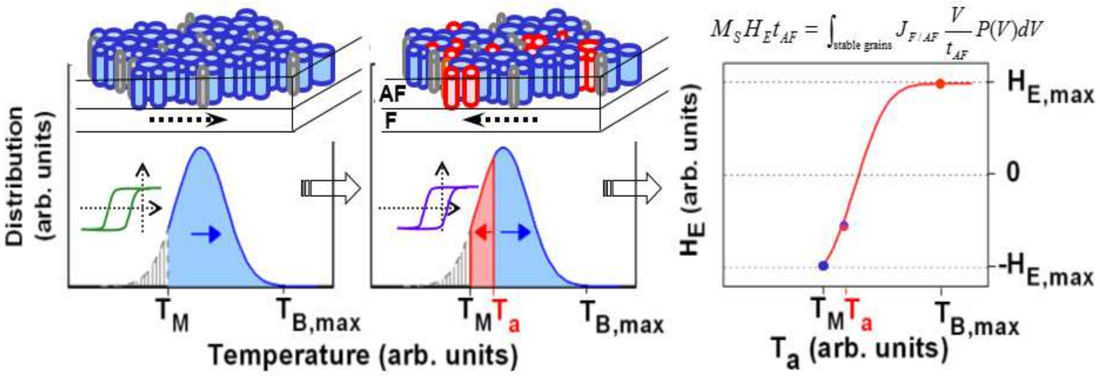

**Figure 1.11**

*(Left) Sketch of the AF entities orientations and corresponding DTB after: i) FC with a positive field from above the maximum TB ($T_{B,max}$) down to the temperature of measurement ($T_M$). (Middle) Same representation after: step i) followed by step ii) consisting in FC with a negative field from an annealing temperature (Ta) down to $T_M$. (Right) Sketch of the resultant dependence of the EB field($H_E$) measured at $T_M$ as a function of $T_a$* [21].

Initially, the EB is set by post-deposition annealing in a furnace under a positive field from above $T_{B,max}$ (here from 573K during 90 min) down to $T_M$ (here 4K). Thus, all the AF entities are polarized positively. This state of the system is illustrated in Figure 1.11 (left). In this figure, the entities in grey correspond to those with a $T_B$ below the $T_M$ and for which no information can be obtained, because the thermal activation energy overcomes the interfacial exchange and anisotropy energies, thus there is no contribution to the EB from that region. Since all the entities are polarized in the same direction, the loop shift for this initial FC shows maximum EB field. The following steps consist in switching the field to the opposite direction, then heating up the system to an intermediate temperature $T_a$, cooling the system back to $T_M$, and measuring a hysteresis loop at $T_M$. As illustrated in Figure 1.11 (middle) the shift in field, $H_E$, integrates AF entities with $T_B$ larger than $T_a$ (unaffected by the FC at $T_a$ and still initially oriented positively) minus AF entities with $T_B$ lower than $T_a$ (reoriented negatively). The above steps are repeated for increasing values of $T_a$. A gradual change in the amplitude and sign of $H_E$ is observed in Figure 1.12 and Figure 1.13 since the higher the $T_a$, the more the reversed entities. Applying this steps with incremental $T_a$, one will evolve the system from initial state with all the entities polarized in one direction, thus having $-H_{Emax}$, to the case with all the entities oriented to the opposite one resulting in $H_{Emax}$.

The dependence of $H_E$ as a function of $T_a$ is sketched on Figure 1.11 and experimental results are reported in Figure 1.13(a). In addition and by definition, the derivative $\delta H_E/\delta T_a$ vs $T_a$ corresponds to $DT_B$, see Figure 1.13(b). Thus: i) an inflection point for $H_E$ vs $T_a$ denotes a peak in the distribution and ii) the amplitude around the inflection, $\Delta_i$ is the surface, $S_i$ of the corresponding peak. In the following, we will discuss in terms of amplitude and surface without distinction. Since in the results and discussion paragraphs we will mostly deal with Δ and S, these notations are of a great importance and are to be kept in mind for the understanding of the following. Note also that, as it was pointed out earlier in the literature, the coercive field $H_C$ relates to the AF entities with spin-lattices dragged during the magnetization reversal of the F layer. This effect is independent on the cooling history which explains the invariance of $H_c$ on $T_a$ since all the loops are measured at 4K. It also confirms that $M_S$ does not depend on $T_a$ for the same reasons.

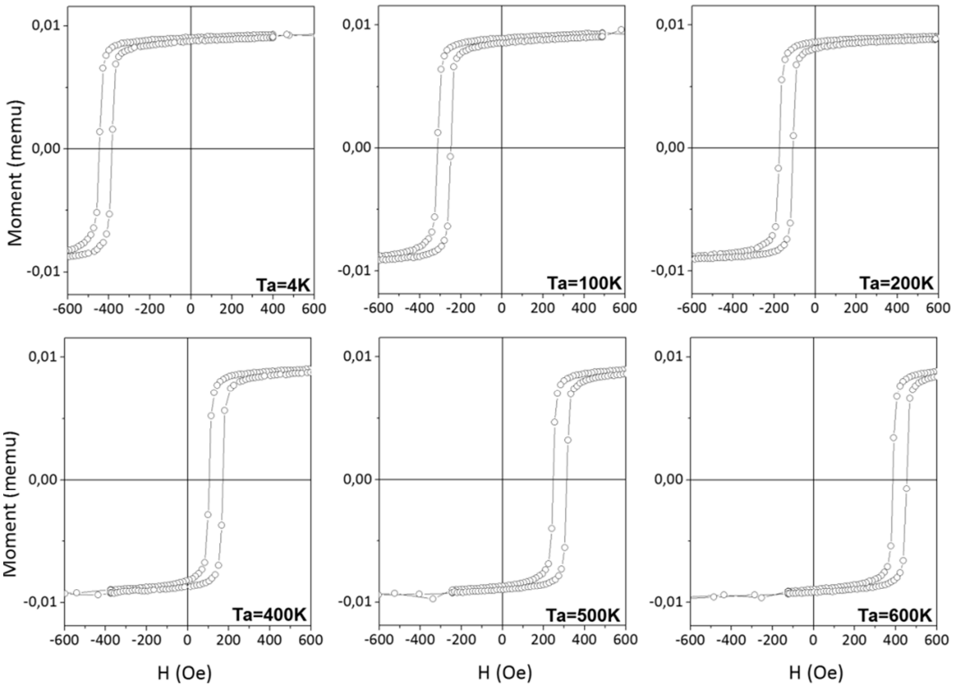

**Figure 1.12**

*Typical hysteresis loops measured with a VSM along the FC direction at $T_M$ = 4K for different annealing temperatures ($T_a$), for a film of Si/SiO2// Ta(3nm)/ Cu(3nm)/ Co(3nm)/ IrMn(7nm)/ Pt(2nm). The loops are subsequent to a specific cooling procedure involving various $T_a$ and described in the text.*

The advantage of this procedure is that all measurements are performed at the same measuring temperature. Accordingly, it focuses on the thermal distributions and not on the thermal variations. Another experimental procedures like measurements of $H_E$ as a function of $T_M$ (note, that $T_M \neq T_a$) cannot provide directly thermal distributions since $H_E$ vs $T_M$ mixes thermal distributions and thermal variations, e.g.[33].

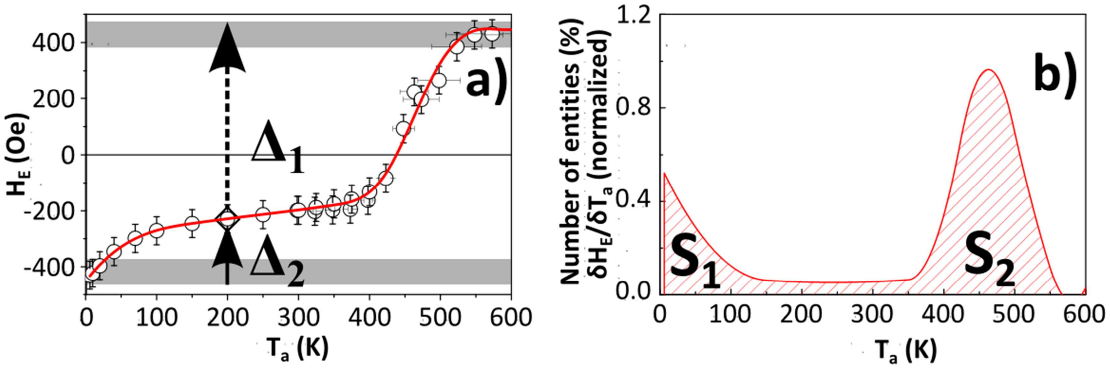

**Figure 1.13**

*(a) loop shift ($H_E$) as a function of $T_a$ and (b) normalized derivative ($\delta H_E/\delta T_a$) calculated from (a) curve as a function $T_a$ for a sample of Si/SiO2//Ta(3nm)/Cu(3nm)/Co(3nm)/IrMn(7nm)/Pt(2nm). The values of $H_E$ were taken from the hysteresis loops shown above and subsequent to cooling procedures described in the text. The derivative (b) is the blocking temperature distribution. The red curve in (a) is an interpolation of the raw data and is used for the derivative. Also, the grey areas in (a) stand for the maximum and minimum values of $H_E$, within experimental error. Note that $H_{Emin}$ = - $H_{Emax}$.*

Further analysing Figure 1.13, it now discuss the origin of the typical bimodal $DT_B$ observed. The $T_B$ distributions are made of two contributions:

i) a commonly observed high-T contribution that was associated in the literature to thermally activated reversal of the AF grains spin-lattice. For example, and in agreement with the granular model, this contribution shifts toward larger T when the AF thickness is increase [21,22,34] and Figure 1.14.

ii) a low-T contribution ascribed to F/AF interfacial spin-glasses. In contrast to the high-T contribution, this low-T contribution to the $T_B$ distribution was found to be independent on $t_{IrMn}$. Because of this, the magnetic entities associated with this second low-

T contribution are likely associated with the F/AF interfacial spin-glass like region exhibiting low freezing temperature $T_F$, typically between 4K and 70K). These regions undergo spin reorganization when the sample is annealed at $T_a$ typically between 4K and 70K and FC in opposite field. This interfacial spin reorganization locally changes the effective coupling $J_{F/AF}$ across these regions thus affecting the EB field (see Equation (1.10)). These spin-glasses are probably those located nearby any particular defects, e.g. grain boundaries or roughness-induced steps, which are able to locally reduce the molecular field. The distribution of the above properties results in a distribution of $J_{F/AF}$: $D(J_{F/AF})$ (Equation (1.10)), which is directly probed here. Within a grain with many interfacial frustrations, the F and AF are magnetically coupled across spin-glass like interfacial regions only up to $T_F$, even if the AF core below may remain frozen up to $T_B$. Over the whole sample, the resulting low-T $DT_B$ is related to the distribution of $T_F$ which transposes in an effective distribution of $J_{F/AF}$: $D(J_{F/AF})$. In contrast, at interfacial regions where the frustration is weak, F and AF are magnetically coupled up to $T_B$. In other words, bimodal $DT_B$ are essentially due to the convolution between P(V) peaked at high-T and $D(J_{F/AF})$ peaked at low-T.

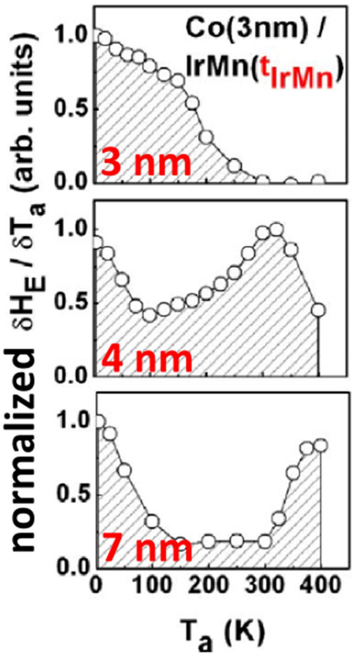

**Figure 1.14**

*Blocking temperature distributions for //Ta (3nm)/ Cu (3nm)/ Co (3nm)/ IrMn ($t_{IrMn}$)/Pt (2nm) continuous films with $t_{IrMn}$ = 3, 4 and 7 nm from top to bottom respectively* [21].

Given that most applications work above 300K, many studies from the literature used a measurement temperature, $T_M$ of 300K and observed the well-known high-T contribution to $DT_B$, i.e. single mode distributions. It was often studied in view of understanding the influences of the structural properties and magnetic parameters (e.g. anisotropy, exchange stiffness) of the F/AF bilayers on the mean value, maximum value or standard deviation of the distribution [22,34]. By reducing $T_M$ to 4K, a second contribution was observed. The use of blocking temperature distributions [32] and its extrapolation to 4K [21] offers a unique versatile way to quantify the glassy character of a FM/AFM interface. This was recently introduced by the SPINTEC laboratory [21] and thoroughly studied since then. In particular, by tuning various parameters such as the AF material (IrMn vs FeMn and NiMn) [21], F/AF interfacial mixing [35] via thermally activated species diffusions [36], the AF crystallography (polycrystalline- vs epitaxial-AF) [37] and lateral sizes [38], some of the key parameters influencing the formation of these F/AF spin-glass phases were identified and especially the role of Mn diffusions for Mn-based AF. Later on in this manuscript, we will deeply study the effect of Mn-diffusion, solutions to avoid such diffusion and the insights that this quantitative approach brought for applied spintronics and in particular for thermally activated TA-MRAMs.

Finally by comparing the various amplitudes ($\Delta$) either between high- and low-T contributions to $DT_B$ for a given sample, or between low-T contributions for various samples we can quantify the relative impact of the F/AF glassy character. Basically, the smaller the $\Delta$, the less the amount of spin-glass like phases. We will use this later on. Prior to that, let us detail some of the applications using exchange bias. Next, I will briefly introduce the notions of giant and tunnel magnetoresistance, the sensors applications and I will extensively describe memories applications and in particular thermally-assisted (TA) magnetic random access memories (MRAM). Essentially, this PhD work was done in the context of TA-MRAM. At the end of the next section, the issues related to TA-MRAM and the problems tackled in the frame of this PhD will be introduced.

# Chapter 2.

# Applications of exchange bias and issues to be solved

Spintronics applications such as thermally assisted MRAM (TA-MRAM), sensors (e.g.. hard disk drive read head), logic devices and radiofrequency emitters use F/AF EB interactions to set the reference direction required for the spin of conduction electrons. In this chapter, I will briefly discuss the principles of giant and tunnel magnetoresistance, that of a spin-valve with exchange bias F/AF bilayers and the applications employing these phenomena. Among the numerous kinds of devices employing magnetic properties, from very precise medical tools and microscopes to hard machinery and transducers, there are two major domains which are closely related to the current study. One of them is developed to detect magnetic field and the other stores data. Thus, the former belongs to the sensors family and the latter to the memories. Both of these families experienced a significant improvement over the last decades, not only because of modern technological facilities, but also thanks to several breakthrough discoveries. Nevertheless, the evolution of any technology happens step by step. I will focus on the evolution of sensors employed in HDDs read heads since the discovery of giant magnetoresistance (GMR) in 1988, and of another type of solid-state non-volatile magnetic data storage technology: magnetic random access memories (MRAM), since most of the work done in this PhD relates to MRAM.

## 2.1. Introduction of key concepts

### 2.1.1. Giant magnetoresistance

The discovery and interpretation of the giant magnetoresistance (GMR) phenomenon was rewarded by the Nobel prize in 2007. In 1988, Pr Peter Grunberg [39] and Pr Albert Fert [40] independently discovered this phenomenon in (Fe/Cr) sandwiches and multilayers. Their groups studied multilayered magnetic structures consisting of alternation of magnetic and non-magnetic layers. Repeated Fe/Cr($t_{Cr}$) multilayers with varied Cr thickness ($t_{Cr}$) were studied, i.e. Fe thin layers separated by non-magnetic Cr metallic spacers. The first experimental result is shown in Figure 2.1a) for various thicknesses of Cr interlayer.

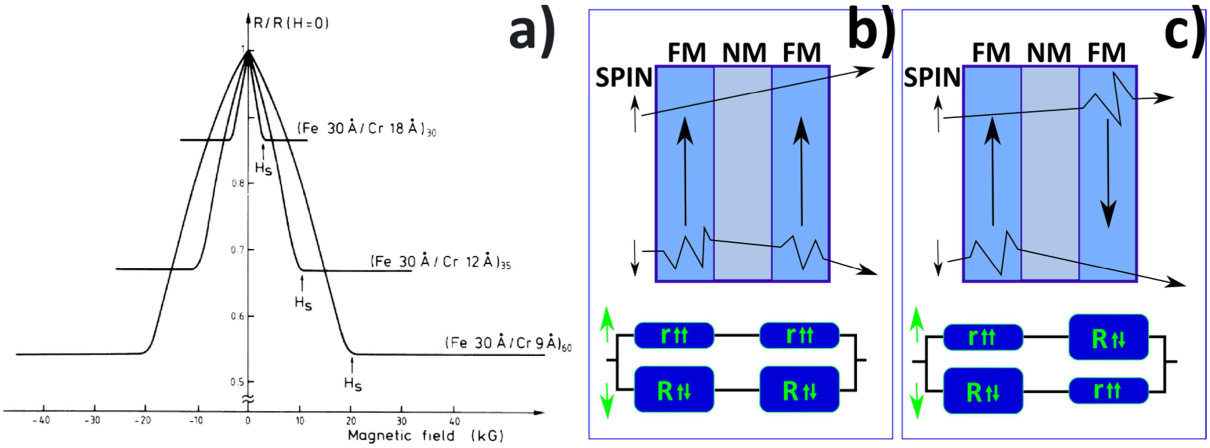

**Figure 2.1**

*a) R(H) loops measured at 4.2K for [Fe (3nm)/ Cr ($t_{Cr}$)]$_N$ multilayers with $t_{Cr}$ equal to 1.8, 1.2 and 0.9 nm and N repetitions = 30,35 and 60 respectively (After* [40]*). b) Schematically illustrated GMR scheme for 2 different F-layers orientation. Up-left – parallel configuration with low-resistance and up-right with a high resistance states. Bottom, corresponding sketch with the simplified equivalent electric circuit indicating the total resistance of the device. After* [41].

The working principle of this system is based on a specific electron property – its spin, or more precisely on the spin-dependent conductivity in magnetic transition metal. The electrical current can be considered as carried in parallel by the spin “up” and spin “down” electrons. The notion of up and down refers to the spin-orientation relatively to the local magnetization. The resistivity of spin up and spin down electrons are equal in non-magnetic materials such as Cu or Al. However, in magnetic transition metal such as Fe, Ni and Co, the resistivity becomes spin-dependent. This is due to the different density of states at the Fermi for “up” and “down” spins orientation. Accordingly, the phenomenon of GMR arises from the spin dependent scattering phenomenon occurring in the bulk of the magnetic layers and their intefaces with the non-magnetic spacer. The overall electron scattering rate depends on the relative orientation of the magnetization in the successive ferromagnetic layers. (see Figure 2.1b)). Thus the two oppositely oriented populations of electrons propagating from one magnetic material to another through the non-magnetic spacer behave differently. Let us consider a three layer structure with F-layers separated by a non-magnetic spacer. When the two F layers are in parallel magnetic configuration, the system is in the low resistance state Figure 2.1b). Indeed, in this case the population of electrons with spins parallel to the magnetization direction can easily traverse all layers with weak scattering. These spin up electrons can then carry lot of current and create a sort of short-circuit in the system. The spin-down electrons are strongly scattered in both magnetic layers but still the resistance is low due to the short-circuit effect of the spin-up electrons. If now the system is switched in the antiparallel magnetic configuration, both populations are affected Figure 2.1c) in either of the two F-layers. Now both categories of electrons are strongly scattered in one or the other ferromagnetic layers. The short-circuit effect of spin-up electrons present in parallel magnetic configuration no longer exists in the antiparallel configuration. As a result, the resistance becomes higher. Underneath sketched paths of electrons for each configuration, there is an equivalent resistance circuit for both configurations (Figure 2.1b-c). In this manner, by varying the magnetization direction of one magnetic layer so as to change the magnetic configuration from parallel to antiparallel, it becomes possible to achieve two distinct resistance states of the system.

Following the above sketched equivalent resistance circuits, one can derive the total resistance of the system in parallel and antiparallel orientations and the GMR ratio:

$$R_P = \frac{2R_{\uparrow\downarrow}r_{\uparrow\uparrow}}{r_{\uparrow\uparrow} + R_{\downarrow\uparrow}} \; ; \; R_{AP} = \frac{R_{\uparrow\downarrow} + r_{\uparrow\uparrow}}{2} \tag{2.1}$$

$$GMR = \frac{R_{AP} - R_P}{R_{AP}} = \frac{(R_{\uparrow\downarrow} - r_{\uparrow\uparrow})^2}{4R_{\uparrow\downarrow}r_{\uparrow\uparrow}} \tag{2.2}$$

### 2.1.2. Tunnel magnetoresistance

In 1970 spin-polarized tunneling was predicted by Tedrow and Meservey [42] and experimentally reproduced by Julliere [43] 5 years after. Studying Fe/GeO/Co structures, he found a resistance variation depending on the mutual orientation of the F-layers magnetization. As predicted by Slonczewski [44], the conductance of magnetic tunnel junctions is expected to be proportional to the cosine of the angle between the magnetization of the two F layers. Hence, the highest conductance (i. e. lowest resistance) is observed in the collinear case. Nevertheless, the interest for magnetic tunnel junctions dramatically increased when it became possible to perform magnetic tunnelling experiments at room temperature [45,47] with as much as 12% of MR ratio Figure 2.2a). These results were obtained with amorphous Alumina barrier. In these MTJ, the TMR amplitude is only determined by the electron polarization at the Fermi energy in the ferromagnetic electrodes. This polarization is equal to the relative difference in density of states at Fermi energy for spin up and spin down electrons in the ferromagnetic layers. Following this breakthrough discovery, many studies were dedicated to increasing the tunnel magnetoresistance (TMR) amplitude by a proper choice of the tunnel barrier material. One of the best candidates as insulating layer which was predicted in 2001 [48,49] is thin crystalline MgO 001 [50] layer. The major difference between MgO and Alumina barrier is that the former are crystalline with good crystal matching with the ferromagnetic electrodes whereas the latter are amorphous. Thanks to this crystallinity, a new spin-filtering mechanism takes place associated with the symmetry of the wave functions. Electrons with Δ1 symmetry can tunnel easily through MgO barriers. It turns out that only spin up electrons have this Δ 1 symmetry in Fe so that spin up electrons can easily tunnel in parallel magnetic configuration but not in antiparallel magnetic configuration [51]. This additional spin-filtering mechanism allows to significantly increase the TMR amplitude. In the late 90s, with Alumina barrier, the observed TMR were in the range 40-70% at room-temperature.[52–55]. In 2004, TMR over 200% at RT were reported with MgO based crystalline MTJ, 410% TMR in 2006 [56] in 2007 500% [57] TMR was reached. In the following two subchapters, 2 different families of applications based on the above described phenomena will be discussed.

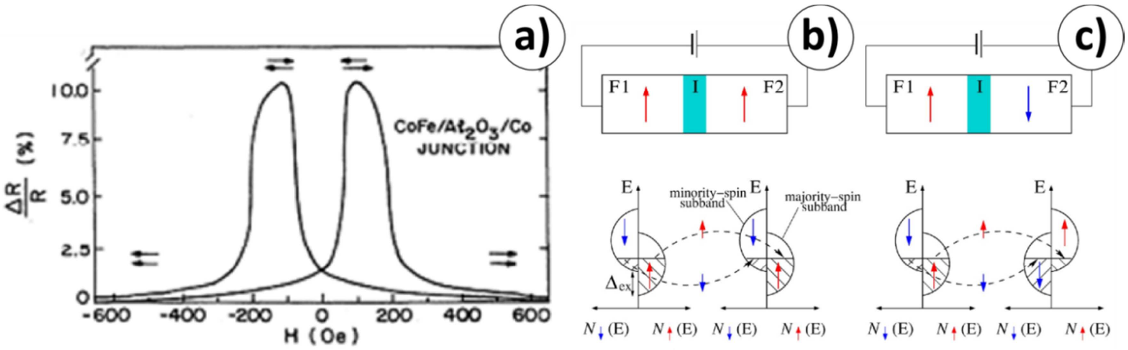

**Figure 2.2**

*a) Room-Temperature magnetoresistance (R-H) loops for CoFe/Al$_2$O$_3$/Co tunnel junction. After* [45]. *b) Parallel and c) antiparallel F-layers mutual magnetization orientation with corresponding spins' densities of d-states. After* [46].

Tunneling Magneto Resistance (TMR) schematically is very similar to the GMR concept, apart from its physical origin due to the nature of material that separates F layers. Rather than using NM conducting layer like in GMR, for the TMR an insulator is inserted between magnetic electrodes. Applying voltage to F-electrodes and having thin enough insulator, there is a quantum mechanical probability for electrons to tunnel through the insulating layer. The TMR can be written as follows:

$$TMR = \frac{R_{AP} - R_P}{R_{AP}} = \frac{2P_1P_2}{1 - P_1P_2} \tag{2.3}$$

where $P_i$ is the polarization of the density of states (DOS) at the Fermi level for each F layer surrounding the tunnel barrier:

$$P_i = \frac{D_{i\uparrow}(E_F) - D_{i\downarrow}(E_F)}{D_{i\uparrow}(E_F) + D_{i\downarrow}(E_F)} \tag{2.4}$$

### 2.1.3. Spin-valve

The spin-valve concept proposed in 1991 [58] consists in pinning the magnetization direction of one of the F-layers (in this case, the reference layer) by coupling this layer to an additional adjacent AF layer to pin it . Thanks to the F/AF exchange coupling, the F layer magnetization becomes stable and acts as a reference, while the magnetization of the sense F-electrode is free and therefore can easily rotate towards the applied field direction. The corresponding R-H loop on Figure 2.3b) shows the magnetic and transport responses of this system. Contrary to the first GMR-sandwiches consisted of two F-layers (Fe) coupled antiferromagnetically through a NM (Cr) spacer, spin-valve concept consists of two uncoupled F-layers separated by a non-magnetic spacer layer inducing no or only very weak interlayer coupling (typically Cu more than 2nm thick). Following this concept, the sensitive free layer magnetization is able to detect low fields while the pinned layer magnetization remains in a fixed direction reference. Spin-valves thus provided extremely sensitive magnetic field sensors and have been used as read head in hard disk drives between 1997 and 2004. (For detailed spin-valve review see for example - [59]).

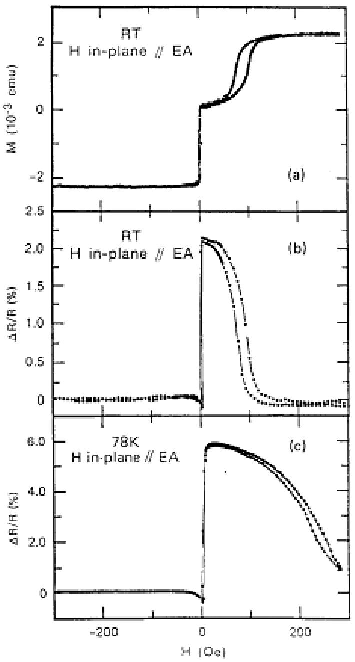

**Figure 2.3**

*(a) hysteresis loop and (b) magnetoresistance loop at room-T and (c) magnetoresistance loop at 78K;for a sample with composition: Si/ NiFe (15nm)/ Cu (2.6nm)/ NiFe (15nm)/ FeMn (10nm)/ Ag (2nm). The field is cycled along the FeMn FC direction. After* [60].

## 2.2. Magnetoresistive read heads for hard disk drives

Many devices such as cell phones, smart-phones but also automotive or robotics require position and orientation sensors. When IBM introduced the AMR read-heads, replacing inductive coils it was already a giant leap in magnetic storage industry and led to a period of rapid areal density increase up to 1Gb HDD capacity with the rate about 60%/year for the areal density increase. The following years researchers were looking for a solution to further improve the scalability. With the AMR-based devices the main difficulty was related with the origin of phenomenon. Being a bulk effect, to be able to detect change in magnetization coming from tiny area, the sensor itself should be comparably small. With AMR, lowering the thickness lowers the output signal strength. This comes from the electrons property – with the film thickness up to couple of tens nanometers they start scattering out of the film surface up to an extent when signal to noise ratio becomes crucial. Therefore AMR-based read-heads could not be considered as a promising technology to increase areal density for the recording media. Being an interfacial effect, GMR was the best candidate to replace previous technology, with its high output signal at very low thickness of sense layer.

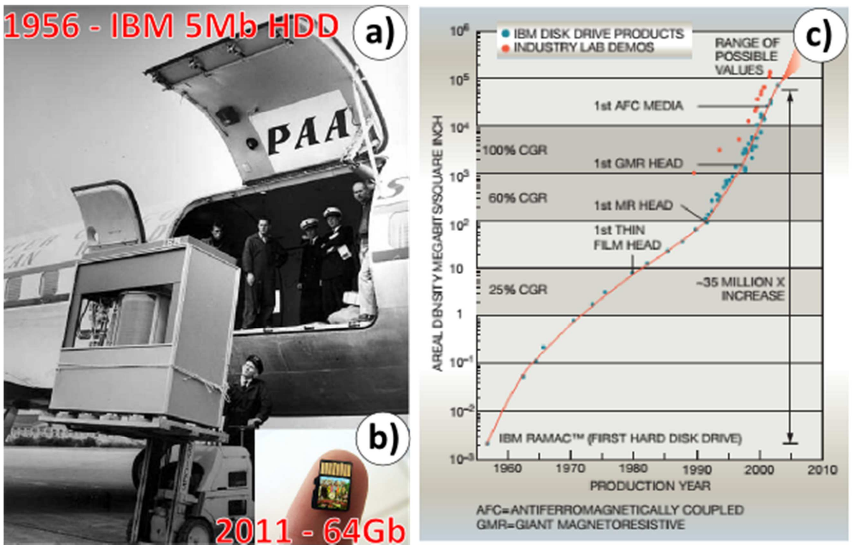

**Figure 2.4**

*The evolution of magnetic storage industry: a) IBM 350 model with 5 Mb capacity introduced in 1956* [61] *(picture from* [62]*), b) Micro SD card with 64 Gb storage capacity on a human finger (picture from* [63]*), and c) time evolution of the data storage areal density, after* [64].

Having just a few percent of MR ratio for AMR and a couple of tens percent for GMR, one can guess how rapidly the further progress was evolving. To have a basic idea on how revolutionary it impacted magnetic recording industry, two numbers will make this impression. Before the introduction of GMR-based magnetic read-heads in 1997 the areal density was only 1 Gbit/in$^2$ whereas 10 years later IBM showed a hard drive with the value of 300Gbit/in$^2$. This huge technological leap completely changed recording media market. The famous Moore's law reflecting the evolution of the number of transistors with the time has an analogy, representing the memory areal density reduction (Figure 2.4*)* for so-called magnetic areal density. This parameters simply tell us how small in its lateral dimensions can be written a Boolean elements – logic "1" or "0". This correspondence becomes natural if one considers the more and more powerful machines and computers that obviously lead to the development of related technological progress in various areas. The quality of digital cameras, videos, photos, internet solutions and other media, demands larger storage capabilities.

Even though it may seem easy to implement new GMR-based approach, having good MR ratio, in a fully functional device, in fact there were a lot of efforts done to bring it to the market, especially dealing with low scales. One of the difficulties in GMR-based device implementation was related with magnetic field to reverse the magnetization of the storage layer. Being coupled antiferromagnetically (otherwise the system will be always in parallel state), the applied field to reverse the magnetization of storage layer should be strong enough to overcome the AF coupling energy. Although, showing high MR ratio at low temperatures, the MR amplitude decreases significantly with temperatures and was requiring high field to be obtained (the MR about 65% at RT for Co/Cu multilayers was reached in 1991 [65] and required saturation field as big as 10kOe, whereas 35% of MR were available at only 300 Oe). Furthermore, in order to reduce the lateral dimensions of one bit - the read-head size had to be reduced accordingly, leading the storage and reference to become thinner and thinner. This issue was solved thanks to the spin-valve concept presented previously [59].

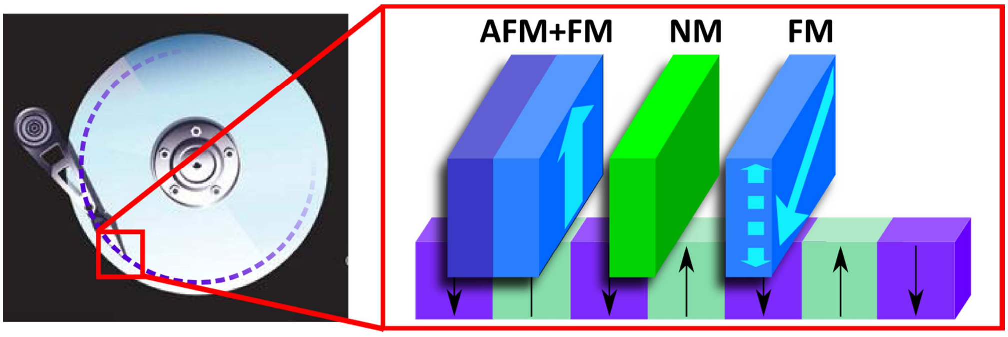

**Figure 2.5**

*Picture of real HDD drive (left) with a sketch of the read-head (up-right). The Reference and free layer's easy axes are perpendicular. Below the spin-valve structure is also sketched the track of "0" and "1" bits.*

As it is schematically illustrated on Figure 2.5, the read-head flying above the surface of the disc senses the magnetic field coming from the underneath media. Obviously, the thickness of the free layer should not be greater than the length of each bit in the downtrack direction, otherwise the signal from two neighbouring bits would be detected, that in turn will lead to high error rate and big signal to noise ratio. In terms of media, a significant improvement has been the change from in-plane to out-of-plane magnetized media. Before, the magnetization was in plane and the bit readout was based on domain boundaries detection, producing stray fields. With the time, it became obvious, that longitudinal magnetization approach was reaching its limit with bit size reduction. The reason was that data retention for 10 years imposes the requirement $K_{eff}V > 67\ k_BT$. where $K_{eff}V$ – anisotropy energy, $K_{eff}$ – anisotropy constant, V –the volume of the grain, $k_B$ – Boltzmann constant. $K_{eff}$, being a fixed parameter as a material property, with continuous decrease of bit size (volume V accordingly), would lead to super-paramagnetic limit. The out-of-plane magnetic recording approach was proposed to push further the density of bits per unit area. Indeed, when the magnetization points out-of-plane, the demagnetizing field decreases while reducing the bit size. This magnetic configuration allowed increasing the areal density up to 750 Gbits/in$^2$, which is 18 times denser than for longitudinal media. In 2005 Seagate Corporation launched HDDs with heads based on TMR effect. Their larger MR ratios allowed keeping on increasing the storage capabilities of HDDs. High TMR ratios provide high signal to noise ratio provided the resistance area (RA) product can be maintained sufficiently low so that the sensor resistance remains in the range of a few tens of ohm and keep the shot noise low enough. [66].

## 2.3. Memories

Another family of devices based on the TMR-effect is magnetic random access memories (MRAM). In contrast to sensors where the magnetization of the free layer coherently rotates around a 90° orientation with the magnetization of the reference layer, in memory, the magnetization of the soft layer (called storage layer), can lie in two possible stable states (parallel or antiparallel magnetic configurations) with two associated values of MTJ resistance. The magnetization direction is switched either by application of a magnetic field or by using the spin-transfer-torque phenomenon. The information is stored as the magnetic orientation of the storage layer magnetization. The readout is achieved by measuring the resistance of the stack. In terms of fabrication, memories are much more demanding in terms of process control than read-heads. Indeed, read heads comprise only one MTJ and can be tested and selected one by one. In contrast, memories comprise millions or even billions of MTJs which must have very similar properties. The larger the memory capacity, the more stringent the constrains on the process quality.

From the very beginning, the MRAM concept attracted a worldwide attention that can be easily explained. MRAM have lot of advantages compared to other memory technologies: i) As FLASH memories and in contrast to DRAM or SRAM, they are non-volatile (no loss of data when the power is off); ii) they can be as dense as DRAM iii) Their data retention can exceed 10 years; iv) They have almost infinite endurance meaning that they can be written more than 10$^{16}$ cycles which is much better than all other technologies of non-volatile memories (FLASH: endurance~10$^5$cycles) v) They can be written and read with low power consumption and vi) at high read/write speed (write speed ~3-10ns; read speed~10ns). These memories are solid state memories meaning that in contrast to HDD, the stored information can be accessed without any mechanical movement and in random order (random access memories)

Over the two last decades, many MRAM concepts were proposed for various types of applications. They will be discussed in the next section.

### 2.3.1. Various magnetic random access memories (MRAM) approaches

Over the past 20 years of intensive R&D in the field of MRAMs, several concepts of MRAM have been proposed. They can be divided into 2 major groups depending on the writing method. The first group gathers MRAMs in which the storage layer magnetization is switched by magnetic field writing (field induced magnetic switching - FIMS). In the second group of MRAMs developed mostly after 2004, the magnetization of the storage layer is switched by using the spin-transfer-torque phenomenon (STT).

Concerning the field written MRAM, two main approaches to store information were proposed: Stoner-Wohlfarth (SW) MRAM - and Toggle-MRAMs. SW memory cell consists offTMR-based storage element surrounded by 2 orthogonal metallic wires (called bit line and word line) (see Figure 2.6a)). The writing principle consists in sending pulses of current simultaneously in the two wires crossing at the addressed memory point (see Figure 2.7a)). The writing principle is based on the so called Stoner Wolfarth Astroid [24] partially shown on Figure 2.7b). With proper adjustment of the write current amplitude, the simultaneous presence of the two orthogonal fields is needed to write the selected cell. As it is illustrated on the sketch (Figure 2.7(a-b)), according to this approach, the so-called “half-selected” bits which only feel one of the applied magnetic field along their easy or hard axis denoted in yellow and blue colour respectively do not switch. Only the selected bit feeling the two orthogonal fields can switch. However, very soon it became clear that these half-selected bits may experience uncontrolled switching because of the width of the distribution of switching field in large arrays of memory dots. Indeed, if the distribution of switching field is too large, bits with low switching field may accidently switch when submitted to only one magnetic field. This problem is known as “half select instability». The main factors responsible for the switching field distribution are: the inhomogeneities in stack composition over the whole array area and irreproducibility in the shape of the MTJs associated with variability in the patterning process. Either of these factors led to broadening in switching field distribution. Furthermore, from the scalability point of view, with the decrease of memory cell size, the field-line cross-section decreases as well, that in turn leads to its resistance increase. Hence more power is required to generate the same field. In addition, the current density required to generate the field increases and reaches the electromigration threshold at feature size of the order of 90nm. Also, by bringing closer and closer neighbouring memory cells, cross-talk effect could appear due to the relatively slow decrease of the field amplitude versus distance.

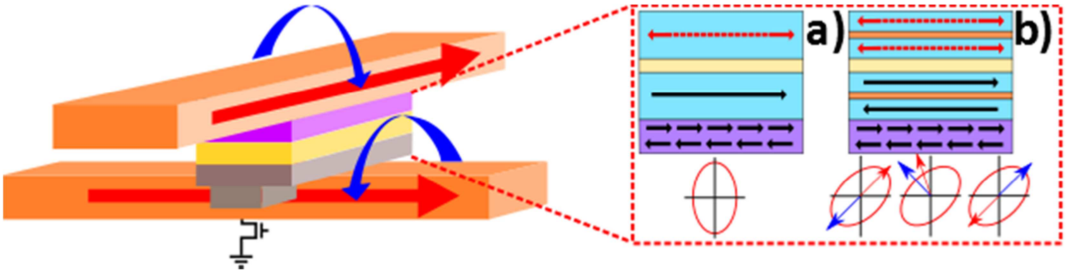

**Figure 2.6**

*(Left) MTJ with two perpendicular field lines with red and blue arrows representing current flow and associated magnetic field. (Right) a) SW- and b) Toggle-MRAM sketches of the stack. For a) both the storage and reference layers are composed of F-material, for b) the F-material is replaced by a synthetic antiferromagnetic layer (SyF) and the easy axis is tilted by 45° to field line.*

To solve the write-selectivity problem of SW MRAM, a major improvement was proposed by Savtchenko [67] in the so- called Toggle-MRAM. This approach solved the "half select instability" problem by replacing the single F layer by a synthetic Ferrimagnet (SyF) (see sketch Figure 2.6b)). SyF consists of 3-layer sandwich with two F-slabs separated by a thin non-magnetic Ru spacer. By adjusting the Ru thickness (usually between 5-10Å), one can tune the coupling strength via RKKY interactions. Another difference compared to SW-MRAM is that the cell is here tilted by 45 so that its easy axis lies along the diagonal between bit and word lines. The writing is more complicate for SyF structure and consists of a sequence of field steps along which the field rotates by successive rotations of 45°.

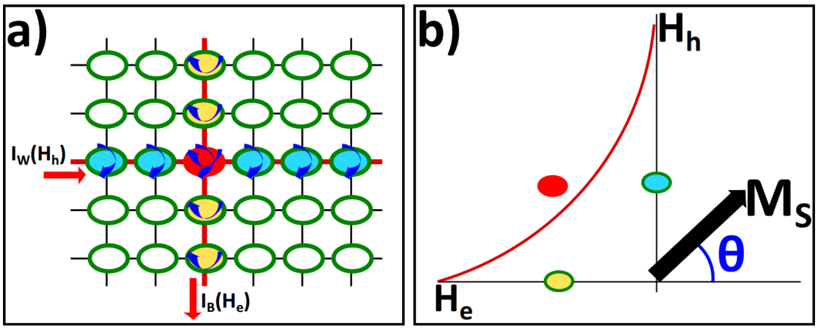

**Figure 2.7 Toggle MRAM**

*a) Schematic representation of a Toggle MRAM array with 2 lines utilized to write the bit; b) part of the SW Astroid with the local fields felt by 3 different cells respectively along an activated bit line, along an activated word line and at their intersection*

In Toggle MRAM, the write process is illustrated in Figure 2.8. At zero field, the magnetization of the two layers constituting the SyF are aligned antiparallel along their easy axis (see time $t_0$ on Figure 2.8). When the write field if applied, larger than the so-called spin-flop field [68], the magnetization of the two layers tend to rotate in a scissor configuration wherein the two magnetization lie symmetrically with respect to the field direction. In toggle MRAM, to switch the magnetization, the field is first applied along the word line direction (line 2 in Fig2.8. at t1). Next, while first field is still applied (time $t_2$), the second field $H_2$ is applied by passing current pulse $I_2$ in the bit line (called line 1 in Figure 2.8) thus aligning the net field with the easy axis direction. Then, at time $t_3$ the current $I_1$ is switched off and only $H_2$ is applied to complete rotation cycle. After this third step, the magnetization of the storage layer represented by a black arrow on Figure 2.8 has almost completed a 180° rotation. At time $t_4$ , the current $I_2$ is turned off and the magnetization relaxes towards the easy axis. Thanks to this 180° rotation, the bit value has changed from one value to the opposite one. Note that because this writing procedure systematically rotates the magnetization by 180°, the bit needs to be read before writing to know if it has to be changed or not from its previous value, depending on the data which has to be written. This toggle approach is more robust for half-selection problem and more thermally stable. Being intensively studied by the company EVERSPIN, the Toggle-MRAM was released on the market by this company. MRAM are particularly suited for aeronautics and space applications thanks to their radiation resistance but also for automotive applications thanks to their robustness, high endurance and ability to operate up to elevated temperature. Also, the appearance of these devices on the market demonstrated that the combination of magnetic back-end technology together with standard front-end CMOS process could be brought to a sufficient level of reliability for commercial products. Despite its initial market success, the scalability problem was still there and it was predicted that the limit of this technology will not go beyond the 90nm node. The reasons for that are very similar to the ones for SW-MRAM – to assure the data retention the energy barrier should satisfy the inequality: $K_{eff}V > 67\ k_BT$. If the volume of the cell is decreased, the anisotropy has to be increased which means that the write current also increases. Since the bit line and word line width decreases with increased density, this means that the current density to produce the write field dramatically increases in the write and bit lines so that the electromigration threshold is reached. In toggle MRAM, this occurs at the 90nm node.

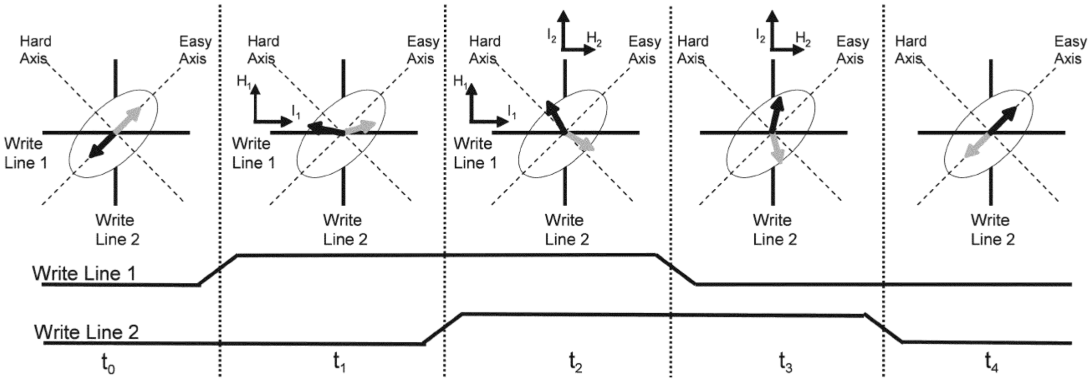

**Figure 2.8**

*TOGGLE-MRAM switching scheme according to Savtchenko approach. The $t_i$ represent successive steps of the write sequence* [69].

SW and toggle-MRAM both use pulses of magnetic fields to reverse the magnetization of the storage layer. However, as mentioned in the introductory part of this section, there are other ways to write the information i.e. be able to switch the magnetization of the storage layer, using the phenomenon of spin-transfer-torque. This is explained below.

In 1996 Slonczewski [70] and Berger [71] predicted the phenomenon of spin transfer torque (STT). They predicted that due to exchange interaction between the spin of the conduction electrons and the spins responsible for the local magnetization, a spin-polarized current flowing through a magnetic layer with some angle between the spin polarization of the current and the local magnetization, can exert a torque on the magnetization. This phenomenon can be explained as follows: let us consider a sandwich structure as illustrated in Figure 2.9. Here the electrons flow from the left ferromagnetic layer (FM1), then pass through the non-magnetic spacer and enter the second FM2 layer. When they pass through the first magnetic layer FM1, the conduction electrons become polarized thanks to spin-dependent scattering phenomena occurring in this layer. When the electrons exit this FM1 layer (also called a polarizer) the conduction electrons have a net spin polarization parallel to the magnetization of FM1 layer. Flowing through non-magnetic NM layer, the spin is conserved. When the conduction electrons arrive at the interface of the second magnetic layer FM2, some of the electrons are transmitted, others are reflected depending on the projection of their spin with respect to the FM2 magnetization. The transmitted electrons spins then precess around the magnetization direction of the FM2. Within about 1nm from the NM/FM2 interface, this incoherent precession motion leads to a complete re-orientation of the conduction electron spin polarization from parallel to FM1 to parallel to FM2. By action and reaction, the reorientation of spin direction produces a flow of angular momentum, which yields a torque on local magnetization. If the current is large enough, it leads to the reversal of the free layer (FM2) magnetization. The current required for STT switching is called critical current ($J_C$) and its amplitude is determined by the ability of the STT to counterbalance the Gilbert damping term.

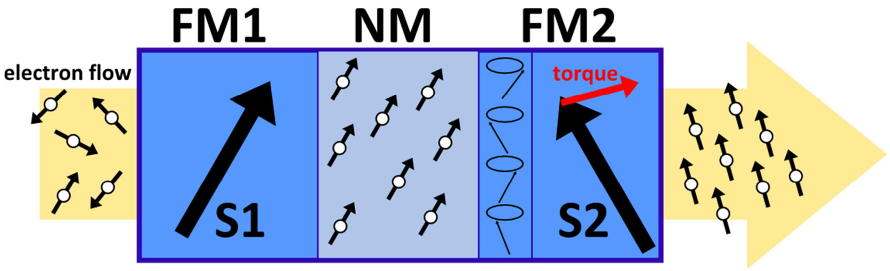

**Figure 2.9**

*Illustration of the STT-phenomenon The current flows through the first magnetic layer so that the spins get polarized parallel to magnetization direction of FM1 layer. Then, passing though the non-magnetic spacer, they enter the interface of the second free layer being either reflected or transmitted. In a free layer (FM2) transmitted electrons start precessing along the magnetization direction with magnetization not parallel to the first one.*

The mutual orientations of two magnetic layers can be switched to parallel or antiparallel configurations by sending current pulses of different polarities. If the electrons flow from the reference layer to the free layer, this will favour parallel magnetic configuration. On the contrary, if electrons flow from free layer to reference layer, this will favour antiparallel configuration. For reading out the information, a lower current is used so that the resistance state can be determined but without inducing a switching of the storage layer magnetization. Experimentally, current induced magnetization switching (CIMS) was first confirmed in spin-valves with non-magnetic conductive Cu spacer [72,73]. Later, with the improvement in MTJ growth and ability to make MTJ with thinner barrier, CIMS was also observed in MTJ with an insulating spacer [74]. Apart from its great scientific interest, this STT phenomenon raised a considerable interest also for industrial applications since it provides a new way to manipulate the magnetization of magnetic nanostructures with much lower energy and much better spatial resolution than with field writing. Initially, the first experiments of CIMS were performed on systems with in-plane magnetization. The shape of the dot was chosen to be elliptical to induce shape anisotropy and thus induce an anisotropy in the free layer. However, very soon, scalability evaluations predicted that shape-induced anisotropy with in-plane magnetized layer, would not be sufficient to counterbalance magnetic thermal fluctuations at cell dimensions below 50nm. Similarly to the situation in HDDs technology, it was then proposed to switch from in-plane magnetized layer to out-of-plane magnetization in order to reinforce the magnetic stability of the storage layer [75–77].

Furthermore, it led simultaneously to a reduction of writing current density for at same thermal stability factor and more simple nanofabrication process since the cell could be then patterned in circular shape which is simpler to fabricate than elliptical shape. More details on STT-physics, technology and applications can be found elsewhere [78].

### 2.3.2. Focus on thermally-assisted MRAM (TA-MRAM)

A very promising approach to solve the selectivity issue as well as the dilemma between memory retention and its writability was proposed by SPINTEC in early 2000, using thermally assisted writing in so-called thermally assisted MRAM (TA-MRAM) [79,80]. The concept consists in using a temporary heating of the cell during write, produced by a pulse of current flowing through the barrier, to reduce the barrier for magnetization switching. Once the magnetization of the storage layer has switched either thanks to a pulse of field or to STT, the heating current is switched off and the cell cools down in its new state. Once at the standby temperature, the storage layer magnetization is very stable. The concept was implemented at SPINTEC on MTJ comprising an exchange bias storage layer. Let's mention that along the same idea, a method proposed by Daughton [81] employed low Curie temperature F with induced shape anisotropy to achieve thermally assisted writing.

To better understand the principle of TA-MRAM, let us first describe the writing principle of the device. The device consists of a MTJ comprising an exchanged bias pinned layer, pinned by an antiferromagnetic layer with high blocking temperature (typically PtMn with blocking temperature of the order of 350°C) and an exchange biased storage layer pinned by an antiferromagnetic layer with moderate blocking temperature (typically FeMn or IrMn with blocking temperature in the range 150°C-230°C). In Figure 2.10, the writing sequence is represented. In the initial state (1), the storage layer (red horizontal arrow) is exchange-coupled and pointing to the left. The MTJ is then in its high-resistance state corresponding to antiparallel configuration. In order to write logical "0" i.e. low resistance state, the storage layer has to be reversed to the opposite direction. To do so, the system is heated above the storage AF's $T_B$, thus breaking AF order (2) and consequently unpinning adjacent F-layer. The maximum reached temperature is typically of the order of 230°C i.e. high enough to unpin the storage layer magnetization but low enough so that the reference layer always remain pinned in the same direction. At this stage, the F layer becomes free to rotate. The storage layer magnetization can then be switched either by magnetic field or by STT. In the first approach developed at SPINTEC and pursued by the Crocus Technology company, the magnetization of the storage layer is switched by magnetic field. It is worth mentioning that due to the dimensions of MTJ at the nanoscale, the heating process is extremely fast (within 10ns). Thus, in practise, both electric current pulse and magnetic field are applied almost simultaneously. The cell is then cooled down in presence of H from above the storage layer AF $T_B$. The AF then restores its order and couples again with the F-layer magnetization which now lies in the newly written direction. In this way, the system comes back to the stable state. Clearly, in this TA-MRAM approach, the write selectivity originates from a combination of heating due to the current flowing through the cell and field application. As a result, only one field line is required. For the reading, a lower current flowing through the MTJ is used to determine the cell resistance but low enough not to perturb the information by excessive heating or STT switching.

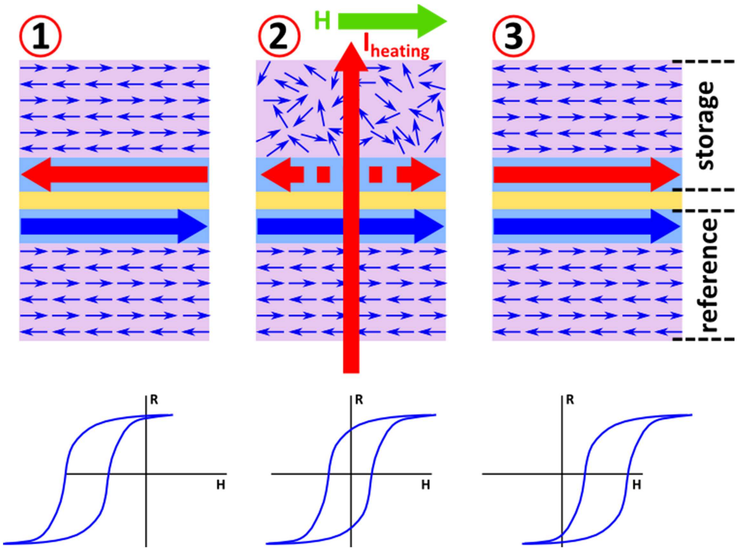

**Figure 2.10**

*Thermally assisted writing approach with 1 -initial state, where the F layer of the F/AF storage layer arbitrary points to the right; 2 – field cooling procedure with i) a heating current pulse (red arrow) above the F/AF $T_B$ to unpin the adjacent F-layer and ii) a magnetic field (green arrow) to reverse the magnetization of the F layer and 3 – final state where the F layer of the F/AF storage layer now points to the left (i. e. reversed). Note that during this all process, the reference layer is not at all affected.*

As previously mentioned, the write process can result from a combination of thermal assistance and field application or from a combination of thermal assistance and STT. In Figure 2.11, the two switching mechanisms are compared. The main difference between these two write approaches is the absence of a field line for the STT switching. In thermally assisted STT-MRAM, the same pulses of current are used to both induce the heating of the storage layer enabling the switching of its magnetization and exert a STT influence on its magnetization to make it switch in the desired direction. The heating is almost independent on the current direction whereas the STT changes sign depending on the current direction.

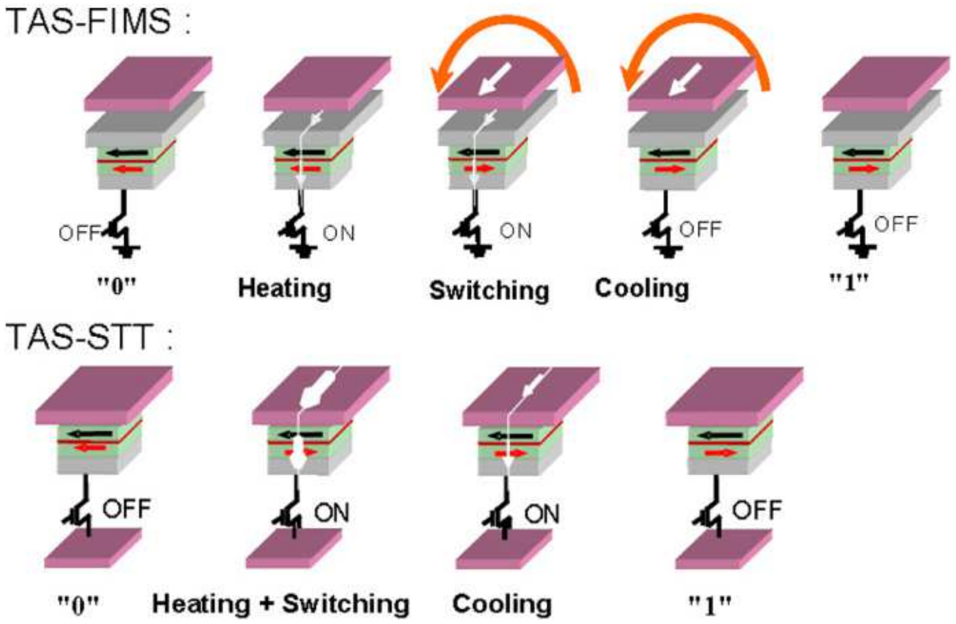

**Figure 2.11**

*Comparison of two thermally assisted switching principles: (top row) – FIMS; (bottom row) – STT. As it can be seen, for the STT switching the current pulse has two combined function – to heat the AF-layer and reverse the F-magnetization direction. After* [82].

Summarizing, this double EB sandwich employed for TA-MRAM allows reducing the number of current lines required to generate the write field from two orthogonal arrays as in toggle MRAM to one array (or even avoid field lines as in case of STT switching). Thanks to the coupling to the AF layer with high anisotropy, the F layer magnetization is very stable in standby down to very small cell size of the order of 20 nm. The memory retention is above 10 years, which is ensured by the AF high anisotropy energy barrier > $70k_bT$. The good data retention and robustness against perturbating fields can be enhanced by insuring that the storage layer exchange-bias field is larger than its coercive field so that only one remanent state exists at zero field at standby temperature. The greater the $H_E$ in comparison with $H_C$, the more robust the device will be. In addition, when the writing is achieved by combining heating with pulse of magnetic field, the field can be shared between all bits of a same word. As a result, a whole word (for instance 32 or 64 bits) can be written with only two pulses of magnetic field. To do so, all “0” are written at once with a first pulse of magnetic field combined with the simultaneous heating of all the bits which have to be written to “0”. Once these bits have cooled down, all bits which have to be written to “1” are heated and a pulse of magnetic field in the opposite direction is applied to all the bits of the word. The heated bits then switch to “1”. This approach greatly minimizes the power consumption in TA-FIMS MRAM as compared to toggle MRAM.

Great progress has been achieved in the development of TA-MRAM and STT-MRAM over the past ten years. The microelectronic industry is mostly focused on STT-MRAM development with the promises of DRMA replacement and SRAM L3 replacement. This would represent a huge market. Towards this goal, progresses were made to reduce the write critical current [72,83,84,85,86] with the aim to lower the write voltage as compared to the tunnel barrier dielectric breakdown voltage [85]. Also, the transistor dimensions are directly dependent on the write current that it needs to deliver (the larger the current – the bigger the transistor). To address these issues, the STT switching must be achieved at lower currents [86] by enhancing the STT efficiency the resistance of the MTJ must be lowered [72]. Improvements along these lines were obtained by $M_S$ reduction by using CoFeB [87] layer, or decreasing the volume [88] of the magnetic layer, or choosing materials with low Gilbert damping such as Heusler alloys. The change to out-of-plane magnetized MTJ has also been a great progress in STT-MRAM development since, as already mentioned, for a similar thermal stability factor, the current density required to switch by STT in perpendicular MTJ is much lower than for in-plane magnetized MTJ. Another point which still needs to be improved concerns the dot to dot variability associated with the patterning of MTJs. For instance, TMR, RA and $J_C$ cell to cell dispersions arise in particular from damages during etching process. These dispersions are still too large for Gbit density memories. Further work on etching of MTJ is still needed [91, 92].

More specifically, concerning TA-MRAM, the remaining issues are the followings. Since the heating serves to unpin only the storage layer, the reference must be stable at the maximum write temperatures. Considering that the blocking temperature in AF are distributed due to grain size distribution, this means that the minimum $T_B$ of the reference layer must be much larger the maximum $T_B$ of the free layer which implies that the two $T_B$ distributions must be well separated. In this regards, one has to consider that these $T_B$ are time dependent i.e. they depend on the heating pulse duration. Usually, PtMn is used for the reference layer since it has a high $T_B$ measured in quasistatic regime in the range ~300C [90] to 400C [91]. Concerning the storage layer exchange bias, the latter should be chosen high enough compared to the operating temperature range of the MRAM so that the retention is still within the specification at the maximum operating temperature. However, it should not be too high not to get too close to the reference layer blocking temperature and to avoid to excessively heat the MTJ at each write event which would increase the power consumption during write and may gradually damage the MTJ stack. The dispersion of exchange bias field from dot to dot has also to be reduced to avoid unexpected writing while current passes to generate a pulse of field along multiple bits of a same word. Only if the exchange bias distribution is narrow enough so that the smallest exchange bias field is still larger than the coercive field, the concept of field sharing can work. FeMn or IrMn are the most commonly used AF materials for the storage layer, because of their intermediate blocking temperatures. Although the $T_B$ and $H_E$ can be further tuned by varying the thicknesses of F and AF layers [33,92], these materials not always satisfy the industrial needs and other AF materials or combination of these materials may be necessary. Another important desirable feature of the storage layer AF material is the thermal variation of its exchange bias field. In most cases, exchange bias decreases almost linearly with temperature. It would be much preferable if one could find an AF material for which the exchange bias field decreases in a concave way with temperature i.e. slowly over the operating temperature range and abruptly around the write temperature. Composite antiferromagnetic layer may allow us to achieve this as will be shown further.

## 2.4. Issues to be dealt with in the present thesis

To sum up, some technological applications such as MRAM, involve patterning full sheet wafers into matrix of individual cells. Industrial products qualification like those made by CROCUS Technology imposes stringent requirements on the distributions of the magnetic properties from cell to cell, including those related to EB. It was supposed few years ago [38] that randomly spread spin-glass like regions at the F/AF interface or within the bulk of the AF layer significantly contribute to the distributions of EB properties. As detailed earlier, these regions result from frustrations of exchange interactions due for example to interfacial roughness, structural defects, peculiar AF spin structure, interdiffusion of species, and grain boundaries in the case of polycrystalline films. The following hypothesis was made [38]: by nature, these frustrations are randomly spread over the wafer and thus over the memory cells after nanofabrication as sketched in Figure 2.12. As opposed to cells with few spin-glass like regions, cells with more of such regions show a weaker hysteresis loop shift at room-T and are more prone to thermal activation since the F/AF interfacial coupling is disrupted on a large part of the cell area. Ultimately, these cells lose their spin reference direction and correlatively fail. Here are the issues that were treated in this thesis: factually proving the link between spin-glasses spread over ferromagnetic/antiferromagnetic thin films and bit-cell dispersions of exchange bias in corresponding TA-MRAM. This is the object of (section 4.2). Prior to that we need to consolidate the origin of the spin-glass like regions and more specifically the role of Mn-diffusion: in Section 3.1 Mn-diffusion is directly observed and then a solution to reduce Mn-diffusion and consequently to minimize the amount of spin-glass is shown: it consists in adding barriers to the diffusion. Another way to tune the amount of spin-glass like phases consists in mixing antiferromagnets. All at once, this last solution also tunes the grains thermal stability and we will see in Chapter 4 that this is yet another problem to deal with. Finally, and to close the loop, mixed antiferromagnets were the mean chosen to tune the amount of spin-glass like phases and to prove their link with bit-cell distributions.

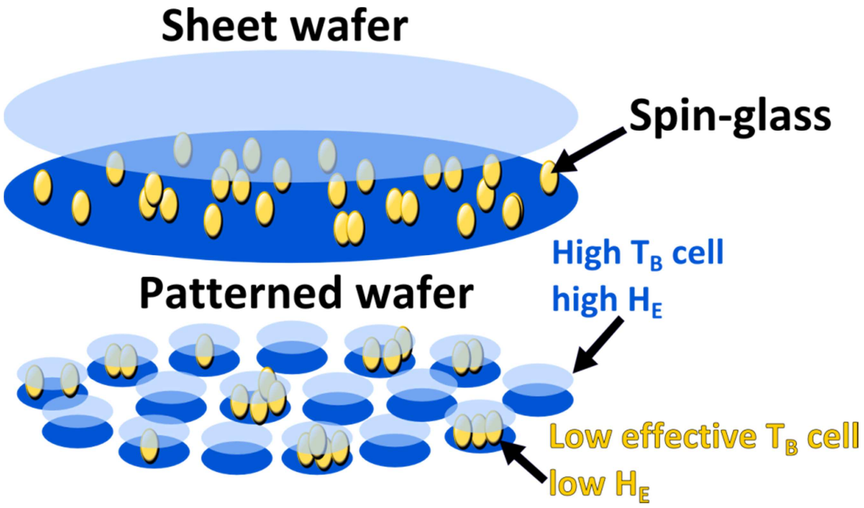

**Figure 2.12**

*Intuitive picture showing the spatial dispersion of spin-glasses (yellow) over the surface of the sheet wafer (top); and resulting cell to cell dispersions after patterning the sheet film into a device (bottom). We believe, that pillars with lower amount of spin-glasses will show higher $T_B$ and $H_E$. Adapted from* [93].

# Chapter 3.

# Minimizing the amount of spin-glass like phases

In this chapter, the discussion is slightly outfocused and shows direct imaging of thermally activated Mn-diffusion. This will be of use for the further interpretation of the Mn content influence on the F/AF spin-glasses. Throughout, when not mentioned otherwise, the error bars are within the symbols dimensions.

## 3.1. The role of Mn in the formation of spin-glasses

### 3.1.1. Direct imaging of Mn diffusion using atom-probe tomography [1]

This subsection is based on the work made in collaboration with the University of Rouen. In particular, the atom probe tomography experiments were performed by our colleagues at Rouen. Although my contribution to this part was small, it is included here since these results are of importance for the understanding of the mechanisms of Mn diffusion that were shown to be one of the main sources of F/AF spin-glass like regions [93] and that will be of use throughout. Below is the paper from this collaborative work [1].

It was discussed earlier that the field of spintronics uses magnetic multilayers for a number of applications [94]. The multilayers most often employ: i) ferromagnetic(F)/antiferromagnetic(AF) exchange bias (EB) interactions [20,25] to set the reference direction required for the spin of conduction electrons but also ii) magnetic tunnel junction orbital symmetry dependent tunnelling from one F electrode to a second F electrode across a crystalline tunnel barrier (usually MgO) to obtain a tunnel magnetoresitance output signal [51]. Various thermal treatments are required to functionalize these magnetic multilayers, e.g., field cooling to set exchange bias and annealing to crystalize amorphous F electrodes around the tunnel barrier. This may result in interdiffusion at the atomic scale [95] and deteriorate the magnetic properties [95–97]. In particular, a great deal of work relates Mn diffusion to annealing temperatures in typical magnetic tunnel junctions [97,98]. Essentially, it is known that Mn atoms diffuse toward the tunnel barrier (AlOx or MgO). As a consequence of Mn impurities around or in the tunnel barrier, the tunnel magnetoresistance of the magnetic tunnel junctions can be greatly reduced. Oxygen-assisted diffusion was proposed as the most likely Mn diffusion mechanism [98,99]. Here, we will pay attention on the thermally activated diffusion specifically activated by the exchange biased electrode with no oxidation-enhanced Mn diffusion (i.e. without AlOx or MgO tunnel barrier in the vicinity). In this context, the precise localization of the atoms at the sub-nanoscale and the subsequent deep understanding of the physics of thermally activated interdiffusion in magnetic multilayers is crucial. Although many techniques are available for chemical analysis, like high-resolution transmission electron microscopy (HRTEM), energy dispersive (EDS) and electron energy-loss spectroscopy (EELS), atom probe tomography (APT) provides a complementary approach to investigate phase transformations and diffusion at the sub-nanoscale since it is an analytical microscope able to map out the three dimensional (3D) spatial distributions of atoms with 0.1 and 0.3 nm depth and lateral resolutions respectively [100–103]. This technique is based on the combination of laser- and field-assisted evaporation of surface atoms. The evaporated atoms are collected by a time-resolved and position-sensitive detector for chemically resolved 3D reconstruction. From that, concentration profiles can be computed anywhere across the analysed volume.

In addition, we note that in polycrystalline thin-film structures, the effects of diffusion are determined by lattice (DL) and grain boundaries (DGB) diffusion constants. When DGB >> DL, in the Harrison type C regime [95], grain boundaries short circuit atomic diffusion. In contrast, diffusion occurs along grain boundaries first and then within grains when DGB > DL: this is the Harrison type B regime [95]. Finally, in the type A regime [95], atoms diffuse both vertically through interfaces and laterally from the grain boundaries toward the inner parts of the grains when DGB ≈ DL. In particular, APT already proved relevant to directly image preferential diffusion via grain boundaries, e.g. for NiFe/Cu [104], Cu/Co [101] and Pt–Rh–Ru [105] layers. Here, we study the physics of diffusion in Cu/Co/IrMn/Pt exchange bias structures with various thicknesses of Pt cap. APT images are correlated to the films' exchange bias properties at different steps of the diffusion, i.e. after various annealing conditions. We expect to resolve interdiffusion both at interfaces and within grain boundaries in order to understand the significant impact of the topmost capping layer on the magnetic properties.

For this study, Ta (3 nm)/[Cu (3 nm)/Co (3 nm)/IrMn (7 nm)]n/Pt ($t_{Pt}$) structures are deposited by dc-magnetron sputtering with an Ar pressure of 2.5 × 10-3 mbar onto thermally oxidised silicon substrates, Si/SiO2//. Co (3 nm) is the F layer and IrMn (7 nm) is the AF layer made from an Ir20Mn80 target. The Ta (3 nm)/Cu (3 nm) bilayer is used as buffer and the top Pt film is the capping layer preventing the stack from oxidation in air. Its thickness $t_{Pt}$ is varied and equals 2 and 80 nm. Note that, the substrate holder temperature is monitored and remains around 16°C during the whole deposition process. Yet, the incoming atoms during deposition may temporarily rise the temperature of the already deposited surface layer before thermalization. Such a potential rise in temperature would not be visible when recording the substrate holder temperature since the inertia of the substrate holder and massive surroundings it is connected to is much larger than that of few hot atomic layers. The sputtering targets are only powered between 50 to 100 Watts to ensure minimum temperature rise of the layers during deposition. The Ta, Cu, Co, IrMn and Pt deposition rates are: 0.14; 0.22; 0.11; 0.17 and 0.26 nm/s, respectively. Room temperature EB is set by post-deposition field cooling (FC) of the samples for 60 min in a resistive furnace from an initial temperature $T_{init}$ down to room temperature, with $T_{init}$ = 250, 400, 450, 500°C. The vacuum level during annealing is set to 10-6 mbar [36]. The positive magnetic field during cooling is applied in the samples planes and its amplitude of 2.5 kOe is large enough to saturate the Co layers. Following this initial FC, all the AF entities with a blocking temperature ($T_B$) larger than room temperature are oriented toward the positive direction [21,36,105]. Room temperature hysteresis loops are then measured along the FC direction by vibrating sample magnetometry (VSM). Following that, standard Ga focused ion beam (FIB) preparation is used. The resulting sharp needles are mounted on holders for laser assisted APT experiments in order to extract, at the nanoscale, the three dimensional spatial distribution of the various atomic species: Cu, Co, Ir, Mn, and Pt. Details of the FIB preparations and APT measurement method can be found in [35,100,106]. Although the base structure of interest contain a single repetition (n=1) and given the small thickness of the layers, 7 repetitions were used to ease the analysis of the APT measurements. Also in an attempt to ease the APT measurements, a thick cap was used to avoid deterioration of the top Cu/Co/IrMn layer during FIB thinning process. Given that, only the Si/SiO2//Ta (3 nm)/[Cu (3 nm)/Co (3 nm)/IrMn (7 nm)]7/Pt (80 nm) samples with various $T_{init}$ were measured by APT [35]. We will see further down that this will suit to interpret both cases: $t_{Pt}$ = 2 and 80 nm. Here, APT analyses are performed with a flexible tomographic atom probe (FlexTAP from CAMECA) at 80K, using a 342 nm laser with 350 fs pulses and a 36° collection angle for optimal mass resolution. The analyses being made with a wide angle, which corresponds to a wide surface (typically 100x100 nm$^2$), the layers are deformed at the edges of the analysed volume. However, flat layers (and thus flat interfaces) can be obtained on a 30x30 nm$^2$ surface. The scaling of the APT data sets was performed by considering the Pt cap (111) planes that were systematically identified by field ion microscopy. This latter technique gives information on the crystallography of the sample under investigation.

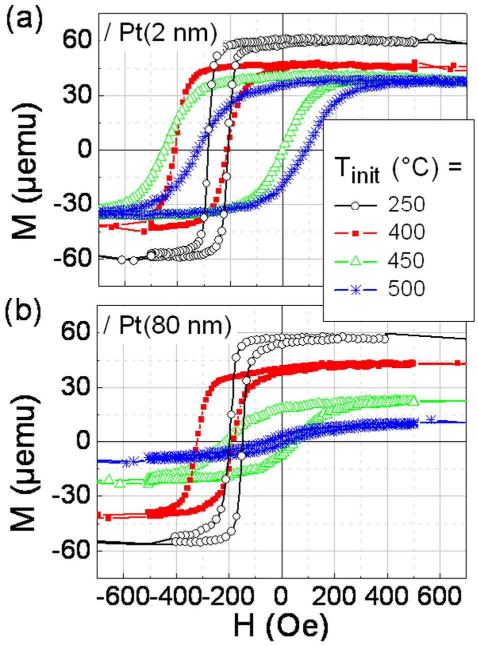

**Figure 3.1**

*Hysteresis loops measured at room temperature by VSM along the field cooling (FC) direction for samples with composition: Si/SiO2//Ta (3 nm)/Cu (3 nm)/Co (3 nm)/IrMn (7 nm)/Pt ($t_{Pt}$) with a Pt thickness $t_{Pt}$ of (a) 2 and (b) 80 nm and for various initial field cooling (FC) temperatures, $T_{init}$. The samples are FC from $T_{init}$ for 60 min down to room temperature (~ 25°C) with $T_{init}$ = 250, 400, 450, 500°C.*

Figure 3.1 shows room temperature VSM hysteresis loops for the Si/SiO2//Ta (3 nm)/Cu (3 nm)/Co (3 nm)/IrMn (7 nm)/Pt ($t_{Pt}$) samples FC from various $T_{init}$ and with $t_{Pt}$ = 2 and 80 nm. For both Pt cap thicknesses, above $T_{init}$ = 400°C, the exchange bias loop shift $H_E$ reduces, the saturation magnetization $M_S$ decreases and the magnetizations reversals become smoother and smoother. In addition, from Figure 3.1, it is striking that the thermally activated modifications of $H_E$, $M_S$ and hysteresis loops shapes evolve much faster for the 80 nm Pt cap. In the following of the article, we use the APT results to enlighten these two facts: i) the thermally activated modifications of magnetic properties, common to $t_{Pt}$ = 2 and 80 nm and ii) the differences between $t_{Pt}$ = 2 and 80 nm with regards to the modification rates. The magnetic properties will be further discussed at the end of the paper in view of the APT data.

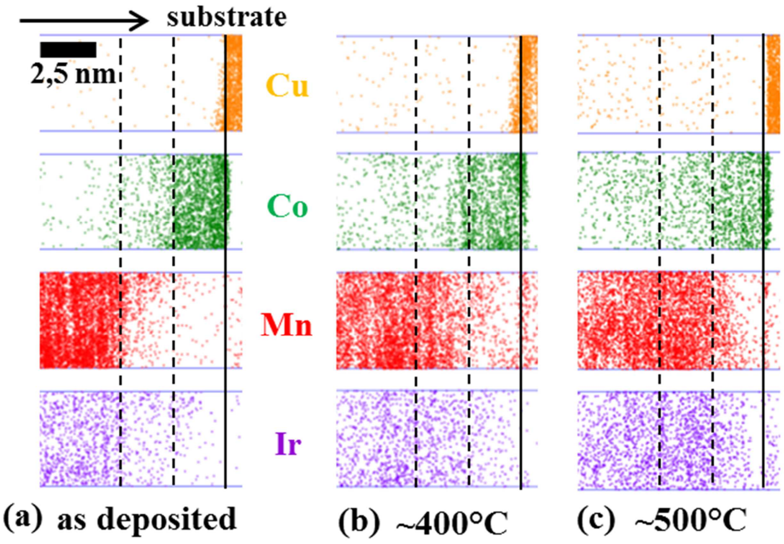

**Figure 3.2**

*Atom probe 2D projection of the 3D-reconstruction corresponding to the spatial distribution of Cu, Co, Mn and Ir atoms in a /Cu (3 nm)/Co (3 nm)/IrMn (7 nm)/ sub-repetition: (a) as-deposited state and after annealing from* $T_{init}$ *for 60 min down to room temperature with (b)* $T_{init}$ *~ 400°C and (c)* $T_{init}$ *~ 500°C. For the sake of clarity, the atoms projections are plotted separately although they superimpose in the sample. The straight line indicates the sharp Cu/Co interface whereas the dashed line delimitate the diffused Co/IrMn one. The scale marker in (a) is common to (a), (b) and (c) and for the three images, the total depth is 9 nm. The images cross-section is 5x5* $nm^2$.

Figure 3.2 shows a 2D projection of the 3D reconstruction after APT analysis and Fig. 3 shows the corresponding concentration profiles. The reconstruction is focused on a /Cu (3 nm)/Co (3 nm)/IrMn (7 nm)/ sub-stack of a Si/SiO2//Ta (3 nm)/[Cu (3 nm)/Co (3 nm)/IrMn (7 nm)]7/Pt (80 nm) sample. This sub-stack is the second of the 7 repetitions from the cap and is typical of all the sub-stacks and interfaces except for the last IrMn (7 nm)/Pt (80 nm) interface. A special focus on this IrMn (7 nm)/Pt (80 nm) interface will be discussed further down. Figure 3.2(a) shows that the Co/IrMn interface is already diffused as deposited [107]. A sub-density at the Co/IrMn interface can be observed. This is due to the difference in the evaporation fields of the IrMn and Co layers (34 V/nm and 37 V/nm, respectively) [108]. This effect is much less pronounced for the annealed samples, Figure 3.2(b) and (c), because the Co/IrMn interface is smoother compared to the as-deposited samples. Intermixing during the deposition process is in part ascribed to physical reasons (like impact-induced exchange events, which involve many parameters such as the incident kinetic energy of the adatoms, surface roughness and chemical bond energy of the underlying layer) and in part to chemical reasons (affinity between elements and tendency to form compounds). The incoming atoms during deposition may temporarily rise the temperature of the already deposited surface layer before thermalization. From Figure 3.2(b)-(c) we observe that further annealing the sample significantly increases Co and Mn intermixing. This is more clearly visible in the concentration profiles plotted in Figure 3.3(left column). In particular, the Co profile progressively shrinks as the annealing temperature increases, as indicated by the arrows. Such thermally activated Co-Mn intermixing that increases with temperature certainly contribute to the observed degradations of magnetic properties common to both $t_{Pt}$. Note that both 3D reconstructions (Figure 3.2) and concentration profiles (Figure 3.3 (left col)) show that the Cu/Co interface remains sharp. This is due to the non miscibility of Cu and Co, as deposited, at 400 and at 500°C [109]. Figure 3.2 and Figure 3.3 (left col) also reveal the presence of few Cu atoms in the IrMn layer with a concentration that increases with the annealing temperature due to thermally activated diffusion of Cu atoms from the Cu layer deposited on top of the IrMn and not visible in Figure 3.2 and Figure 3.3. Note that this particular Cu diffusion is specific to the APT samples with n = 7 and is not relevant for n = 1, i.e. for the structure of interest. So these latest data can be discarded when correlating the APT and magnetic results.

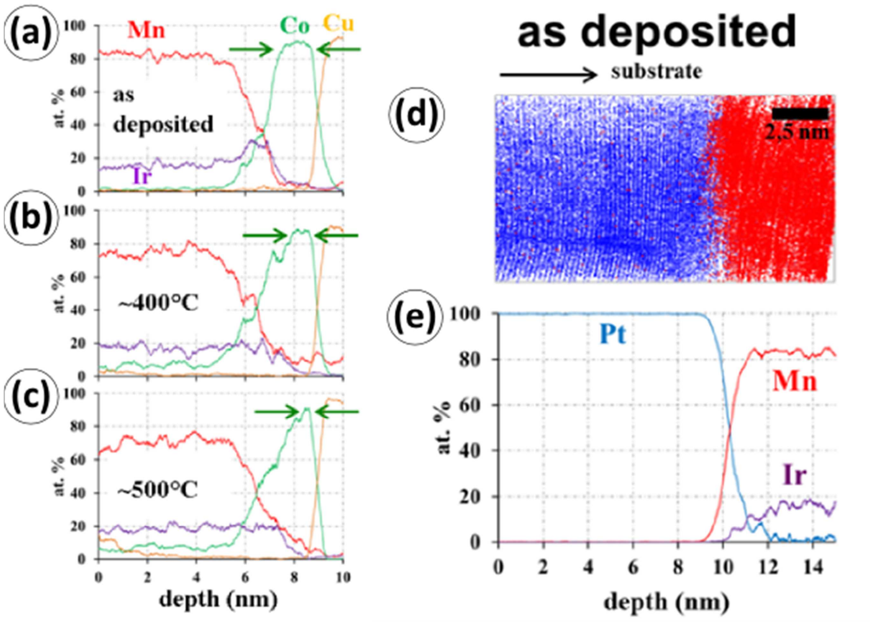

**Figure 3.3**

*Cu, Co, Mn and Ir concentration profiles for /Cu (3 nm)/Co (3 nm)/IrMn (7 nm)/ sub-repetitions: (a) as deposited and after annealing from $T_{init}$ for 60 min down to room temperature with (b) $T_{init}$ ~ 400°C and (c) $T_{init}$ ~ 500°C. The error is estimated to +/- 1%. The cross-section of the region of interest investigated is 5x5 nm2. (d) Atom probe 2D projection of the 3D-reconstruction corresponding to the superimposed spatial distribution of Pt and Mn in the topmost /IrMn (7 nm)/Pt (80 nm) layers as deposited. For the sake of clarity, the Ir projection is not plotted. (e) corresponding concentration profiles, Ir included.*

The following results and discussions aim at enlightening the magnetic differences between $t_{Pt}$ = 2 and 80 nm with regards to the magnetic properties degradation rates. Therefore we now focus on the topmost IrMn (7 nm)/Pt (80 nm) interface. Figure 3.3(right col) shows the 3D reconstruction for the as-deposited multilayer, together with the corresponding concentration profiles. One observes a sharp interface with no Pt-Mn intermixing. In addition, note the well-defined atomic planes in the Pt layer. Note that (111) planes were identified by field ion microscopy, which gives information on the crystallography. We obtained the same results as in Ref. [35] Figure 3.4 shows that, within a grain, IrMn/Pt interface is not affected by annealing at 400°C. The corresponding concentration profile superimposes to the as deposited case. In contrast, Mn diffusion through Pt grains boundaries is clearly observed. Actually, it is known that, in some conditions: the Harrison type C regime [95], grain boundaries and defects offer paths with enhanced atomic mobility, thereby possibly dominating the atomic transport: DGB >> DL. Here, the APT reconstruction field of view extends over 30 nm along the growth direction, meaning that Mn mobility in Pt grain boundaries is such that the related diffusion length exceeds 30 nm after annealing at 400°C. A concentration profile obtained through a grain boundary [Figure 3.4(d)] shows that the measured Mn concentration is about 7% at the centre of the grain boundary. Considering the accuracy of the reconstruction procedure, and the size of the numerical sampling boxes used to obtain such a concentration profile [110], this measured concentration corresponds to an estimated Mn concentration within the grain boundary of about 28%. The consequences of further annealing at 500°C are shown in Figure 3.5. In such conditions, one now observes Mn diffusion through the IrMn/Pt interface within grains and laterally aside grain boundaries: this is typical of the Harrison type A regime [95]. The distribution of Pt and Mn atoms across the IrMn/Pt interface shows a gradual variation of concentrations, revealing different regions: pure Pt (Z1), $Pt_{75}Mn_{25}$ ($Pt_3Mn$) region (Z2), $Pt_{50}Mn_{50}$ region (Z3). Mn diffusion from IrMn into Pt and the subsequent formation of well-known Pt-Mn phases [111] are in agreement with the larger affinity between Mn and Pt atoms than between Mn and Ir. In other words, the enthalpy of formation of Pt3Mn and PtMn is certainly lower than that of IrMn. Given that, Pt acts as a getter for Mn: the higher the annealing temperature, the more the Mn trapped by Pt and the more Mn-depleted the IrMn layer. Alike oxygen-assisted diffusion for magnetic tunnel junctions when IrMn is close to an oxygen-based alloy (AlOx or MgO) with a lower enthalpy of formation than MnOx [98], we conclude that our observations may relate to platinum-assisted diffusion.

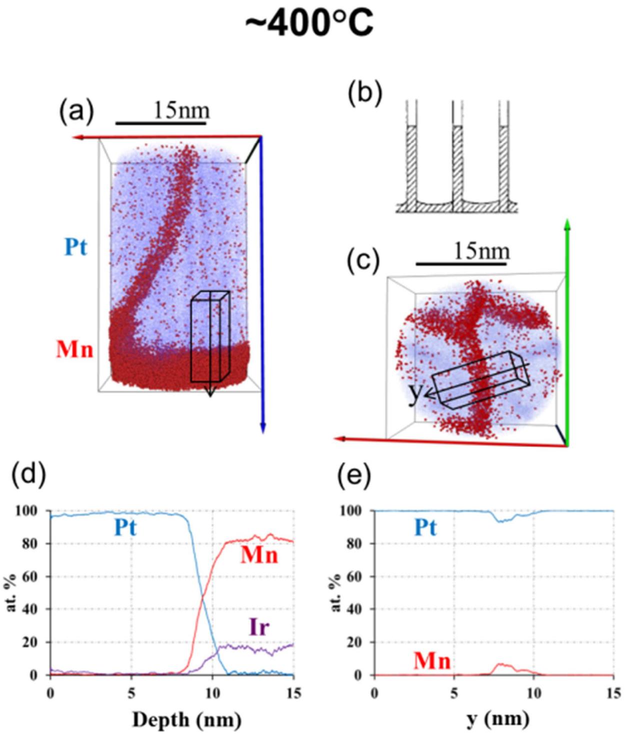

**Figure 3.4**

*(a) Side view of the atom probe 3D-reconstruction corresponding to the superimposed spatial distribution of Pt and Mn in the topmost /IrMn (7 nm)/Pt (80 nm) layers after annealing from ~ 400°C. (b) Corresponding side view sketch after Ref. 5 of diffusion through grain boundaries only and corresponding to the Harrison type C regime [6]. (c) For the same system and annealing conditions, top view of the atom probe 3D-reconstruction. (d) Pt, Mn and Ir concentration profiles extracted from the window plotted in (a). (e) Pt and Mn concentration profiles extracted from the window plotted in (c).*

Given the APT results, we will now re-visit the magnetic results for our Cu/Co/IrMn/Pt polycrystalline thin-film structures. For the two $t_{Pt}$, Figure 3.1 shows that the exchange bias loop shift $H_E$ initially increases when $T_{init}$ rises up to 400°C. The reason of this is likely multiple: i) orientation of the largest AF grains with $T_B$ above 250°C, i.e. in the tail of the $T_B$ distribution since the maximum $T_B$ of our Co (3 nm)/IrMn (7 nm) polycrystalline bilayers is close to 250°C (Chapter 1.3) and ii) thermally activated diffusion favorably resetting the magnetic properties, e.g. increasing the interfacial F-AF exchange coupling and reducing the saturation magnetization $M_S$. Above $T_{init}$ = 400°C, $H_E$ reduces as the likely consequence of further thermally activated intermixing and subsequent negative impact on the magnetic properties of the stacks. In particular, the APT results pointed out Mn diffusion at both Co/IrMn and IrMn/Pt interfaces. Meanwhile, and for similar reasons, $M_S$ decreases and the magnetizations' reversals become smoother and smoother. Concerning Mn diffusion on the Co/IrMn side, our findings agree with and are complementary to earlier Auger electron spectroscopy (AES); Rutherford backscattering spectroscopy (RBS) and VSM studies of Ta/NiFe/Cu/NiFe/IrMn/CoFe/X with X= natural oxidation and Ta [99]. Figure 3.1 also shows that for a given $T_{init}$ $H_E$ is larger for $t_{Pt}$ = 2 nm compared to $t_{Pt}$ = 80 nm. It is possible that the IrMn layer relaxes differently depending on the thickness of the Pt cap. Finally, the fact that the thermally activated modifications of $H_E$, $M_S$ and hysteresis loops shapes evolve much faster for the 80 nm Pt cap agrees with our APT results. These latter show that the capping layer is a reservoir of Pt atoms able to draw Mn out of the IrMn layer: the thicker the cap, the larger the amount of Mn diffusion from the IrMn toward the Pt. With that regards, a faster deterioration of the exchange bias properties for thicker Pt cap is consistent. We note that Pt has been used in the past to limit Co-IrMn interfacial mixing: once inserted between Co and IrMn, it traps the Mn atoms and surely forms a PtMn stable layer thus preventing Co and Mn mixing [106]. Since Pt is miscible with Co [109], for the particular case of Co/IrMn bilayers it will be shown below that inserting (Cu/Pt) dual barrier fulfils the manifold requirements of limiting Co-Mn, Co-Pt and Cu-Mn intermixing which take place when using either no or single Pt and Cu barriers respectively [2].

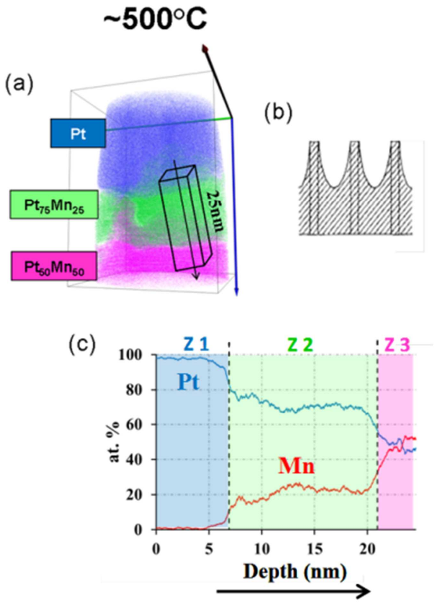

**Figure 3.5**

*(a) Side view of the atom probe 3D-reconstruction corresponding to the superimposed spatial distribution of Pt and Mn in the topmost /IrMn (7 nm)/Pt (80 nm) layers after annealing from ~ 500°C. The atomic compositions indicated refer to the approximate stoichiometry within the grains in the middle of the various phases. (b) Corresponding side view sketch after Ref. 5 of diffusion at interfaces and aside the grain boundaries corresponding to the Harrison type A behaviour [6]. (c) Pt and Mn concentration profiles extracted from the window plotted in (a). The color scheme in (c) is as follows: Pt for xPt>80%, Pt75Mn25 for 80%>xPt>60% and Pt50Mn50 for 60%>xPt with xPt the Pt atomic concentration.*

To conclude, three dimensional spatial distributions of atoms obtained via atom probe tomography analysis of Cu/Co/IrMn/Pt multilayers for various annealing conditions directly revealed the process of gradual Mn diffusion. In particular, on the IrMn/Pt side, it evidenced Mn relocation in Pt grain boundaries. The deteriorations of the films' exchange bias properties upon annealing were correlated to the observed diffusion. More specifically, by drawing Mn out of the IrMn layer, the influence of the amount of Pt atoms in the topmost Pt cap turned out to be crucial. Alike oxidation-enhanced Mn diffusion for magnetic tunnel junctions with AlOx and MgO, our observations may relate to platinum-assisted diffusion. Finally, by knowing the influence of the capping layer, systematic studies could be made in order to find the most robust cap to thermal annealing for IrMn. This is the object of the next paragraph prior to coming back to the issues related to F/AF interfacial spin-glass and to the possible use of Pt or other barriers to trap Mn and avoid its diffusion from the AF to the F and thus to reduce the amount of spin-glass like phases.

### 3.1.2. Further influence of neighbouring getters

The scope of this work is to study the thermal evolution of the magnetic properties as a function of the capping layer materials nature and in particular the evolutions due to thermally activated interdiffusion. Following the study presented above, Ta (5 nm)/Cu (3 nm)/Co (3 nm)/ /IrMn (7 nm)/X ($t_X$ nm) (where X = Pt, Pd, Cu, Ru, Mg, Al and Ta and $t_X$ = 2 and 80 nm), were deposited at room-T by magnetron sputtering onto thermally oxidized silicon substrates, Si/SiO2. Similarly, room-T EB was set by post-deposition field cooling of the samples for 60 min in a furnace from various $T_{init}$ down to room-T. All as-deposited samples have equal dimensions, i.e. the F and AF volumes remain the same. Room-T hysteresis loops were then measured using a vibrating sample magnetometer (VSM) and are shown in Figure 3.6. Further samples have also been made recently and are in the process of being measured in order to discriminate the effect of thermally-activated oxidation of the stacks and thermally-activated interlayer diffusion. These samples have the same composition as the above mentioned samples with an additional 2 nm Pt cap. Although the study is ongoing and the conclusions cannot entirely be drawn, some of the preliminary results are shown and very briefly discussed below. Additional atom probe tomography measurements are also planned to complete the work.

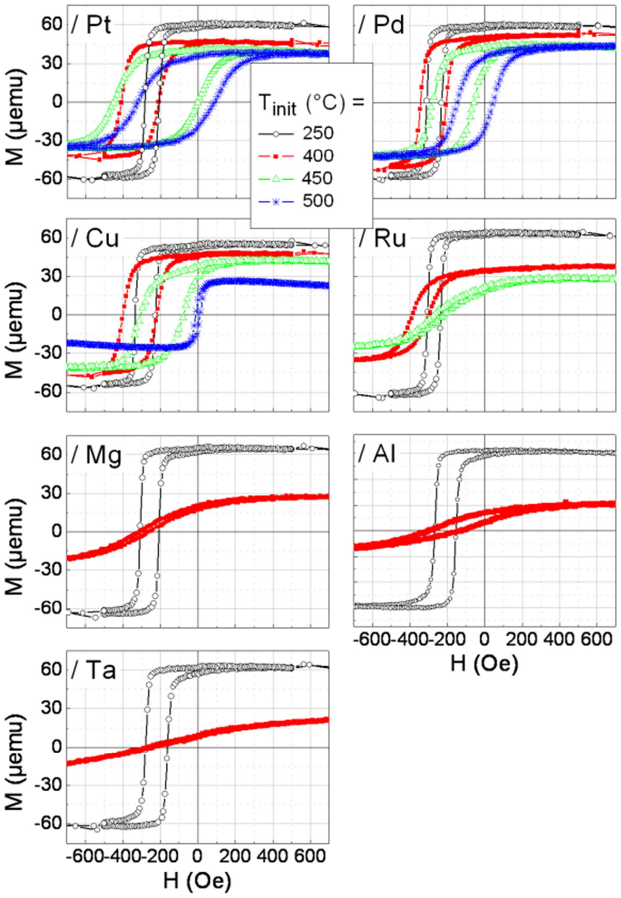

**Figure 3.6**

*Hysteresis loops measured at room temperature by VSM along the field cooling (FC) direction for samples with composition: Si/SiO2//Ta (3 nm)/Cu (3 nm)/Co (3 nm)/IrMn (7 nm)/X (2 nm) with X = Pt, Pd, Cu, Ru, Mg, Al and Ta and for various initial FC temperatures, $T_{init}$. The samples are FC from $T_{init}$ for 60 min down to room temperature (~ 25°C) with $T_{init}$ = 250, 400, 450, 500°C. The data are no more plotted after the magnetic stack becomes paramagnetic.*

For all the caps, when $T_{init}$ is increased, the exchange bias loop shift $H_E$ reduces, the saturation magnetization $M_S$ decreases and the magnetizations reversals become smoother and smoother, as a likely deterioration of the stacks. Pt, Pd and Cu caps seem to be the most robust caps over thermal treatments. It is however hard to conclude here since we observe a mix between interlayer, cap included, mixing and layers oxidation through the cap (except for Pt and Pd). However, the similarity between the Pt and Pd-cap intuitively can be explained due to comparable similar same fcc crystallographic structure and affinity with Pd. Some atom probe tomography works about Pd-Mn alloying are presently ongoing. Concerning the ability of Cu capped samples to resist quite well to thermal activation the situation is more difficult different: on the one side the ability of Cu to draw the Mn atoms depends on the relative affinity of Mn with the surrounding atoms: Ir, Co and Cu and on the other side, this competes with the thermally activated oxidation of the layers and interfaces, since Cu oxidation does not passivate. The preliminary result with a 20 nm cap of Cu compared to a 2 nm cap of Cu shown in Figure 3.7 points to a significant effect due the Cu itself. Essentially, adding a thicker Cu should retard the effects originating from thermally activated oxidation only. Since the opposite occurs, it seems that interlayer mixing plays a significant role with Cu too.

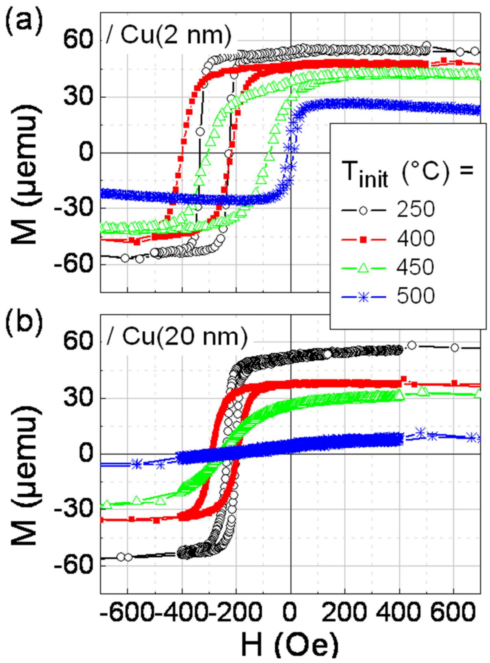

**Figure 3.7**

*Hysteresis loops measured at room temperature by VSM along the field cooling (FC) direction for samples with composition: Si/SiO2//Ta (3 nm)/Cu (3 nm)/Co (3 nm)/IrMn (7 nm)/Cu ($t_{Cu}$) with a Pt thickness $t_{Cu}$ of (a) 2 and (b) 20 nm and for various initial FC temperatures, $T_{init}$. The samples are FC from Tinit for 60 min down to room temperature (~ 25°C) with $T_{init}$ = 250, 400, 450, 500°C. To ease the comparison, the case $t_{Cu}$ = 2 nm is reproduced from Figure 3.6.*

## 3.2. Barriers to the diffusion of Mn

Following the above discussed Mn diffusion, responsible for the formation of interfacial spin-glass-like entities, we introduced a barrier preventing the entities migration. In this part of the manuscript a systematic study of barriers composed of various materials is presented and was recently published [2].

### 3.2.1. Dual barriers [2]

Diffusion barriers have been commonly implemented in the field of electronics [112–114]. Although the science of diffusion barriers involves many aspects which often lead to compromise [112], one of the major difficulties is that the barrier must not corrupt the surrounding materials that it is supposed to be protecting. Some barriers may consist of multiple layers to accommodate such a need for non-reactivity [113,114]. Here, we implement diffusion barrier and in particular dual barriers for the F/AF building block of spintronics devices. In particular, we focus on F/AF cobalt/iridium-manganese (Co/IrMn) based stacks. The blocking temperature distributions ($DT_B$) are used to quantify the interfacial quality of the F/AF interface. We expect that inserting a copper/platinum (Cu/Pt) dual barrier between Co and IrMn will fulfil the manifold requirements of limiting the various species intermixing which take place when using either no or single barriers [27,107,109,111,115–119] and that this will translate into less glassy interfaces, i.e into the observation of lower $T_B$ dispersions.

In this study, Ta (3 nm)/Cu (3 nm)/Co (3 nm)/Cu ($t_{Cu}$)/Pt ($t_{Pt}$)/IrMn (7 nm)/Pt (2 nm) and Ta (3 nm)/Cu (3 nm)/ IrMn (7 nm)/Pt ($t_{Pt}$)/Cu ($t_{Cu}$)/Co (3 nm)/Pt (2 nm) are deposited at room-T by magnetron sputtering onto thermally oxidised silicon substrates, Si/$SiO_2$ [21]. The Ta (3 nm)/Cu (3 nm) bilayer is used as buffer and the Pt (2 nm) film is the capping layer. Co (3 nm) is the ferromagnet and IrMn (7 nm) is the antiferromagnet made from an $Ir_{20}Mn_{80}$ target. The Cu and Pt thicknesses of the (Cu/Pt) and (Pt/Cu) intermixing dual barriers are $t_{Cu}$ and $t_{Pt}$ respectively and take values between 0 and 6 nm. Thick barriers are used here in order to study complete films. Room-T EB is set by post-deposition field cooling (FC) of the samples for 1h in a furnace from 573K down to room-T. The positive magnetic field during cooling is applied in the samples planes and its amplitude of 2.5 kOe is large enough to saturate the Co layers. Following this initial FC, all the AF entities with $T_B$ larger than room-T are oriented toward the positive direction (see Chapter 1.3). Room-T hysteresis loops are then measured. Subsequent initial positive FC is continued from 400 to 4K in the variable T insert of a vibrating sample magnetometer (VSM). $DT_B$ in the range of 4 to 400K are then deduced from hysteresis loops measured at 4K with the VSM after a specific procedure explained in details in Chapter 1.3. It follows by definition that the explanations and terms given in Chapter 1.3 and notations on Figure 1.13 - the variations of the derivative $\delta H_E/\delta T_a$

with $T_a$ represent $DT_B$. Thus: i) an inflection point for $H_E$ vs $T_a$ denotes a peak in the distribution and ii) the amplitude of $H_E$ ($\Delta H_E$) around the inflection is the surface of the peak. In the following, $\Delta H_E$ is the difference between $H_E$ after Ta = 4 and 200K (ie after the inflection, on the plateau).

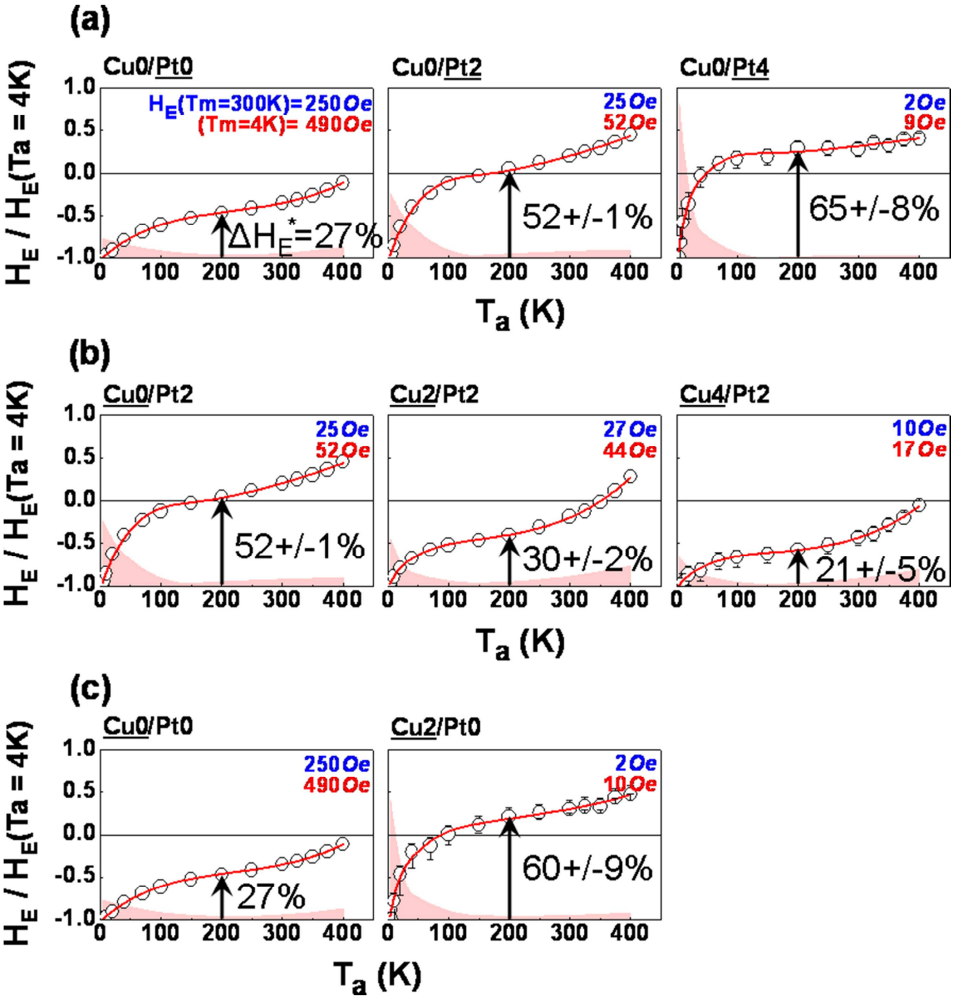

**Figure 3.8**

*Front: variations with the annealing temperatures ($T_a$) of the normalized loop shift ($H_E$ / $|H_E$ ($T_a$ = 4K)$|$) deduced from hysteresis loops measured at 4K by VSM along the field cooling (FC) direction for samples with composition: Si/SiO2//Ta (3 nm)/Cu (3 nm)/Co (3 nm)/Cu ($t_{Cu}$)/Pt ($t_{Pt}$)/IrMn (7 nm)/Pt (2 nm) and subject to a procedure detailed within the text and involving various $T_a$. The Cu and Pt thicknesses of the Cu/Pt intermixing dual barrier are $t_{Cu}$ and $t_{Pt}$ respectively: (a) $t_{Cu}$ = 0 and varying $t_{Pt}$; (b) $t_{Pt}$ = 2 nm and varying $t_{Cu}$ and (c) $t_{Pt}$ = 0 and varying $t_{Cu}$. To ease the reading, the plots in Fig. 1(a) for Cu0/Pt0 and Cu0/Pt2 are reproduced in Fig. 1(b) and 1(c) respectively. The full lines in the graphs result from interpolation of the data. Back: variations with $T_a$ of the normalized derivatives $\delta H_E/\delta T_a$ deduced from the full lines. $\delta H_E/\delta T_a$ vs $T_a$ represent the blocking temperature distributions. The absolute values of HE measured at Tm = 300 and 4K after positive FC from 573K to $T_m$ are indicated.*

Figure 3.8 shows the variations with $T_a$ of the normalized loop shifts, $H_E$ / $|H_E$ ($T_a$ = 4K)$|$ (front) and the corresponding $DT_B$ (back) for Si/$SiO_2$//Ta (3 nm)/Cu (3 nm)/Co (3 nm)/Cu ($t_{Cu}$)/Pt ($t_{Pt}$)/IrMn (7 nm)/Pt (2 nm) with various intermixing barriers. For all the samples, the low-T contribution to $DT_B$ known to originate from AF interfacial spin-glass-like phases (see Chapter 1.3) is fully observed. Given that, $\Delta H_E$ also denotes the glassy character of the surface. This is represented by $\Delta H_E^*$ and arrows in Figure 3.8 and Figure 3.9 and expressed in percentage: $\Delta H_E^*$ equals $\Delta H_E$ normalized to the total expected variations of $H_E$, i.e. 2 for normalized $H_E$: from -1 to 1. The beginning of the second inflection point in the $H_E$ vs $T_a$ variations witnesses the high-T contribution to $DT_B$ related to the grains sizes dispersion. This contribution exists for all the samples since $H_E$ is due to reach back its maximum amplitude but with opposite sign for larger $T_a$, i.e. when all the AF entities are reoriented (Chapter 1.3).

It is known that Co-Mn intermixing exists at Co/IrMn interfaces [107,109,111] and it has been observed that a Pt insertion limits such intermixing [107,111] which should be beneficial for the interfacial quality. However, Pt is not an inert barrier here since it is fully miscible with Co. As a result, CoPt alloys with reduced ordering T around the Co-Pt interface form [107,120]. As a consequence, Figure 3.8(a) shows that, compared to no Pt inclusion, $\Delta H_E^*$ and thus $DT_B$ increases when a 2 nm thick Pt is inserted (from ~ 27 to ~ 65 %). This confirms that the interfacial quality actually worsened. Figure 3.8(a) also shows that the thicker the Pt (0; 2 and 4 nm), the larger the $\Delta H_E^*$ and thus the larger the $DT_B$ contribution (~ 21; ~ 52 and ~ 65% respectively). This implies that the thicker the Pt insertion, the more glassy the interface. It may mean that the Co or Pt diffusion lengths in our experimental conditions are larger than $t_{Pt}$ or $t_{Co}$. Pt and Co diffusions through grain boundaries are also not excluded (See Chapter 3.1.1 and 3.2.2). To avoid Co-Pt intermixing in the case of a single Pt barrier we further added a Cu layer, immiscible with Co [109,121], and obtained a dual (Cu/Pt) barrier. By looking at the plots for (Cu0/Pt2) and (Cu2/P2), Figure 3.8(b) shows that this further Cu insertion indeed reduces $DT_B$ (from ~ 52 to ~ 30%) and therefore increases the interfacial quality. Additionally, Figure 3.8(b) shows that for (Cu/Pt2) dual barriers, the thicker the Cu (0; 2 and 4 nm), the smaller the $DT_B$ (~ 52; ~ 30 and ~ 21% respectively). For similar reasons as above, diffusion length vs film thickness or Co and Pt diffusions via grain boundaries may be argued. It is noticeable that $DT_B$ for a Co/(Cu4/Pt2)/IrMn stack [~ 21 %, see third plot in Figure 3.8(b)], i.e. with an intermixing dual barrier, is smaller than $DT_B$ for a Co/IrMn bilayer [~ 27 %, see first plot in Figure 3.8(b)], i.e. without any intermixing barrier. This thus proves that an efficient inert intermixing barrier is a viable solution to limit the dispersions of $T_B$ in exchange biased stacks, but, as a counterpart, it weakens $H_E$ by taking the F away from the AF [119] (see values in Figure 3.8). However, in Figure 3.8(b), when comparing (Cu0/Pt2) and (Cu2/P2) we remark that the relative changes of $H_E$ are very limited (from 52 to 44 Oe for a measurement T of 4K) despite the addition of as much as 2 nm more between the F and the AF. This result is encouraging and introduces the fact that the benefits of intermixing limitations may, in some conditions, overcome the disadvantages of spacing augment between the F and the AF. Finally, notice that the sole insertion of a single Cu barrier as opposed to a dual (Cu/Pt) barrier leads to larger $DT_B$ and thus to more glassy interfaces, as concluded from Figure 3.8(c) - the case (Cu4/Pt0) virtually gave zero loop shift and no $DT_B$ could be measured. We argue that Cu and Mn are indeed miscible and that CuMn alloys are known to lead to spin-glass phases [27,116–118].

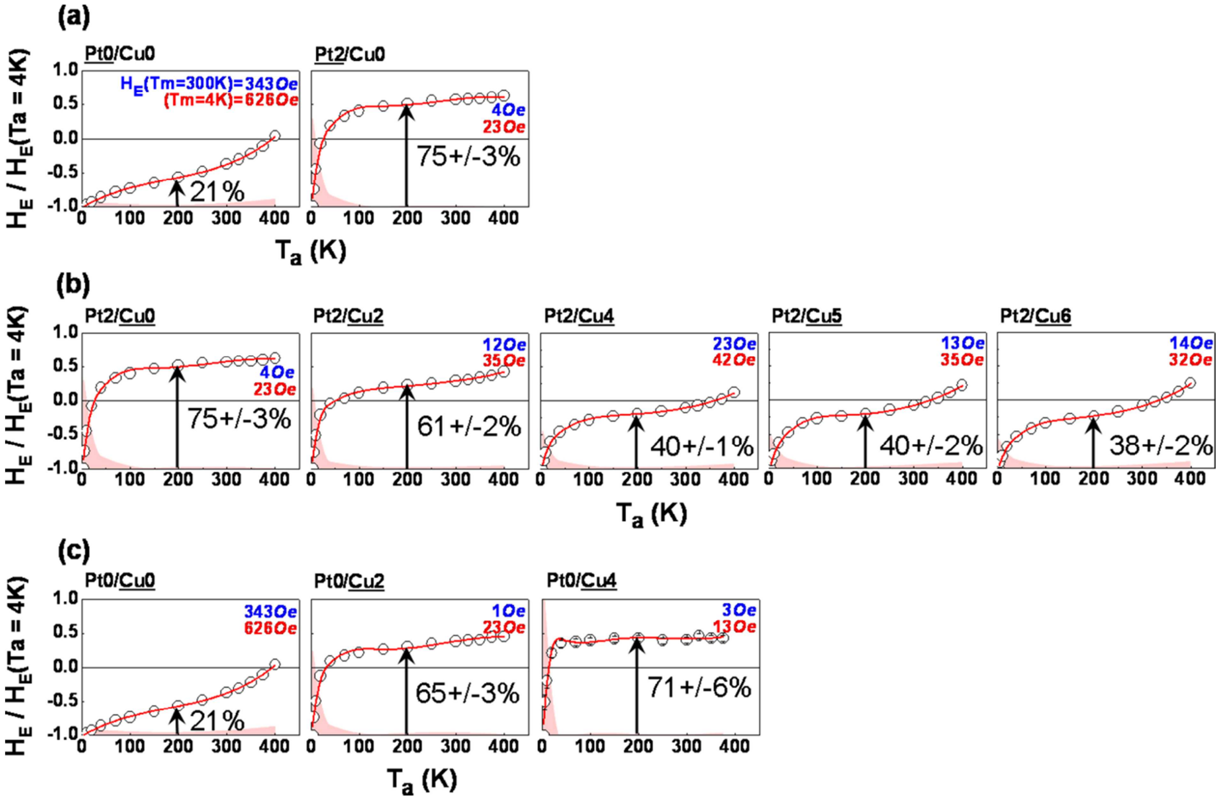

**Figure 3.9**

*Front: variations with Ta of $H_E$ / $|H_E$ ($T_a$ = 4K)$|$ for the inverted structures: Si/SiO2//Ta (3 nm)/Cu (3 nm)/ IrMn (7 nm)/Pt ($t_{Pt}$)/Cu ($t_{Cu}$)/Co (3 nm)/Pt (2 nm) with: (a) $t_{Cu}$ = 0 and varying $t_{Pt}$; (b) $t_{Pt}$ = 2 nm and varying $t_{Cu}$ and (c) $t_{Pt}$ = 0 and varying $t_{Cu}$. The full lines in the graphs result from interpolation of the data. Back: variations with $T_a$ of the normalized derivatives $\delta H_E/\delta T_a$ deduced from the full lines. The absolute values of $H_E$ measured at $T_m$ = 300 and 4K after positive FC from 573K to $T_m$ are indicated.*

In order to strengthen our findings and confirm that the effect is predominantly driven by layers intermixing and not by potential structural or roughness changes we systematically performed measurements for the reversed structures. Figure 3.9 shows the results for Si/$SiO_2$//Ta (3 nm)/Cu (3 nm)/ IrMn (7 nm)/Pt ($t_{Pt}$)/Cu ($t_{Cu}$)/Co (3 nm)/Pt (2 nm). We note that the top and bottom IrMn stacks are certainly not symmetrical due to growth issues (See Appendix 1) on various buffers which influences interface roughness, alloying, layers structures, etc. and affect the $H_E$ absolute values differences between top and bottom stacks [121,122]. For example, although (Cu0/Pt4) and (Pt0/Cu4) based samples gave a non-zero $H_E$, thus allowing $DT_B$ measurements, the cases (Cu4/Pt0) and (Pt4/Cu0) gave zero $H_E$ and thus no $DT_B$ could be measured. The origins of the differences between top and bottom IrMn structures were already studied in the literature and are out of the scope of the present paper. Although the absolute values of $H_E$ and $\Delta H_E^*$ vary between top and bottom IrMn, in agreement with previous results [122] (and Appendix 1), similar trends were obtained after the addition of the barriers thus leading to analogous conclusions. This indeed confirms that our relative observations are predominantly related to intermixing. The barriers addition certainly has other consequences, e.g. on roughness, which surely depend on the top or bottom character of the stack, but such other consequences mainly influence the absolute values differences between top and bottom and not the relative trends for a given top or bottom stack. In brief, Figure 3.9(a) shows the effect of Pt-Co intermixing when adding a single Pt barrier to limit Mn-Co intermixing, which leads to more glassy interfaces and thus to larger $DT_B$ (~ 21 and ~ 75 % for $t_{Pt}$ = 0 and 2 nm respectively). Figure 3.9(c) shows the effect of Cu-Mn intermixing when adding a single Cu barrier, which also leads to larger $DT_B$ (~ 21; ~ 65 and ~ 71% for $t_{Cu}$ = 0; 2 and 4 nm respectively). Finally Figure 3.9(b) confirms the beneficial effect of (Pt/Cu) dual barriers for the reductions of $DT_B$. The corresponding values of $H_E$ and $\Delta H_E^*$ are plotted together in Figure 3.10(a).

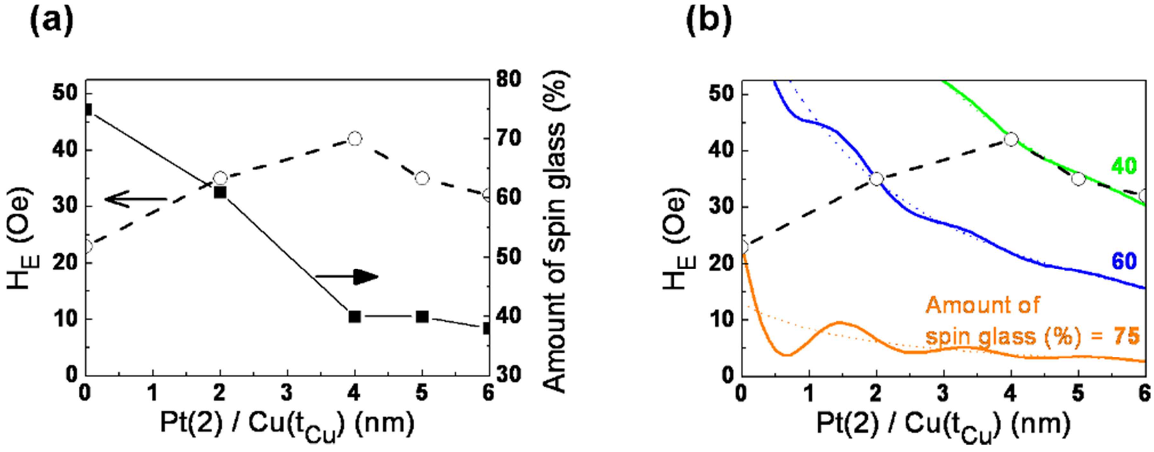

**Figure 3.10**

*(a) Variations of the hysteresis loop shift ($H_E$) measured at 4K and of the relative amount of spin glass deduced from Fig. 2(b) as a function of the Cu thickness ($t_{Cu}$) for samples of Si/SiO2//Ta (3 nm)/Cu (3 nm)/ IrMn (7 nm)/Pt (2 nm)/Cu ($t_{Cu}$)/Co (3 nm)/Pt (2 nm). (b) Comparison of the experimental $H_E$ vs $t_{Cu}$ plot reproduced from Fig. 3(a) (data points and dashed line) with series of expected $H_E$ vs $t_{Cu}$ trends for various relative amount of spin glass, i.e. for various interfacial qualities (dotted full lines in color).*

When the Cu thickness of the (Pt2/Cu) tandem increases, the interfacial quality improves up to a threshold value ($t_{Cu}$ = 4 nm) and levels out above. For our sputtering deposition process (which certainly participate to the activation of some lattice defects within grains [107,111] and post-deposition annealing (at 573K for 1h), diffusion may occur via the core of each grain and via grain boundaries [112] (and/or see paragraph 3.2.2). This may happen up to a threshold thickness larger than the diffusion lengths in the grains and grain boundaries. Actually, it is known that, in some conditions, grain boundaries and defects offer paths with enhance atomic mobility, thereby possibly dominating the atomic transport [112]. We also note that our (Pt/Cu) dual barrier is surely a more complex barrier since Pt and Cu do mix [109]. Attempts with (Ru2/Cu2) barriers in which Ru and Cu are not miscible [109] did not show any $H_E$ probably due to Ru and Mn intermixing and to wetting issues of Cu on Ru. This thus points out the importance of the choice of the materials in the dual barrier even if these latter are miscible between them and provided that they are efficient barriers for the surrounding materials. From Figure 3.10a), we also observe that $H_E$ first increases when the amount of spin-glass decreases (i.e. when the interfacial quality improves) and then reduces when the amount of spin-glass levels out. Figure 3.10(b) helps us to explain this behaviour. First note that the exchange interactions between Co and IrMn through 2 nm of Pt plus 2 to 6 nm of Cu (or more likely through a PtCu alloy) are surely mediated by itinerant *s* electrons [123,124]. To a first approximation this sounds plausible, since the spin diffusion lengths in Pt, Cu and some PtCu alloys can be larger, at 4K, than the above mentioned characteristic lengths [125]. In particular an oscillating behaviour of the magnetic properties for [PtCu-alloys/Co] multilayers [123] was already reported in the literature. Additionally, long range interactions have been modelled and experimentally reported in the literature between a F and an AF, although the spacer did not involve Pt nor a Pt based alloys [31,126–129]. Finally, we attempted (Pt1/AlOx1.4-2/Cu1) trilayer barrier. The total barrier thickness was set to 4 nm so as to compare with the (Pt2/Cu2) dual barrier. No loop shift was obtained (hence no distribution could be measured). Since our AlOx is insulating it may break the IrMn-Co long range interaction. This result probably supports the idea of long range mediation via itinerant s electrons. Note that, in their paper [130] Paul et al studied single AlOx spacer between Co and CoO with incremental thickness within 5nm range. He observed an increase of EB with a peak at $t_{AlOx}$ = 1nm, and a sharp decrease for the thicker layers. This drastic change was explained by transition from AlOx islands at the interface for the thicknesses below 1 nm to collapsing of these regions into a continuous AlOx layer, which diminishes F/AF interaction. Therefore there is an optimal AlOx thickness that establishes bubble-like domain walls, which in turn reflects on the enhanced loop shift, according to proposed model. This result also supports the idea of long range mediation via itinerant s electrons through insulation AlOx layer, responsible for exchange interaction for separated F and AF. Although in their paper Paul et al get EB up to 1.5 nm of AlOx layer thickness (that is a satisfactory condition to consider it as a continuous layer), the total additional augmentation by 2 nm of Pt and Cu layers in our case are likely responsible for the vanishing of the loop shift. Since for the present study, exactly continuous amorphous interlayer is required, in order to prevent Mn migration through the grain boundaries of alloyed Pt/Cu barrier, as will be also be discussed later - the lower thicknesses (of AlOx) not establishing continuous surface coverage cannot be considered as an effective diffusion barrier for the grain boundaries migration. Also, it has been shown, that Mn diffusion mobility can be highly dependent on oxygen concentration [99]. Studies of varied oxidation degrees (from low to high) of AlOx [98] showed that an extent of Mn diffusion increased with oxidation time increment.

In Figure 3.10(b), we plotted a series of oscillatory decreasing loops of the form: $(Ae^{-t/L})/t + B(Ct\cos(Ct) - \sin(Ct))/(Ct)$ [109]. The first term represents the reduction of $H_E$ ascribed to spacing augment between the F and the AF [119] and the second term models additional RKKY long range interactions [123]. These curves are guides to the eye and A, B, C and L have been assigned arbitrary values. B, C and L were kept constant, while A was increased to model an interfacial improvement. The variable t is the total thickness of the dual barrier. This series of virtual master curves reads as follows: the interface gradually improves when switching from the orange curve (75%) to the dark blue (60%) and to the green curve (40%). The interfacial improvement experimentally measured between 0 and 4 nm of Cu [see Figure 3.10(a)] means that the corresponding virtual $H_E$ should jump from master curve to master curve. As shown in Figure 3.10b) this is in agreement with the experimental increase of $H_E$. When the interfacial quality levels out, above $t_{Cu}$ = 4 nm as experimentally observed in Figure 3.10a), the related virtual $H_E$ should stick to the same curve: here, the green curve (40%) in Figure 3.10b). It then follows the decrease due to the gradual separation of the F and the AF, which is also in agreement with the experimental trend. Although adding a diffusion barrier to bare Co/IrMn did not fulfil at once interfacial improvement (ie spin-glass reductions) and preservation of a decent value for $H_E$, for the (Pt2/Cu) series (Figure 3.10a)) we evidenced that, in some conditions and despite the F-AF spacing augment it was possible, via the addition of diffusion barriers, to simultaneously increase $H_E$ and lower the $T_B$ dispersions.

To conclude, the report of layers intermixing at ferromagnetic/antiferromagnetic exchange biased interfaces and concomitant formation of interfacial spin-glass-like phases with reduced properties and increased dispersions led us to engineer diffusion barriers. Cu and Pt based barriers were inserted at Co/IrMn interfaces and the interfacial quality potential improvement was investigated via measurements of the low-temperature contributions to the blocking temperature distributions: the smaller the contribution, the less glassy the interface. The use of (Cu/Pt) intermixing dual barriers led to blocking temperature distributions reductions as a result of interfaces improvements. All at once, (Cu/Pt) limited Co-Mn, Co-Pt and Cu-Mn mixing, which took place when using either no or single Pt and Cu barriers. Although inserting (Cu/Pt) intermixing dual barriers was beneficial for the exchange bias properties dispersions, it weakened the loop shift amplitudes by taking the ferromagnet away from the antiferromagnet. However, some encouraging data suggested that it is in principle possible to find barriers for which the benefits of intermixing limitations overcome the disadvantages of spacing augment between the ferromagnet and the antiferromagnet. Since Cu and Pt are miscible, complementary studies with $Cu_xPt_{1-x}$ barriers would be interesting, although polycrystalline $Cu_xPt_{1-x}$ alloys will also leak at grain boundaries where diffusion may still occur. Other complementary studies could involve amorphous layers in order to avoid diffusion via grain boundaries (See section 3.2.2).

Finally note that thermally activated diffusion processes are obviously time depend. By reproducing $DT_B$ for various waiting time, $t_{wait}$ at $T_{init}$ we observed no significant differences in $\Delta^*$ for $t_{wait}$ ranging between 60 and 180 min (Figure 3.11). Since the results reported above were made for $t_{wait}$ = 60 min we thus conclude that most of the diffusion already occurred by then.

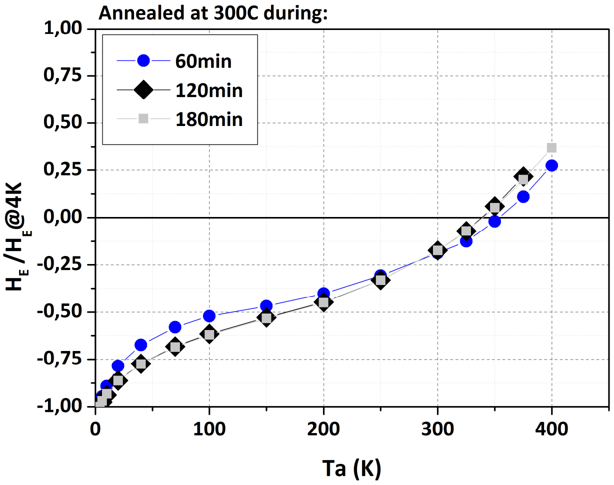

**Figure 3.11**

*Blocking temperature distributions for the same composition after an initial FC from the same initial temperature: $T_{init}$ = 300°C but for various waiting time at $T_{init}$ The overlap of the black and grey symbols evidences that there is no more diffusion evolution between the system annealed for 120 and 180 min. For this measurement, the composition was Ta (3 nm)/Cu (3 nm)/Co (3 nm)/Cu (2 nm)/Pt (2 nm)/IrMn (7 nm)/Pt (2 nm).*

### 3.2.2. Attempt with more complex barriers

The previously shown results for the dual barrier clearly evidenced the interfacial quality improvement by inserting Pt and Cu at the interface between F and AF layers. Although, the dual barrier was beneficial, the possible mechanism of diffusion via polycrystalline CuPt alloy is not discarded. Therefore, in this short subchapter we examined the assumption of Mn entities diffusion via grain boundaries of alloyed dual barrier, by introducing an amorphous layer between Cu and Pt. For additional amorphous [131] CoFeB barrier it was possible to quantify the completed $DT_B$ Figure 3.12(b-d). Two different stacks were chosen, where 1 nm of CoFeB was deposited between Co and Cu Figure 3.12b) and between Pt and Cu with 1.5 nm thickness for both Pt and Cu, The total barrier thickness was again set to 4 nm so as to compare with the Pt2/Cu2 dual barrier. Neither of single CoFeB insertions from Figure 3.12b)-c) showed an improvement of interfacial quality in comparison with pure dual barrier showing $\Delta_2$ equal to 81% and 82% respectively contrary to 61% shown for Pt2/Cu2. Despite the amorphous character of CoFeB, it is likely that B diffuses in the surrounding layers during the initial annealing at 300°C for 1h, hence creating more spin glasses and more amorphous areas. Other amorphous layers or additional barriers to B diffusions may be attempted. In addition, note that the CoFeB temperature/magnetic/and structure behaviour is strongly dependent on large variety of factors. For example, the transition from amorphous to crystal structure of CoFeB grown on top of MgO was found to be at $T_a$ = 360ºC [131,132]. At the same time, it was reported [133], that whether CoFeB is grown and capped with either Ta or Ru, at 250ºC it still remains amorphous for the former seed/cap material and start to crystallize with Ru forming bcc (001) texture, whereas grown on CoFe the texture is bcc (110) [134]. From HRTEM analysis shown [133], the interfacial quality of seed/capping layer was evidenced – sharp Ru interface, contrary to Ta, provide better growth conditions, also the diffusion of boron atoms can be easier established via Ru grain boundaries, rather than amorphous Ta layer. Accordingly, the lack of B and seed Ru-layer structure may promote the partial crystallization of CoFeB at lower annealing temperatures. Again, AF layer grown on top of this multi-layered structure may be affected by preceding layers crystallographic orientation. All at once, being annealed at 300ºC (which is 50ºC higher than reported above) our samples may partially adopt a crystallographic orientation of the layers below thus establish paths for grain boundaries diffusion (rather than being amorphous), the CoFeB thickness of 1 nm may be not enough to prevent the diffusion. All these hypotheses may benefit from X-ray measurements to be pursued in future works.

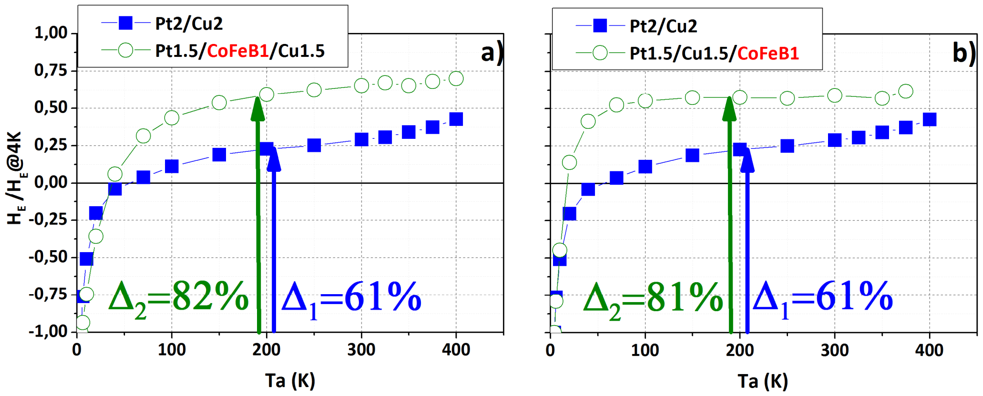

**Figure 3.12**

*Blocking temperature distributions comparisons between Pt (2nm)/Cu (2nm) and (a) Pt (1.5nm)/ CoFeB (1mn)/Cu (1.5nm)(b) Pt (1.5nm)/Cu (1.5nm)/ CoFeB (1mn) diffusion barriers.*

To conclude on this chapter, first we determined the mechanism of Mn diffusion using both magnetic and APT measurements. It was evidenced, that Mn diffusion occurs also via grain boundaries. The following step was to find an appropriate material to insert between F and AF layers to reduce as much as possible the Mn diffusion being responsible for interfacial spin-glass formation. First attempts with a single barrier (Appendix 1) did not show a sufficient improvement of the interfacial quality mainly due to miscibility of materials and growth issues. Then, for Co/IrMn bilayers the introduction of dual Cu and Pt barrier with varied thicknesses showed continuous improvement of the interface because this tandem limited Co-Pt, Co-Mn and Cu-Mn intermixing.

# Chapter 4.

# Insights of spin-glass like phases for applied spintronics

This chapter is divided into two separate parts and connects spin-glass like phases to technological issues: i) factually studying the link between spin-glasses spread over ferromagnetic/antiferromagnetic thin films and bit-cell dispersions of exchange bias in corresponding TA-MRAM. This is the object of the second part of this chapter. ii) another way to tune the amount of spin-glass like phases consists in mixing antiferromagnets, this is dealt with in the first part of this chapter. All at once, this last solution also tunes the grains thermal stability and we will see that this is another technological problem to deal with for TA-MRAM. Finally, and to close the loop, mixed antiferromagnets were the mean chosen to tune the amount of spin-glass like phases and to prove their link with bit-cell distributions in the second part of this Chapter. Somehow, the first part is a preliminary study of continuous films and our assumption for possible technological improvement, whereas the second is a direct inspection of the concept performed on real TA-MRAM devices.

## 4.1. Mixing antiferromagnets to tune TA-MRAM interfacial spin-glasses [3]

These results have been published in [3] and the text of the paragraph is mostly based on this paper. Spintronics thermally assisted magnetic random access memories (TA-MRAM) applications [82] use two ferromagnetic/antiferromagnetic (F/AF) exchange bias (EB) bilayers: one for reference and one for storage (See Section 2.3.2). The blocking temperature ($T_B$) is the temperature (T) above which the F is no longer pinned in a fixed direction by the AF. In particular, $T_B$ increases with the F magnetization sweep-rate and reaches the AF intrinsic Néel-T ($T_N$) in the nanosecond regime [135,136]. For EB storage layer $T_B$ defines the data retention thermal threshold at the device rest-T whereas $T_N$ regulates data writing at the nanosecond. At rest-T, both the reference and storage layers magnetization must withstand thermal activation, i. e. $T_B$ must be much larger than the rest-T. During writing, the TA-MRAM cell is simultaneously heated for a few nanoseconds at a T of about 200°C thanks to a current flowing through the tunnel barrier and subjected to a magnetic field pulse of tens of Oersteds. The reference layer pinned to a high $T_N$ AF (e. g. PtMn; $T_N$ = 700°C [25]) remains unaffected by this. In contrast, the storage layer coupled to a moderate $T_N$ AF (e. g. IrMn and FeMn with $T_N$ in the 200-300°C range [25]) gets unpinned at the write-T so that its magnetization can switch in the applied field direction (Section 2.3.2). Engineering the storage layer thus requires compromises since its critical temperature needs to be adjusted above the rest-T but below the write-T. Too large blocking-T for the storage layer would result in useless increase in power consumption for writing.

AFs used in TA-MRAM are mostly based on PtMn for the reference layer and IrMn or FeMn for the storage one [82,90]. One of the present industrial issues with regards to TA-MRAM is to find a storage layer with intermediate properties between those of IrMn and FeMn and in particular with a blocking-T larger than FeMn for better stability at rest-T but lower than IrMn to reduce power consumption at write-T. Additives like Cr enhance AFs corrosion and stress resistance. To some extent, they also tune the AF $T_N$, the F/AF $T_B$ and the loop shift amplitude ($H_E$) [127–129]. To this adds AF laminations[130] and stoichiometry adjustments in the range where the compounds remain AF [139,141–144]. In conjunction with electrical resistance and dimensions issues, varying the layers thicknesses is another way to enlarge the range of exchange bias properties since for example $H_E$ is inversely proportional to the F thickness and $T_B$ depends on the AF thickness[25]. Yet, most of these adjustments either do not influence the F/AF interface or do not modify the amount of interfacial spin-glass like phases (See Section 1.2.4). The latter play an important role since they play an important role in the cell to cell dispersions after patterning the sheet film [38]. For example, while varying the AF thickness makes no difference on the amount of interfacial spin-glasses, additives surely do. This study is based on results obtained using $DT_B$ procedure (See Section 1.3)

The present study focuses on finding an appropriate AF material for exchange bias of the storage layer in TA-MRAM with intermediate properties between those of IrMn and FeMn. It mixes usual IrMn and FeMn in the form of [IrMn/FeMn] repetitions in an attempt to widen the coverage of available AFs and F/AF properties; interface quality included-for the storage layer of TA-MRAMs. Therefore, in addition to exchange bias loop shifts, the F/AF magnetic interfacial qualities [18,21,27,36,38,145] and the AF grains thermal stability (See Section 1.2.4) were studied via measurements of the low- and high-temperature contributions to the blocking-temperature distributions (See Section 1.3), respectively. We demonstrate that the exchange bias field and blocking temperature distributions can be continuously tuned from those of IrMn to those of FeMn via [IrMn/FeMn] laminations.

For this work, buffer/CoFeB (1.2 nm)/Mg (1.4 nm, naturally oxidized)/F /AF /Ta (5 nm), with F = CoFeB (2 nm)/NiFe (1.5 nm) and AF = IrMn (10 nm), [IrMn (t nm)/FeMn (t nm)]$_{xN}$, [FeMn (t nm)/IrMn (t nm)]$_{xN}$ and FeMn (10 nm), were deposited onto thermally oxidised silicon substrates at room-T by magnetron sputtering [135]. The IrMn and FeMn thicknesses t and the number of repetitions N take the following values so that the total thickness of the AF is constant at 10 nm: (t;N) = (2.5;2) and (1;5). After deposition, room-T exchange bias was set by field cooling (FC) the samples in a furnace from 573K for 90 min down to room-T. The magnetic field applied during cooling is positive, in the sample plane and its amplitude of 10 kOe saturates the CoFeB (2 nm)/NiFe (1.5 nm) F layer. In addition, the T of 573K is large enough so that, following this initial FC, all the AF entities with $T_B$ larger than room-T are oriented toward the positive direction (Section 1.2.4). Hysteresis loops were then measured at room-T. Subsequent initial positive FC is continued down to 4K in a vibrating sample magnetometer (VSM). $DT_B$ in the range of 4 to 473K are then deduced from hysteresis loops measured at 4K by VSM after a specific procedure (Chapter 1.3).

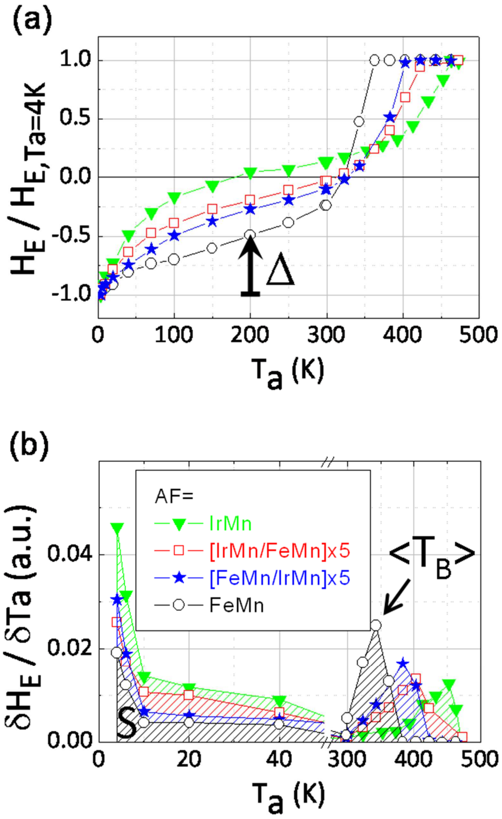

**Figure 4.1**

*(a) Typical variations with the annealing temperatures ($T_a$) of the normalized loop shift ($H_E$ / $|H_E$ (Ta = 4K)$|$) deduced from hysteresis loops measured at 4K by VSM along the field cooling direction for F/AF stacks with compositions: CoFeB (2 nm)/NiFe (1.5 nm)/AF, and subject to a procedure detailed within the text and involving various $T_a$. The AF layers are: IrMn (10 nm), [IrMn (1 nm)/FeMn (1 nm)]x5, [FeMn (1 nm)/IrMn (1 nm)]x5 and FeMn (10 nm). (b) Variations with $T_a$ of the normalized derivatives $\delta H_E/\delta T_a$. $\delta H_E/\delta T_a$ vs $T_a$ represent the blocking temperature distributions ($DT_B$).*

Figure 4.1 shows the variations with $T_a$ of the normalized loop shifts, $H_E$ / $|H_E$ ($T_a$ = 4K)$|$ and the corresponding derivatives for our F/AF multilayers with various AFs: IrMn (10 nm), [IrMn (1 nm)/FeMn (1 nm)]$_{x5}$, [FeMn (1 nm)/IrMn (1 nm)]$_{x5}$ and FeMn (10 nm). Given that, Δ [Figure 4.1 (a)] or S [Figure 4.1 (b)] measures the glassy character of the interface. In the following and to ease the interpretation, this glassy character is expressed in percentage: $\Delta^*$ equals Δ normalized to the total expected variations of $H_E$, i.e. 2 for normalized $H_E$: from -1 (when all the AF entities contributing to $H_E$ at 4K are initially oriented positively) to 1 (when all the entities are reoriented negatively after completion of the FC procedure). The second inflection point in the $H_E$ vs $T_a$ variations [Figure 4.1(a)] corresponds to the high-T contribution to $DT_B$ [Figure 4.1 (b)] and is related to the grains stability and sizes dispersion. This contribution is centred on $<T_B>$ [see Figure 4.1(b)].

For the various AFs, Figure 4.1(a) shows the amount of interfacial spin-glass, $\Delta^*$ deduced from Figure 4.1(a). The F/AF magnetic interfacial quality varies from a glassy interface with IrMn (~ 52%) to a twice less glassy interface with FeMn (~ 25%) via an intermediate value with [IrMn(t)/FeMn(t)]$_{xN}$ repetitions (~ 38%). The differences between IrMn ($Ir_{20}Mn_{80}$) and FeMn ($Fe_{50}Mn_{50}$) was already observed and ascribed to the larger proportion of Mn atoms for the IrMn [21,36]. It was inferred that the larger the amount of Mn atoms, the more glassy the interface. In particular, Mn atoms diffuse at the interface and create spin-glass phases. Lowering this via the addition of diffusion barriers was recently evidenced (Section 3.2). The intermediate value obtained with [IrMn(t)/FeMn(t)]$_{xN}$ repetitions are independent on the repetitions parameters (t;N). This implies that alloys partly form rather than well separated layers and well defined interfaces within the repetition. This is surely related to layers intermixing and alloying occurring during both deposition and post-deposition FC from 573K. Intermixing during the deposition process is in part ascribed to physical reasons (like impact-induced exchange events, which involve many parameters such as the kinetic incident energy of the adatoms, surface roughness and chemical bond energy of the underlying layer) and in part to chemical reasons (affinity between elements and tendency to form compounds). Post-deposition intermixing is due to the above same chemical reasons. Diffusion may occur via the core of each grain and via grain boundaries [107,109,111,112,115]. This may happen up to a threshold thickness larger than the diffusion lengths in the grains and grain boundaries (see paragraph 3.2.2). Actually, it is known that, in some conditions, grain boundaries and defects offer paths with enhanced atomic mobility, thereby possibly dominating the atomic transport. It is also known that some of these paths are open during deposition [112]. Although the science of layers interdiffusion at the atomic scale involves many complex aspects out of the scope of the present part, one of the major empirical conclusions here is that simply stacking (alloying) IrMn and FeMn offers a knob to tune the magnetic interface quality exactly between that of pure IrMn and FeMn.

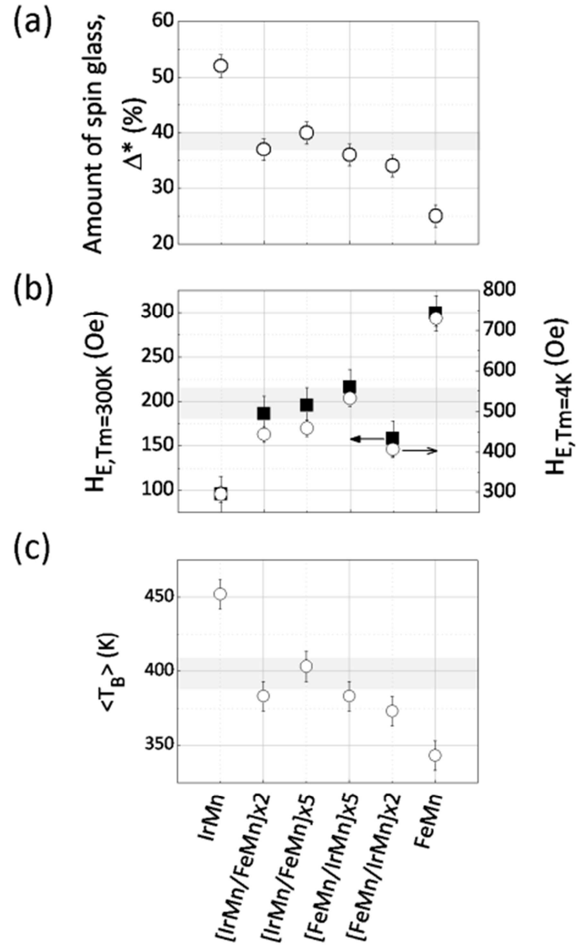

**Figure 4.2**

*For F/AF stacks with compositions: CoFeB (2 nm)/NiFe (1.5 nm)/AF, with AF = IrMn (10 nm), [IrMn (t nm)/FeMn (t nm)]$_{xN}$, [FeMn (t nm)/IrMn (t nm)]$_{xN}$ and FeMn (10 nm), for (t;N) = (2.5;2) and (1;5): (a) amount of spin-glass, $\Delta^*$ deduced from the blocking temperature distributions measurements: $\Delta^* = \Delta / 2$, with a typical $\Delta$ indicated in Figure 4.1(a); (b) amplitude of hysteresis loop shift, $H_E$ measured at $T_m$ = 4 and 300K and (c) mean blocking temperature, of the high-T contribution, $<T_B>$ extracted from the blocking temperature distribution measurements: a typical $<T_B>$ is indicated in Figure 4.2(b). For every plot, the grey area is, within error bars, the mean value calculated from the IrMn and FeMn experimental data.*

Figure 4.2 (b) shows the hysteresis loop shift amplitude, $H_E$ measured at $T_m$ = 4 and 300K for the various AFs. For a given $T_m$, $H_E$ is related to many parameters such as the magnetic anisotropies of the F and AF ($K_F$, $K_{AF}$), the F-AF interfacial exchange stiffness ($J_{F-AF}$), the F and AF magnetic moments ($m_F$, $m_{AF}$) and the amount of AF entities that remain pinned when cycling the F (Chapter 1.2.4). Although this latter parameter itself results as well from a complex compromise between $J_{F-AF}$, AF-AF exchange stiffness ($J_{AF-AF}$), grains volumes, amount of spin-glasses on top of each grain etc., the $DT_B$ plotted in Figure 4.1(b) directly measures the relative amount of AF entities remaining pinned at T = $T_a$ (see Chapter 1.3). Figure 4.2(b) also shows that the $[IrMn(t)/FeMn(t)]_{xN}$ samples all have similar values almost intermediate between those of IrMn and FeMn: $H_{E,FeMn} > H_{E,[IrMn/FeMn]} > H_{E,IrMn}$. This is partly due to $J_{F\text{-}AF}$: FeMn coupled to NiFe shows larger $J_{F\text{-}AF}$ than IrMn. Additionally, it looks consistent that $J_{NiFe\text{-}[IrMn/FeMn]}$ stands almost between $J_{NiFe\text{-}FeMn}$ and $J_{NiFe\text{-}IrMn}$ since as measured and discussed above the $[IrMn(t)/FeMn(t)]_{xN}$ magnetic interface quality is intermediate between FeMn and IrMn,. The differences between $H_{E,FeMn}$, $H_{E,[IrMn/FeMn]}$ and $H_{E,IrMn}$ is also in part related to the amount of stable AF entities which, is larger for FeMn compared to $[IrMn(t)/FeMn(t)]_{xN}$ and IrMn, e. g. see Figure 4.1(b) integrand from 573 to 300K.

Figure 4.2 (c) represents the mean $T_B$ of the high-T contribution, $<T_B>$ extracted from Figure 4.1(b) for the various AFs. The $[IrMn(t)/FeMn(t)]_{xN}$ repetitions all show almost similar values of $<T_B>$ which confirms the partly formation of alloys rather than well distinct layers separated by defined interfaces. Contrary to Figure 4.1(a) where only the magnetic interfacial quality is probed, $<T_B>$ is associated with the AF grains stability over F magnetization reversal and is related to both the coupling of the AF to the F ($J_{F\text{-}AF}$) and the intrinsic thermal stability of the AF grains ($K_{AF}V_{AF}$) (See Section1.2.4). It seems that alloying IrMn and FeMn also results in AF grains stabilities intermediate between IrMn and FeMn.

To conclude, the ferromagnetic/antiferromagnetic, F/AF storage layer building block of spintronics devices was studied for various mixed [IrMn/FeMn] AFs. In particular, this part used blocking temperature distributions to quantify the magnetic interfacial quality of the F/AF stack. Although alloying IrMn and FeMn improved the IrMn magnetic interfacial quality and concomitantly participated to $H_E$ enhancements, this adjustment was at the expense of the AF grains stability which lowered by shifting toward that of FeMn. Yet, interestingly laminating and partly alloying IrMn and FeMn offered an additional knob, easy to implement, to adjust both blocking temperature dispersions, hysteresis loop shift amplitudes and AF grains stability to values intermediate between those of IrMn and FeMn. This responds to an industrial need and in particular provides an ideal material for a TA-MRAM storage layer with better stability than FeMn at rest-T but requiring less write power consumption than IrMn.

## 4.2. Amount of spin-glasses over thin films and bit-cell dispersion in TA-MRAM devices [4]

For thermally-assisted magnetic random access memories (TA-MRAM), lowering bit-cells dispersions of exchange bias and of write power is necessary (see Paragraph 2.4). In this Chapter, we factually prove that spin-glass-like phases spread over the F/AF storage layer are the main cause of such distributions once the film is nanofabricated into a device. In particular, we show that the less the spin-glass like phases, the lower the bit-cell dispersion. More precisely, the amount of spin-glass-like phases was varied from sample to sample by sputtering various AFs: IrMn, FeMn and their alloys (see previous paragraph). Blocking temperature distributions were measured to quantify the amount of spin-glass-like phases at the wafer level. The wafers were then patterned by the CROCUS Technology team at the Tower Jazz foundry to obtain 1kb devices and the cells were tested electrically. Finally, the resulting loop shift cumulative distribution functions accounting for the bit-cell dispersions were correlated to the initial amount of spin-glass-like phases. This part will be reported in Ref. [4].

To develop MRAM, high TMR-ratio is not the single criterion to establish a fully-functional device. Among large variety of difficulties to overcome many of them relate to the writing procedure. Writing is complicated mainly because of two major reasons. First, there are current-related issues – like RA product [72], critical current control [146] and many others (see Section 2.3.1). Indeed, regardless the scheme of writing (whether it’s FIMS or CIMS) elevated currents and/or fields are required, that in turn may lead to barrier damages and selection transistor size increment [147]. The second critical point to be addressed is the homogeneity of the magnetic parameters shared between cells in the whole array. The issue with cell-to-cell parameters dispersion has been know from the very first generation of MRAM - TOGGLE-MRAM [148] and usually lead either to instability of written bits at rest-T, or either unselected bits writing or unwritten selected bits (due to insufficient field or current power for example) [149]. Many works were dedicated to point out the reasons of inhomogeneity and consequently the ways to avoid/reduce them. It was already shown, that inhomogeneity of geometrical shape [150,151] (due to etching for example), anisotropy (cell aspect ratio and shape, layers thickness) [152] and lateral edges defects [153–155] lead to high MTJ-cells variability. In the present work our attention was focused on another possible source or mechanism responsible for bit-cell dispersions – the F/AF interfacial glassy-character from the sheet film. To exclude as much as possible the above listed possible influence of geometry/edges/deposition-related parameters, all the sample preparation treatments were performed with the same systematic. We presume there are some geometry/edges/deposition variations among the junctions, but still due to sufficient statistics, we can consider the geometry/edges/deposition variations are the same for all the samples studied.

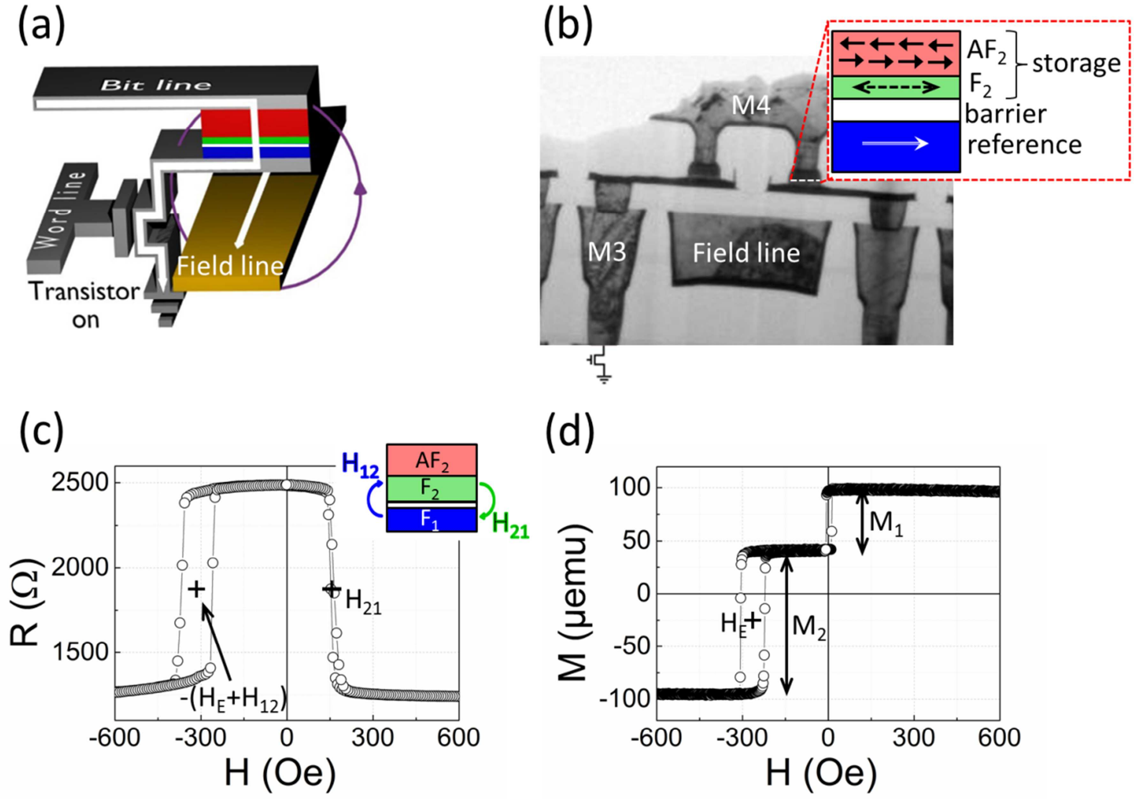

**Figure 4.3**

*(a) Sketch of a TA-MRAM cell during writing, i. e. when simultaneously heated and subjected to a magnetic field pulse thanks to electrical current flow through the tunnel barrier and the metallic field line, respectively. (b) Transmission electron microscopy (TEM) cross section for a typical 1 kb TA-MRAM device on CMOS under investigation here. The image shows two magnetic memory cells sandwiched between two metallic contacts: M3 and M4 (dark contrasts) and surrounded by an insulator (bright contrast). The inset details the magnetic stack. (c) Resistance (R) versus magnetic field (H) for a TA-MRAM cell with composition: substrate // buffer / [$AF_1$/Ru2/$F_1$] / MgO1.4 / [$F_2$/$AF_2$] / cap (nm), with $AF_1$ = PtMn20; $F_1$ = CoFeB1.2; $F_2$ = CoFeB2/NiFe1.5 and $AF_2$ = FeMn10. The measurement is done with an electrical prober at room-temperature. To ease data interpretation, the reference layer is downgraded to a simple free layer by decoupling $AF_1$ and $F_1$ with a thick Ru spacer. The EB loop shift ($H_E$) of the $F_2$/$AF_2$ storage layer and the stray fields created by $F_1$ on $F_2$ ($H_{12}$) and by $F_2$ on $F_1$ ($H_{21}$) are defined in the graph and inset. (d) Hysteresis loop for the corresponding sheet film measured by magnetometry at room temperature. The EB loop shift $H_E$ is also defined in the graph in addition to the magnetizations $M_1$ and $M_2$ of the $F_1$ and $F_2$ layers, respectively.and M4 (dark contrasts) and surrounded by an insulator (bright contrast). The inset details the magnetic stack.*

For this study, the following multilayers were fabricated: CMOS / buffer / [$AF_1$/Ru2/$F_1$] / MgO1.4 / [$F_2$/$AF_2$] / thermal barrier / cap (nm), with $AF_1$ = PtMn20; $F_1$ = CoFeB1.2; $F_2$ = CoFeB2/NiFe1.5 and $AF_2$ = IrMn10; $\{IrMn1/FeMn1\}_{x5}$, $\{FeMn1/IrMn1\}_{x5}$ and FeMn10. The total thickness of $AF_2$ is kept constant. Here, we specifically worked on the EB properties of the [$F_2$/$AF_2$] storage layer. Therefore, to ease data interpretation and in contrast to the TA-MRAM final product, the [$AF_1$/Ru2/$F_1$] reference layer is downgraded to a simple free layer by decoupling $AF_1$ and $F_1$ with a thick Ru spacer. For similar reasons we used F layers instead of synthetic-AFs stacks. The multilayer structures were deposited by dc-magnetron sputtering with an Ar pressure of $2.5 \times 10^{-3}$ mbar onto 8-inch standard complementary metal oxide semiconductor (CMOS) wafers with typical pre-processed back-end transistors. In the multilayer structures, PtMn, NiFe, CoFeB, IrMn and FeMn were made from $Pt_{38}Mn_{62}$, $Ni_{81}Fe_{19}$, $Co_{60}Fe_{20}B_{20}$, $Ir_{20}Mn_{80}$ and $Fe_{50}Mn_{50}$ targets (at. %), respectively. For studies of EB, room temperature EB was set by post-deposition field cooling (FC) of the samples for 90 min in a resistive furnace from an initial temperature $T_{init}$ down to room temperature, with $T_{init}$ = 300°C. The vacuum level during annealing is set to $10^{-6}$ mbar. Positive magnetic field during cooling is applied in the sample plane, with an amplitude of 2.5 kOe, large enough to saturate the F layers. Following this initial FC, all the AF entities with a blocking temperature ($T_B$) larger than room temperature were oriented toward the positive direction. Room temperature hysteresis loops were then measured along the FC direction by vibrating sample magnetometry (VSM). Blocking temperature distributions were then measured by use of standard FC from incremental annealing temperatures down to 4K and hysteresis loop measurements at 4K. Details of the measurement of blocking temperature distributions and extraction of the relative amount of spin-glass like phases spread over the sheet wafer ($\Delta^*$) was described at the end of Chapter 1. Here, for the four multilayer composition, we obtained: $\Delta^*$ = 52; 40; 36; and 27 % corresponding to $AF_2$ = IrMn10; $\{IrMn1/FeMn1\}_{x5}$, $\{FeMn1/IrMn1\}_{x5}$ and FeMn10 (nm), respectively. Note that in our earlier work (see 4.1), for similar stacks we had obtained very similar values. It gives an idea of the sample to sample reproducibility for both the fabrication and measurement. Following this step, the wafers were processed to obtain two series of 1 kb TA-MRAM devices on CMOS with circular magnetic cells of diameter 140 and 200 nm. The process involved standard steps and was performed on the production line of the CROCUS Technology company, at Tower Jazz.

Figure 4.3(a) sketches a typical TA-MRAM cell on CMOS during writing, i.e. when simultaneously heated and subjected to a magnetic field pulse. Heating above the blocking temperature of the [$F_2$/$AF_2$] storage layer is achieved thanks to an electrical current flowing from the bit-line to the word-line and hence across the tunnel barrier. The magnetic pulse is created by an electrical current in the field line. Figure 4.3(b) shows a transmission electron microscopy (TEM) cross section for our typical 1 kb TA-MRAM device on CMOS. The image shows two magnetic memory cells sandwiched between two metallic contacts: M3 and M4 (dark contrasts) and surrounded by an insulator (bright contrast). The metallic contacts connect the magnetic stack – detailed in the inset - to the bit-line and word-lines. The field line is also clearly visible in the TEM image. Following the process, the electrical properties of every memory cell of the 1k devices were tested at room temperature by use of an automated electrical prober. The measurement consisted in recording resistance vs magnetic field (R vs H) loops. For such a measurement, a bias voltage of 50 mV was applied between the bit- and word-lines to read R. For reading, contrary to the writing, the current was sufficiently small to avoid heating above the blocking temperature of the [$F_2$/$AF_2$] storage layer. In addition, the field line current was used here to sweep the magnetic field between +/- 800 Oe. Here typical currents resulting from the 50 mV bias were of tens of µA for resistances of the order of k$\Omega$. As a result of the electrical measurements, for each of the four multilayer compositions we obtained two sets of thousand resistance vs magnetic field (R vs H) loops: one for the 140 nm cells and one for the 200 nm cell. A R vs H loop for a TA-MRAM cell is shown in Figure 4.3(c). The EB loop shift ($H_E$) of the $F_2$/$AF_2$ storage layer and the stray fields created by $F_1$ on $F_2$ ($H_{12}$) and by $F_2$ on $F_1$ ($H_{21}$) are defined in the graph and inset. The hysteresis loop for the corresponding sheet film was measured by VSM at room temperature and is shown in Figure 4.3(d). The EB loop shift $H_E$ is also defined in the graph in addition to the magnetizations $M_1$ and $M_2$ of the $F_1$ and $F_2$ layers, respectively. From Figure 4.3(d), we determine experimentally ($M_1$ / $M_2$): ($M_1$ / $M_2$) = 0.42. We recall that $F_1$ = CoFeB(1.2 nm) and $F_2$ = CoFeB(2 nm) / NiFe (1.5 nm). Given that, the nominal value of ($M_1$ / $M_2$) writes: ($M_1$ / $M_2$) = (1.2 x $M_{S,CoFeB}$) / (2 x $M_{S,CoFeB}$ + 1.5 x $M_{S,NiFe}$) where $M_{S,i}$ are the saturation magnetization of the layers. Separate measurements of the CoFeB and NiFe layers with a superconducing interference quantum device gave us: $M_{S,CoFeB}$ ~ 1100 emu.cm$^{-3}$ and $M_{S,NiFe}$ ~ 750 emu.cm$^{-3}$. The nominal value of ($M_1$ / $M_2$) thus equals 0.4. There is a closer fit between the nominal and experimental values. It is reasonable to assume that the $F_1$ and $F_2$ layers are conformal in shape. From simple considerations, it thus results that the ratio between $H_{12}$ and $H_{21}$ is equal to that of $M_1$ and $M_2$. It results that $H_{12}$ = 0.42 x $H_{21}$. For every memory cell, it was thus possible to extract the EB loop shift: $H_{E12}$ = ($H_E$ + $H_{12}$) and $H_{21}$ were extracted from the R vs H loop [see Fig. 1(c)] and $H_E$ was calculated from: $H_E$ = $H_{E12}$ - (0.42 x $H_{21}$). For the example shown in Fig. 1(c) for a 200 nm TA-MRAM cell, we find $H_E$ ~ 330 Oe. For the corresponding sheet film, we get a close fit: $H_E$ ~ 315 Oe, as measured from the hysteresis loop plotted in Figure 4.3(d). In this case, we found that finite size had a negligible impact on the mean EB loop shift.

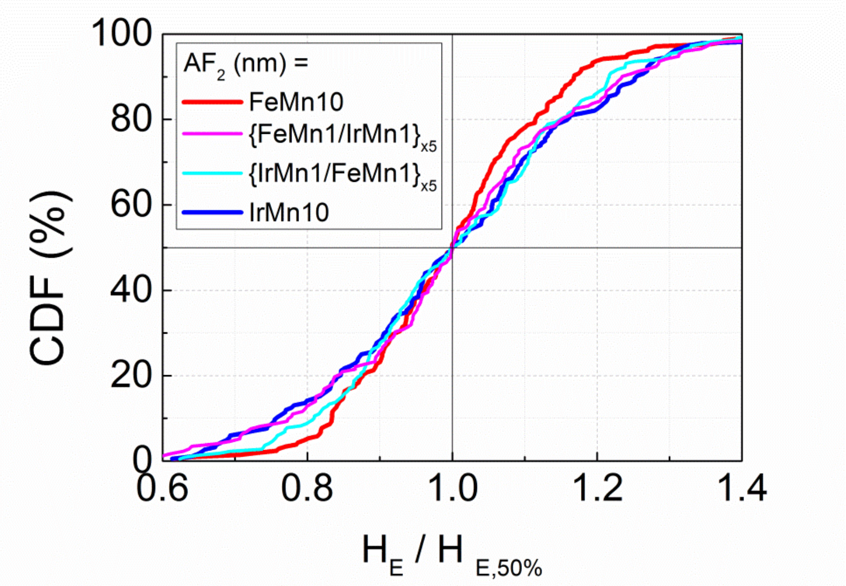

**Figure 4.4**

*For four 1kb TA-MRAM devices, cumulative distribution function of hysteresis loop shift over the TA-MRAM cells as a function of the normalized hysteresis loop shift ($H_E/H_{E,50\%}$). The composition of the TA-MRAM cells are: substrate // buffer / [$AF_1$/Ru2/$F_1$] / MgO1.4 / [$F_2$/$AF_2$] / cap (nm), with $AF_1$ = PtMn20; $F_1$ = CoFeB1.2; and $F_2$ = CoFeB2/NiFe1.5. The antiferromagnet in the storage layer is varied between the four devices: $AF_2$ = IrMn10; $\{IrMn1/FeMn1\}_{x5}$, $\{FeMn1/IrMn1\}_{x5}$ and FeMn10. The bit-cell diameter is 140 nm.*

Next, for statistical analysis of the random bit-cell distribution of $H_E$ over the TA-MRAM devices, we used the concept of cumulative distribution function. We performed cumulative frequency analysis. It is the analysis of the frequency of occurrence of $H_E$. For four 1kb TA-MRAM devices with four different $AF_2$ layers, Figure 4.4 shows the cumulative distribution for $H_E$ versus $H_E$ normalized to $H_{E,50\%}$, where $H_{E,50\%}$ is the value of $H_E$ with an occurrence of 50%. The graph reads as follows: when the cumulative distribution equals, for example, 30%, the corresponding value of $H_E/H_{E,50\%}$ is 0.9 for $AF_2$ = IrMn10. It means that the frequency of occurrence of $H_E/H_{E,50\%}$ less than 0.9 is 30%. In Fig. 3, the width of the cumulative distribution of $H_E$ accounts for the bit-cell dispersion of $H_E$. Somehow, the central slope of the curves is a good preliminary indication of the trend as a function of the $AF_2$ layer composition. The bit-cell dispersion of $H_E$ seems to be larger when changing the $AF_2$-layer from pure FeMn to pure IrMn. In order to quantitatively analyze such bit-cell dispersion, we calculated the standard deviation ($\sigma_{HE}$) for the distribution.

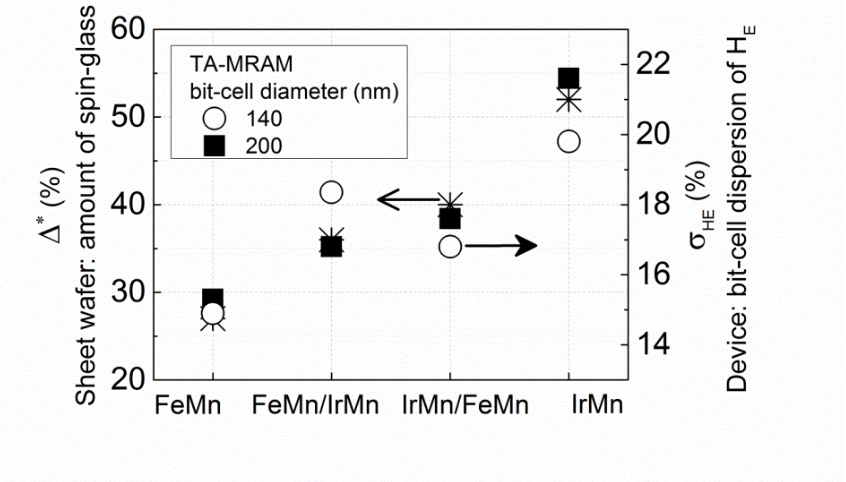

**Figure 4.5**

*For four compositions: substrate // buffer / [$AF_1$/Ru2/$F_1$] / MgO1.4 / [$F_2$/$AF_2$] / cap (nm), with $AF_1$ = PtMn20; $F_1$ = CoFeB1.2; $F_2$ = CoFeB2/NiFe1.5 and $AF_2$ = IrMn10; $\{IrMn1/FeMn1\}_{x5}$, $\{FeMn1/IrMn1\}_{x5}$ and FeMn10: amount of spin-glass like phases ($\Delta^*$) deduced from blocking temperature distributions measurements on the sheet wafers and root mean square deviation ($\sigma_{HE}$) of the cumulative distribution function of hysteresis loop shift ($H_E$) over the TA-MRAM cells of 1kb devices, i. e. after processing. $\sigma_{HE}$ accounts for the bit-cell dispersions of $H_E$.*

For the four $AF_2$ layer composition Figure 4.5 shows the amount of spin-glass like phases ($\Delta^*$) deduced from blocking temperature distributions measurements on the sheet wafers and the standard deviation ($\sigma_{HE}$) over the TA-MRAM cells of the 1kb devices, i. e. after processing, calculated from Fig. 3. We recall that $\sigma_{HE}$ accounts for the bit-cell dispersions of $H_E$. The cells diameter was 200 nm. The graph also recalls that the amount of spin-glass like phases was varied by tuning the $AF_2$ layer composition and in particular its amount of Mn. From earlier works, we evidenced that the larger the amount of Mn, the larger the amount of spin-glass like phases over the sheet film (see 4.1). We used this earlier advance as a mean to tune the amount of spin-glass like phases here. From Figure 4.5, the dependence of the bit-cell dispersions of $H_E$ after patterning, $\sigma_{HE}$, with the $AF_2$-layer composition follows that of the amount of spin-glass like phases measured at the sheet film level; strictly speaking, except for $AF_2$ = [FeMn/IrMn] with 140 nm cells. The origin of this discrepancy is under further consideration and it may well give an idea of the error bars on $\sigma_{HE}$. The correlation between amount of spin-glass like phases measured at the sheet film level and bit-cell dispersions of $H_E$ in TA-MRAM processed devices is better visible in Figure 4.6. This latter shows $\sigma_{HE}$ versus $\Delta^*$ for two sets of 1kb TA-MRAM devices: with bit-cells diameters of 140 and 200 nm. Note that the bit-cell dispersion of $H_E$ is on average slightly smaller for the smaller bit-cell diameter.

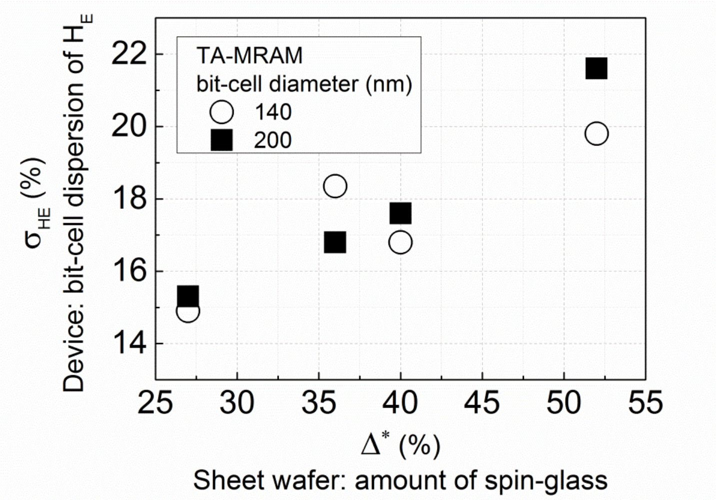

**Figure 4.6**

*Bit-cell dispersions of $H_E$ ($\sigma_{HE}$) for 1kb TA-MRAM devices with bit-cells diameters of 140 and 200 nm respectively, plotted as a function of the amount of spin-glass like phases ($\Delta^*$) spread over the sheet wafers.*

To conclude this paragraph, it was supposed few years ago [93] that randomly spread spin-glass like phases at the F/AF interface or within the bulk of the AF layer significantly contributes to the distributions of EB properties in devices after processing. As detailed earlier, these regions result from frustrations of exchange interactions due for example to interfacial roughness, structural defects, peculiar AF spin structure, interdiffusion of species, and grain boundaries in the case of polycrystalline films. The following hypothesis was made: by nature, these frustrations are randomly spread over the wafer and thus over the memory cells after nanofabrication as sketched in Figure 2.12. As opposed to cells with few spin-glass like regions, cells with more of such regions show a weaker hysteresis loop shift at room-T and are more prone to thermal activation since the F/AF interfacial coupling is disrupted on a large part of the cell area. Ultimately, these cells lose their spin reference direction and correlatively fail. Here, we factually proved the link between spin-glasses spread over ferromagnetic/antiferromagnetic thin films and bit-cell dispersions of exchange bias in corresponding TA-MRAM. Note also that in addition to bridging the gap between fundamental spin-glass like phases and a technological application, we also demonstrate here that blocking temperature distributions are a versatile method to qualify TA-MRAM production batches before processing. In fact, from blocking temperature distributions measured with a piece of sheet film, one measures the amount of spin-glass like phases spread over the film and one can select whether the wafer is worth processing or not.

# CONCLUSION AND PERSPECTIVES

The present work was mainly driven by the improvement of spintronics devices and more specifically of TA-MRAMs. Such devices use one ferromagnetic/antiferromagnetic (F/AF) reference layer to set the reference direction of the spins of the conduction electrons and one F/AF storage layer to encode every memory-cell. We focused our attention on the storage layer. Exchange bias (EB) and the distributions of EB properties from bit-cell to bit-cell were the main points investigated. Exchange bias depends on numerous factors, among which is the interfacial quality between the F and AF layers. It was earlier speculated that this interfacial quality in the sheet film and in particular the F/AF glassy character may lead to variability from one bit to another once the sheet wafer is patterned into a device. Such bit-cells dispersions are crucial for applications and need to be reduced as much as possible. In the present thesis the attention was paid on the origins of such interfacial quality; on various ways to tune the F/AF glassy character and finally on the factual comparison between the amount of interfacial spin-glass like phases in the sheet film and the bit-cells dispersions in the corresponding device. Throughout, the interfacial quality was quantitatively investigated by use of a recent technique: measurements of the low-temperature contributions to the blocking temperature distributions: the smaller the contribution, the less glassy the interface [21,93].

Widely used for industrial applications, the magnetron sputtering deposition process itself and the further thermal treatments used to functionalize the stacks result in atomic interdiffusion. It has been shown that such interdiffusion is one of the mechanisms responsible for the formation of spin-glass like phases. In particular, mainly Mn-based alloys are used as AF in spintronics devices and Mn-diffusion was identified as key to the formation of spin-glass like phases. Here, the role of Mn-diffusion was consolidated. Mn-diffusion was directly observed, understood and the use of complex barriers to reduce such diffusion and consequently to minimize the amount of spin-glass was successfully studied. In particular, Cu and Pt based barriers were inserted at Co/IrMn. The use of (Cu/Pt) intermixing dual barriers led to blocking temperature distributions reductions as a result of interfaces improvements. All at once, (Cu/Pt) limited Co-Mn, Co-Pt and Cu-Mn mixing, which took place when using either no or single Pt and Cu barriers. This study can be pursued by search for more suitable barriers: i.e. less prone to diffusion through grain boundaries; softer from the process point of view to ease the etching process; less expensive materials; and thinner barriers to maintain a sufficient F/AF coupling. The use of PtMn alloys as a barrier may be a possible solution to tackle the above mentioned points since PtMn has a low formation enthalpy and shall therefore be very stable against Mn-diffusion.

The choice of AF materials in a TA-MRAM storage layer is limited due to parameters that are determined by the device working principle. The blocking temperature is one of these parameters and it determines the standby thermal stability of the bi-cell and the writing power consumption. Engineering the storage layer requires compromises since its critical temperature needs to be adjusted above the rest-T but below the write-T. AFs used in TA-MRAM are mostly based on IrMn or FeMn for the storage one. One of the present industrial issues with regards to TA-MRAM was to find a storage layer with intermediate properties between those of IrMn and FeMn and in particular with a blocking-T larger than FeMn for better stability at rest-T but lower than IrMn to reduce power consumption at write-T. Since the F/AF blocking-T tends toward the intrinsic Néel-T of the AF in the nanosecond range, the intrinsic properties needed to be tuned and not simply extrinsic properties such as the layer thickness. By laminating and partly alloying IrMn and FeMn we proposed an additional knob, easy to implement, to adjust both blocking temperature dispersions, hysteresis loop shift amplitudes and AF grains stability to values intermediate between those of IrMn and FeMn. We insist on the fact that, interestingly, such composite AF were also a way to tune the amount of spin-glass like phases. Supplementary studies may include deposition of thicker AF in contact with the F-layer, and further variation of deposition order of the rest AF. It can be interesting because of two reasons – in shown study we dealt with very thin repetition thickness of only 1nm, which may be not sufficient to limit diffusion from upcoming repetitions; and secondly, to check how the alloying is reflected on net properties of complex AF. In addition: - partly forming an IrFeMn alloy via IrMn/FeMn lamination provides an intermediate intrinsic bulk $T_N$ which contributes to intermediate $<T_B>$ once coupled to a F; - given that on the contrary FeMn/F are better than IrMn/F and IrFeMn/F interfaces to augment $H_E$ and reduce interfacial spin glasses; - then the ideal solution is probably to make an IrFeMn-thick/FeMn-thin/F sample. However, we have seen that Mn likely diffuses from IrMn to FeMn and diminishes the potential of IrMn/FeMn lamination. Adding a Mn diffusion barrier here could be appropriate in order to recover laminated structures rather than IrFeMn alloys throughout to the interface. [FeMn/IrMn]/Pt ($t_{Pt}$)/FeMn ($t_{FeMn}$)/F and [FeMn/IrMn]/PtMn ($t_{Pt}$)/FeMn ($t_{FeMn}$)/F stacks started to be tested in the frame of the M2 and then as part of the PhD thesis of Lamprini Frangou (2014-2017).

We have seen that tuning the amount of Mn-diffusion and hence the amount of spin-glass like phases in Mn-based F/AF bilayers can be achieved by use of diffusion barriers and of composite AF. Preliminary attempts to tune the amount of Mn-diffusion via ion irradiations were also investigated in the frame of the present PhD thesis in collaboration with the Laboratoire de Physique des Solides, Orsay and the Helmholtz-Zentrum Dresden-Rossendorf. These preliminary data are shown in Appendix 2.

Finally, we factually proved that spin-glass-like phases spread over the F/AF storage layer are the main cause of bit-cells distributions once the film is nanofabricated into 1kb TA-MRAM devices. This is one of the key results of the present PhD thesis since it is somehow a “proof of concept” and it bridges the gap between some fundamental physics and a technological application. In addition, it was evidenced, that quantifying the interfacial quality of the continuous film predicts the degree of homogeneity for the corresponding patterned devices. Given that, blocking temperature distributions are a versatile method to qualify TA-MRAM production batches before processing. The direct inspection of the bit-cell dispersion of write power is presently under investigation, since it was also pointed out that the amount of spin-glass like phases may correlate to the bit-cell dispersion of blocking temperature and hence of write power. Further analysis may also involve more functional structures, such as composite AFs and stacks with Mn-diffusion barrier.

To complement earlier studies of finite size effects on the formation of F/AF spin-glasses along the dot edges, a special focus will be given on the influence of the dots lateral oxidation for the formation of spin-glasses. Potentially overcoming this issue via encapsulation was envisaged and preliminary tackled in the frame of the present PhD thesis. Finally, a recent collaboration started with the University of Berkeley in an attempt to directly compare existing X-ray dichroism data and blocking temperature measurements in order to factually evaluate the complementarities of the two techniques with regards to the quantification of spin-glasses. A preliminary attempt is shown in Appendix 3.

# Bibliographical references

[1] F. Letellier, L. Lechevallier, R. Lardé, J.-M. Le Breton, K. Akmaldinov, S. Auffret, B. Dieny, V. Baltz, Direct imaging of thermally-activated grain-boundary diffusion in Cu/Co/IrMn/Pt exchange-bias structures using atom-probe tomography, J. Appl. Phys. 116 (2014). doi:10.1063/1.4902954.

[2] K. Akmaldinov, S. Auffret, I. Joumard, B. Dieny, V. Baltz, Benefit of inserting a (Cu/Pt) intermixing dual barrier for the blocking temperature distribution of exchange biased Co/(Cu/Pt)/IrMn stacks, Appl. Phys. Lett. 103 (2013) 042415. doi:10.1063/1.4816816.

[3] K. Akmaldinov, C. Ducruet, C. Portemont, I. Joumard, I.L. Prejbeanu, B. Dieny, V. Baltz, Mixing antiferromagnets to tune NiFe-[IrMn/FeMn] interfacial spin-glasses, grains thermal stability, and related exchange bias properties, J. Appl. Phys. 115 (2014) 17B718. doi:10.1063/1.4864144.

[4] K. Akmaldinov, L. Frangou, C. Ducruet, J. Alvarez-Hérault, V. Baltz, Bridging amount of spin-glasses over ferromagnetic/antiferromagnetic thin films and bit-cell dispersion of exchange bias in corresponding TA-MRAM devices', To Be Submitt. (n.d.).

[5] W.H. Meiklejohn, C. Bean, New Magnetic Anisotropy, Phys. Rev. 102 (1956) 1413–1414. doi:10.1103/PhysRev.102.1413.

[6] H. Ohldag, Erlangung des Doktorgrades, Universität Düsseldorf, 2003.

[7] W.H. Meiklejohn, C. Bean, New Magnetic Anisotropy, Phys. Rev. 105 (1957) 904–913. doi:10.1103/PhysRev.105.904.

[8] W.H. Meiklejohn, Exchange Anisotropy—A Review, J. Appl. Phys. 33 (1962) 1328. doi:10.1063/1.1728716.

[9] M. Tsunoda, Y. Tsuchiya, M. Konoto, M. Takahashi, Microstructure of antiferromagnetic layer affecting on magnetic exchange coupling in trilayered Ni-Fe/25 at% Ni-Mn/Ni-Fe films, J. Magn. Magn. Mater. 171 (1997) 29–44. doi:10.1016/S0304-8853(97)00054-1.

[10] R. Jungblut, R. Coehoorn, M.T. Johnson, J. aan de Stegge, A. Reinders, Orientational dependence of the exchange biasing in molecular-beam-epitaxy-grown Ni80Fe20/Fe50Mn50 bilayers (invited), J. Appl. Phys. 75 (1994) 6659. doi:10.1063/1.356888.

[11] J. Nogués, J. Sort, V. Langlais, V. Skumryev, S. Suriñach, J.S. Muñoz, et al., Exchange bias in nanostructures, Phys. Rep. 422 (2005) 65–117. doi:10.1016/j.physrep.2005.08.004.

[12] J.S. Kouvel, Exchange Anisotropy in an Iron-Aluminum Alloy, J. Appl. Phys. 30 (1959) S313. doi:10.1063/1.2185950.

[13] D. Mauri, H.C. Siegmann, P.S. Bagus, E. Kay, Simple model for thin ferromagnetic films exchange coupled to an antiferromagnetic substrate, J. Appl. Phys. 62 (1987) 3047. doi:10.1063/1.339367.

[14] A. Malozemoff, Random-field model of exchange anisotropy at rough ferromagnetic-antiferromagnetic interfaces, Phys. Rev. B. 35 (1987) 3679–3682. doi:10.1103/PhysRevB.35.3679.

[15] V. Baltz, Effets de taille finie sur les couplages magnétostatiques et l'anisotropie d'échange dans le domaine de l'enregistrement magnétique, PhD Thesis, 2005.

[16] U. Nowak, K. Usadel, J. Keller, P. Miltényi, B. Beschoten, G. Güntherodt, Domain state model for exchange bias. I. Theory, Phys. Rev. B. 66 (2002) 014430. doi:10.1103/PhysRevB.66.014430.

[17] K. Takano, R.H. Kodama, A. Berkowitz, W. Cao, G. Thomas, Role of interfacial uncompensated antiferromagnetic spins in unidirectional anisotropy in Ni[sub 81]Fe[sub 19]/CoO bilayers (invited), J. Appl. Phys. 83 (1998) 6888. doi:10.1063/1.367721.

[18] K. Takano, R.H. Kodama, A. Berkowitz, W. Cao, G. Thomas, Interfacial Uncompensated Antiferromagnetic Spins: Role in Unidirectional Anisotropy in Polycrystalline Ni81Fe19/CoO Bilayers, Phys. Rev. Lett. 79 (1997) 1130–1133. doi:10.1103/PhysRevLett.79.1130.

[19] E. Fulcomer, Thermal fluctuation aftereffect model for some systems with ferromagnetic-antiferromagnetic coupling, J. Appl. Phys. 43 (1972) 4190. doi:10.1063/1.1660894.

[20] A. Berkowitz, K. Takano, Exchange anisotropy — a review, J. Magn. Magn. Mater. 200 (1999) 552–570. doi:10.1016/S0304-8853(99)00453-9.

[21] V. Baltz, B. Rodmacq, A. Zarefy, L. Lechevallier, B. Dieny, Bimodal distribution of blocking temperature in exchange-biased ferromagnetic/antiferromagnetic bilayers, Phys. Rev. B. 81 (2010) 052404. doi:10.1103/PhysRevB.81.052404.

[22] K. O'Grady, L.E. Fernandez-Outon, G. Vallejo-Fernandez, A new paradigm for exchange bias in polycrystalline thin films, J. Magn. Magn. Mater. 322 (2010) 883–899. doi:10.1016/j.jmmm.2009.12.011.

[23] E. Fulcomer, Temperature and frequency dependence of exchange anisotropy effects in oxidized NiFe films, J. Appl. Phys. 43 (1972) 4184. doi:10.1063/1.1660893.

[24] E.C. Stoner, E.P. Wohlfarth, A Mechanism of Magnetic Hysteresis in Heterogeneous Alloys, Philos. Trans. R. Soc. A Math. Phys. Eng. Sci. 240 (1948) 599–642. doi:10.1098/rsta.1948.0007.

[25] J. Nogués, I.K. Schuller, Exchange bias, J. Magn. Magn. Mater. 192 (1999) 203–232. doi:10.1016/S0304-8853(98)00266-2.

[26] M. Stiles, R.D. McMichael, Model for exchange bias in polycrystalline ferromagnet-antiferromagnet bilayers, Phys. Rev. B. 59 (1999) 3722–3733. doi:10.1103/PhysRevB.59.3722.

[27] M. Ali, P. Adie, C.H. Marrows, D. Greig, B.J. Hickey, R. Stamps, Exchange bias using a spin glass., Nat. Mater. 6 (2007) 70–5. doi:10.1038/nmat1809.

[28] I. Tomeno, H.N. Fuke, H. Iwasaki, M. Sahashi, Y. Tsunoda, Magnetic neutron scattering study of ordered Mn[sub 3]Ir, J. Appl. Phys. 86 (1999) 3853. doi:10.1063/1.371298.

[29] F. Ernult, B. Dieny, L. Billard, F. Lançon, J.R. Regnard, Increase in ferromagnetic/antiferromagnetic exchange bias due to a reduction of the interfacial exchange interaction, J. Appl. Phys. 94 (2003) 6678. doi:10.1063/1.1614867.

[30] J. Geshev, T. Dias, S. Nicolodi, R. Cichelero, A. Harres, J.J.S. Acuña, et al., Role of the uncompensated interface spins in polycrystalline exchange-biased systems, J. Phys. D. Appl. Phys. 44 (2011) 095002. doi:10.1088/0022-3727/44/9/095002.

[31] A. Tan, J. Li, C.A. Jenkins, E. Arenholz, A. Scholl, C. Hwang, et al., Exchange bias in epitaxially grown CoO/MgO/Fe/Ag(001), Phys. Rev. B. 86 (2012) 064406. doi:10.1103/PhysRevB.86.064406.

[32] S. Soeya, T. Imagawa, K. Mitsuoka, S. Narishige, Distribution of blocking temperature in bilayered Ni81Fe19/NiO films, J. Appl. Phys. 76 (1994) 5356. doi:10.1063/1.358488.

[33] M. Ali, C. Marrows, M. Al-Jawad, B. Hickey, A. Misra, U. Nowak, et al., Antiferromagnetic layer thickness dependence of the IrMn/Co exchange-bias system, Phys. Rev. B. 68 (2003) 214420. doi:10.1103/PhysRevB.68.214420.

[34] V. Baltz, J. Sort, B. Rodmacq, B. Dieny, S. Landis, Thermal activation effects on the exchange bias in ferromagnetic-antiferromagnetic nanostructures, Phys. Rev. B. 72 (2005) 104419. doi:10.1103/PhysRevB.72.104419.

[35] L. Lechevallier, A. Zarefy, R. Lardé, H. Chiron, J.-M. Le Breton, V. Baltz, et al., Structural analysis and magnetic properties of (Pt/Co)3/PttPt/IrMn multilayers, Phys. Rev. B. 79 (2009) 174434. doi:10.1103/PhysRevB.79.174434.

[36] V. Baltz, Thermally driven asymmetric responses of grains versus spin-glass related distributions of blocking temperature in exchange biased Co/IrMn bilayers, Appl. Phys. Lett. 102 (2013) 062410. doi:10.1063/1.4792347.

[37] C.K. Safeer, M. Chamfrault, J. Allibe, C. Carretero, C. Deranlot, E. Jacquet, et al., Anisotropic bimodal distribution of blocking temperature with multiferroic BiFeO3 epitaxial thin films, Appl. Phys. Lett. 100 (2012) 072402. doi:10.1063/1.3684812.

[38] V. Baltz, G. Gaudin, P. Somani, B. Dieny, Influence of edges on the exchange bias properties of ferromagnetic/antiferromagnetic nanodots, Appl. Phys. Lett. 96 (2010) 262505. doi:10.1063/1.3449123.

[39] G. Binasch, P. Grünberg, F. Saurenbach, W. Zinn, Enhanced magnetoresistance in layered magnetic structures with antiferromagnetic interlayer exchange, Phys. Rev. B. 39 (1989) 4828–4830. doi:10.1103/PhysRevB.39.4828.

[40] M.N. Baibich, J.M. Broto, A. Fert, F.N. Van Dau, F. Petroff, Giant Magnetoresistance of (001)Fe/(001)Cr Magnetic Superlattices, Phys. Rev. Lett. 61 (1988) 2472–2475. doi:10.1103/PhysRevLett.61.2472.

[41] S.M. Thompson, The discovery, development and future of GMR: The Nobel Prize 2007, J. Phys. D. Appl. Phys. 41 (2008) 093001. doi:10.1088/0022-3727/41/9/093001.

[42] R. Meservey, P.M. Tedrow, Spin polarization of tunneling electrons from films of Fe, Co, Ni, and Gd, Solid State Commun. 11 (1972) 333–336. doi:10.1016/0038-1098(72)90244-X.

[43] M. Julliere, Tunneling between ferromagnetic films, Phys. Lett. A. 54 (1975) 225–226. doi:10.1016/0375-9601(75)90174-7.

[44] J.C. Slonczewski, Conductance and exchange coupling of two ferromagnets separated by a tunneling barrier, Phys. Rev. B. 39 (1989) 6995–7002. doi:10.1103/PhysRevB.39.6995.

[45] J.S. Moodera, L.R. Kinder, T.M. Wong, R. Meservey, Large Magnetoresistance at Room Temperature in Ferromagnetic Thin Film Tunnel Junctions, Phys. Rev. Lett. 74 (1995) 3273–3276. doi:10.1103/PhysRevLett.74.3273.

[46] I. Žutić, S. Das Sarma, Spintronics: Fundamentals and applications, Rev. Mod. Phys. 76 (2004) 323–410. doi:10.1103/RevModPhys.76.323.

[47] T. Miyazaki, N. Tezuka, Giant magnetic tunneling effect in Fe/Al2O3/Fe junction, J. Magn. Magn. Mater. 139 (1995) L231–L234. doi:10.1016/0304-8853(95)90001-2.

[48] W. Butler, X.-G. Zhang, T. Schulthess, J. MacLaren, Spin-dependent tunneling conductance of Fe|MgO|Fe sandwiches, Phys. Rev. B. 63 (2001) 054416. doi:10.1103/PhysRevB.63.054416.

[49] J. Mathon, A. Umerski, Theory of tunneling magnetoresistance of an epitaxial Fe/MgO/Fe(001) junction, Phys. Rev. B. 63 (2001) 220403. doi:10.1103/PhysRevB.63.220403.

[50] B. Dieny, R. Sousa, J. Hérault, C. Papusoi, G. Prenat, U. Ebels, et al., Spin-transfer effect and its use in spintronic components, Int. J. Nanotechnol. 7 (2010) 591–614.

[51] S. Yuasa, D.D. Djayaprawira, Giant tunnel magnetoresistance in magnetic tunnel junctions with a crystalline MgO(0 0 1) barrier, J. Phys. D. Appl. Phys. 40 (2007) R337–R354. doi:10.1088/0022-3727/40/21/R01.

[52] J.S. Moodera, G. Mathon, Spin polarized tunneling in ferromagnetic junctions, J. Magn. Magn. Mater. 200 (1999) 248–273. doi:10.1016/S0304-8853(99)00515-6.

[53] S. Parkin, K.P. Roche, M.G. Samant, P.M. Rice, R.B. Beyers, R.E. Scheuerlein, et al., Exchange-biased magnetic tunnel junctions and application to nonvolatile magnetic random access memory (invited), J. Appl. Phys. 85 (1999) 5828. doi:10.1063/1.369932.

[54] R. Sousa, J.J. Sun, V. Soares, P.P. Freitas, A. Kling, M.F. da Silva, et al., Large tunneling magnetoresistance enhancement by thermal anneal, Appl. Phys. Lett. 73 (1998) 3288. doi:10.1063/1.122747.

[55] S. Cardoso, V. Gehanno, R. Ferreira, P.P. Freitas, Ion beam deposition and oxidation of spin-dependent tunnel junctions, IEEE Trans. Magn. 35 (1999) 2952–2954. doi:10.1109/20.801044.

[56] S. Yuasa, A. Fukushima, H. Kubota, Y. Suzuki, K. Ando, Giant tunneling magnetoresistance up to 410% at room temperature in fully epitaxial Co∕MgO∕Co magnetic tunnel junctions with bcc Co(001) electrodes, Appl. Phys. Lett. 89 (2006) 042505. doi:10.1063/1.2236268.

[57] Y.M. Lee, J. Hayakawa, S. Ikeda, F. Matsukura, H. Ohno, Effect of electrode composition on the tunnel magnetoresistance of pseudo-spin-valve magnetic tunnel junction with a MgO tunnel barrier, Appl. Phys. Lett. 90 (2007) 212507. doi:10.1063/1.2742576.

[58] B. Dieny, V. Speriosu, S. Parkin, B. Gurney, D. Wilhoit, D. Mauri, Giant magnetoresistive in soft ferromagnetic multilayers, Phys. Rev. B. 43 (1991) 1297–1300. doi:10.1103/PhysRevB.43.1297.

[59] J.C.S. Kools, Exchange-biased spin-valves for magnetic storage, IEEE Trans. Magn. 32 (1996) 3165–3184. doi:10.1109/20.508381.

[60] B. Dieny, V.S. Speriosu, B. a. Gurney, S. Parkin, D.R. Wilhoit, K.P. Roche, et al., Spin-valve effect in soft ferromagnetic sandwiches, J. Magn. Magn. Mater. 93 (1991) 101–104. doi:10.1016/0304-8853(91)90311-W.

[61] http://www-03.ibm.com/ibm/history/exhibits/storage/storage_350.html.

[62] http://royal.pingdom.com/2010/02/18/amazing-facts-and-figures-about-the-evolution-of-hard-disk-drives/.

[63] No Title, (n.d.). http://fr.leawo.com/knowledge/sd-card-backup-micro-sd-card-recovery.html.

[64] E. Grochowski, R.D. Halem, Technological impact of magnetic hard disk drives on storage systems, IBM Syst. J. 42 (2003) 338–346. doi:10.1147/sj.422.0338.

[65] S. Parkin, Z.G. Li, D.J. Smith, Giant magnetoresistance in antiferromagnetic Co/Cu multilayers, Appl. Phys. Lett. 58 (1991) 2710. doi:10.1063/1.104765.

[66] M. Takagishi, K. Koi, M. Yoshikawa, T. Funayama, H. Iwasaki, M. Sahashi, The applicability of CPP-GMR heads for magnetic recording, IEEE Trans. Magn. 38 (2002) 2277–2282. doi:10.1109/TMAG.2002.802804.

[67] L. Savtchenko, B.N. Engel, N.D. Rizzo, M.F. DeHerrera, J.A. Janesky, No Title, 6 545 906 B1, 2003.

[68] D.C. Worledge, Spin flop switching for magnetic random access memory, Appl. Phys. Lett. 84 (2004) 4559. doi:10.1063/1.1759376.

[69] B.N. Engel, J. Akerman, B. Butcher, R.W. Dave, M. DeHerrera, M. Durlam, et al., A 4-Mb toggle MRAM based on a novel bit and switching method, IEEE Trans. Magn. 41 (2005) 132–136. doi:10.1109/TMAG.2004.840847.

[70] J.C. Slonczewski, Current-driven excitation of magnetic multilayers, J. Magn. Magn. Mater. 159 (1996) L1–L7. doi:10.1016/0304-8853(96)00062-5.

[71] L. Berger, Emission of spin waves by a magnetic multilayer traversed by a current, Phys. Rev. B. 54 (1996) 9353–9358. doi:10.1103/PhysRevB.54.9353.

[72] Y. Huai, F. Albert, P. Nguyen, M. Pakala, T. Valet, Observation of spin-transfer switching in deep submicron-sized and low-resistance magnetic tunnel junctions, Appl. Phys. Lett. 84 (2004) 3118. doi:10.1063/1.1707228.

[73] F.J. Albert, J. a. Katine, R. a. Buhrman, D.C. Ralph, Spin-polarized current switching of a Co thin film nanomagnet, Appl. Phys. Lett. 77 (2000) 3809. doi:10.1063/1.1330562.

[74] Y. Huai, M. Pakala, Z. Diao, Y. Ding, Spin transfer switching current reduction in magnetic tunnel junction based dual spin filter structures, Appl. Phys. Lett. 87 (2005) 222510. doi:10.1063/1.2138363.

[75] M. Nakayama, T. Kai, N. Shimomura, M. Amano, E. Kitagawa, T. Nagase, et al., Spin transfer switching in TbCoFe⁄CoFeB⁄MgO⁄CoFeB⁄TbCoFe magnetic tunnel junctions

with perpendicular magnetic anisotropy, J. Appl. Phys. 103 (2008) 07A710. doi:10.1063/1.2838335.

[76] S. Ikeda, K. Miura, H. Yamamoto, K. Mizunuma, H.D. Gan, M. Endo, et al., A perpendicular-anisotropy CoFeB-MgO magnetic tunnel junction., Nat. Mater. 9 (2010) 721–4. doi:10.1038/nmat2804.

[77] L.E. Nistor, B. Rodmacq, S. Auffret, A. Schuhl, M. Chshiev, B. Dieny, Oscillatory interlayer exchange coupling in MgO tunnel junctions with perpendicular magnetic anisotropy, Phys. Rev. B. 81 (2010) 220407. doi:10.1103/PhysRevB.81.220407.

[78] K. Ando, S. Fujita, J. Ito, S. Yuasa, Y. Suzuki, Y. Nakatani, et al., Spin-transfer torque magnetoresistive random-access memory technologies for normally off computing (invited), J. Appl. Phys. 115 (2014) 172607. doi:10.1063/1.4869828.

[79] I.L. Prejbeanu, W. Kula, K. Ounadjela, R. Sousa, O. Redon, B. Dieny, et al., Thermally Assisted Switching in Exchange-Biased Storage Layer Magnetic Tunnel Junctions, IEEE Trans. Magn. 40 (2004) 2625–2627. doi:10.1109/TMAG.2004.830395.

[80] M. Kerekes, R.C. Sousa, I.L. Prejbeanu, O. Redon, U. Ebels, C. Baraduc, et al., Dynamic heating in submicron size magnetic tunnel junctions with exchange biased storage layer, J. Appl. Phys. 97 (2005) 10P501. doi:10.1063/1.1850392.

[81] J.M. Daughton, a. V. Pohm, Design of Curie point written magnetoresistance random access memory cells, J. Appl. Phys. 93 (2003) 7304. doi:10.1063/1.1557373.

[82] I.L. Prejbeanu, S. Bandiera, J. Alvarez-Hérault, R. Sousa, B. Dieny, J.P. Nozières, Thermally assisted MRAMs: ultimate scalability and logic functionalities, J. Phys. D. Appl. Phys. 46 (2013) 074002. doi:10.1088/0022-3727/46/7/074002.

[83] H. Meng, J. Wang, Z. Diao, J.-P. Wang, Low resistance spin-dependent magnetic tunnel junction with high breakdown voltage for current-induced-magnetization-switching devices, J. Appl. Phys. 97 (2005) 10C926. doi:10.1063/1.1857651.

[84] J. Wang, P.P. Freitas, E. Snoeck, Low-resistance spin-dependent tunnel junctions with ZrAlO[sub x] barriers, Appl. Phys. Lett. 79 (2001) 4553. doi:10.1063/1.1428111.

[85] C. Shang, Y. Chen, K. Moon, Kinetics of pinhole nucleation and growth in magnetic tunnel junctions, J. Appl. Phys. 93 (2003) 7017. doi:10.1063/1.1555291.

[86] L. Berger, Multilayer configuration for experiments of spin precession induced by a dc current, J. Appl. Phys. 93 (2003) 7693. doi:10.1063/1.1555771.

[87] H. Kano, K. Bessho, Y. Higo, K. Ohba, M. Hashimoto, T. Mizuguchi, et al., MRAM with improved magnetic tunnel junction material, in: IEEE Int. Dig. Tech. Pap. Magn. Conf., IEEE, 1996: p. BB4. doi:10.1109/INTMAG.2002.1000779.

[88] E. Myers, F. Albert, J. Sankey, E. Bonet, R. Buhrman, D. Ralph, Thermally Activated Magnetic Reversal Induced by a Spin-Polarized Current, Phys. Rev. Lett. 89 (2002) 196801. doi:10.1103/PhysRevLett.89.196801.

[89] G.I.R. Anderson, H.-X. Wei, N. a. Porter, V. Harnchana, a. P. Brown, R.M.D. Brydson, et al., Changes in the layer roughness and crystallography during the annealing of CoFeB/MgO/CoFeB magnetic tunnel junctions, J. Appl. Phys. 105 (2009) 063904. doi:10.1063/1.3081652.

[90] J.P. Nozières, S. Jaren, Y.B. Zhang, A. Zeltser, K. Pentek, V.S. Speriosu, Blocking temperature distribution and long-term stability of spin-valve structures with Mn-based antiferromagnets, J. Appl. Phys. 87 (2000) 3920. doi:10.1063/1.372435.

[91] G.W. Anderson, Y. Huai, M. Pakala, Spin-valve thermal stability: The effect of different antiferromagnets, J. Appl. Phys. 87 (2000) 5726. doi:10.1063/1.372502.

[92] K. Imakita, M. Tsunoda, M. Takahashi, Thickness dependence of exchange anisotropy of polycrystalline Mn[sub 3]Ir/Co-Fe bilayers, J. Appl. Phys. 97 (2005) 10K106. doi:10.1063/1.1850858.

[93] V. Baltz, Antiferromagnets for spintronics: exchange bias, spin dependent transport, HDR Thesis (*Habilitation à diriger des recherches*), 2014.

[94] S. a Wolf, D.D. Awschalom, R. a Buhrman, J.M. Daughton, S. von Molnár, M.L. Roukes, et al., Spintronics: a spin-based electronics vision for the future., Science. 294 (2001) 1488–95. doi:10.1126/science.1065389.

[95] L.G. Harrison, Influence of dislocations on diffusion kinetics in solids with particular reference to the alkali halides, Trans. Faraday Soc. 57 (1961) 1191. doi:10.1039/tf9615701191.

[96] M. Ohring, Materials Science of Thin Films, Elsevier, 2002. doi:10.1016/B978-012524975-1/50014-8.

[97] D.J. Larson, E. a. Marquis, P.M. Rice, T.J. Prosa, B.P. Geiser, S.-H. Yang, et al., Manganese diffusion in annealed magnetic tunnel junctions with MgO tunnel barriers, Scr. Mater. 64 (2011) 673–676. doi:10.1016/j.scriptamat.2010.12.021.

[98] C.S. Yoon, J.H. Lee, H.D. Jeong, C.K. Kim, J.H. Yuh, R. Haasch, Diffusion study of the exchange-biased NiFe/MnIr/CoFe electrode in magnetic tunnel junctions, Appl. Phys. Lett. 80 (2002) 3976. doi:10.1063/1.1481185.

[99] J.H. Lee, H.D. Jeong, C.S. Yoon, C.K. Kim, B.G. Park, T.D. Lee, Interdiffusion in antiferromagnetic/ferromagnetic exchange coupled NiFe/IrMn/CoFe multilayer, J. Appl. Phys. 91 (2002) 1431. doi:10.1063/1.1427400.

[100] B. Gault, F. Vurpillot, A. Vella, M. Gilbert, A. Menand, D. Blavette, et al., Design of a femtosecond laser assisted tomographic atom probe, Rev. Sci. Instrum. 77 (2006) 043705. doi:10.1063/1.2194089.

[101] D.J. Larson, A.K. Petford-Long, Y.. Ma, A. Cerezo, Information storage materials: nanoscale characterisation by three-dimensional atom probe analysis, Acta Mater. 52 (2004) 2847–2862. doi:10.1016/j.actamat.2004.03.015.

[102] A. Cerezo, P.H. Clifton, M.J. Galtrey, C.J. Humphreys, T.F. Kelly, D.J. Larson, et al., Atom probe tomography today, Mater. Today. 10 (2007) 36–42. doi:10.1016/S1369-7021(07)70306-1.

[103] D.N. Seidman, Perspective: From field-ion microscopy of single atoms to atom-probe tomography: A journey: “Atom-probe tomography” [Rev. Sci. Instrum. 78, 031101 (2007)]., Rev. Sci. Instrum. 78 (2007) 030901. doi:10.1063/1.2716503.

[104] C.B. Ene, G. Schmitz, R. Kirchheim, A. Hütten, Stability and thermal reaction of GMR NiFe/Cu thin films, Acta Mater. 53 (2005) 3383–3393. doi:10.1016/j.actamat.2005.03.038.

[105] T. Li, P.A.J. Bagot, E.A. Marquis, S.C.E. Tsang, G.D.W. Smith, Characterization of Oxidation and Reduction of Pt–Ru and Pt–Rh–Ru Alloys by Atom Probe Tomography and Comparison with Pt–Rh, J. Phys. Chem. C. 116 (2012) 17633–17640. doi:10.1021/jp304359m.

[106] A. Zarefy, L. Lechevallier, R. Lardé, H. Chiron, J.-M. Le Breton, V. Baltz, et al., Influence of Co layer thickness on the structural and magnetic properties of (Pt/Co(tCo)3/Pt(tPt)/IrMn multilayers, J. Phys. D. Appl. Phys. 43 (2010) 215004. doi:10.1088/0022-3727/43/21/215004.

[107] F. Letellier, V. Baltz, L. Lechevallier, R. Lardé, J.-F. Jacquot, B. Rodmacq, et al., Effects of sputter-deposition-induced and post-deposition thermally activated intermixing on the exchange bias properties of [Pt/Co] ×3 /(Pt)/IrMn films, J. Phys. D. Appl. Phys. 45 (2012) 275001. doi:10.1088/0022-3727/45/27/275001.

[108] a. Zarefy, R. Lardé, L. Lechevallier, F. Cuvilly, J.M. Le Breton, V. Baltz, et al., Characterization of (Pt[sub 2 nm]/Co[sub 0.4 nm])[sub 3]/Pt[sub x]/IrMn[sub 7 nm] multilayers by tomographic atom probe: On the role of a Pt spacer, J. Appl. Phys. 105 (2009) 103912. doi:10.1063/1.3125527.

[109] R.M. Bozorth, Magnetism, D. Van Nostrand Company INC, 1951.

[110] R. Lardé, L. Lechevallier, A. Zarefy, A. Bostel, J. Juraszek, J.M. Le Breton, et al., Structural analysis of a (Pt/Co)[sub 3]/IrMn multilayer: Investigation of sub-nanometric layers by tomographic atom probe, J. Appl. Phys. 105 (2009) 084307. doi:10.1063/1.3106636.

[111] L. Lechevallier, A. Zarefy, F. Letellier, R. Lardé, D. Blavette, J.M. Le Breton, et al., Temperature stability of (Pt/Co)3/IrMn multilayers, J. Appl. Phys. 112 (2012) 043904. doi:10.1063/1.4745033.

[112] M.-A. Nicolet, Diffusion barriers in thin films, Thin Solid Films. 52 (1978) 415–443. doi:10.1016/0040-6090(78)90184-0.

[113] S. Song, Y. Liu, M. Li, D. Mao, C. Chang, H. Ling, Diffusion barrier performance of W/Ta–W–N double layers for Cu metallization, Microelectron. Eng. 83 (2006) 423–427. doi:10.1016/j.mee.2005.11.005.

[114] M.-G. Sung, Y.S. Kim, S.J. Kim, I.-K. Jeong, H.-S. Choi, M.-S. Kim, et al., Low resistive tungsten dual poly-metal gates with multi-diffusion barrier metals in high performance memory devices, Solid. State. Electron. 69 (2012) 22–26. doi:10.1016/j.sse.2011.09.003.

[115] X.W. Zhou, H.N.G. Wadley, R.A. Johnson, D.J. Larson, N. Tabat, A. Cerezo, et al., Atomic scale structure of sputtered metal multilayers, Acta Mater. 49 (2001) 4005–4015. doi:10.1016/S1359-6454(01)00287-7.

[116] D. Kaya, P.N. Lapa, P. Jayathilaka, H. Kirby, C.W. Miller, I. V. Roshchin, Controlling exchange bias in FeMn with Cu, J. Appl. Phys. 113 (2013) 17D717. doi:10.1063/1.4798310.

[117] P. Gibbs, T.M. Harders, J.H. Smith, The magnetic phase diagram of CuMn, J. Phys. F Met. Phys. 15 (1985) 213–223. doi:10.1088/0305-4608/15/1/022.

[118] R.K. Chouhan, A. Mookerjee, Magnetic phase diagram for CuMn, J. Magn. Magn. Mater. 323 (2011) 868–873. doi:10.1016/j.jmmm.2010.11.070.

[119] N. Gökemeijer, T. Ambrose, C. Chien, Long-Range Exchange Bias across a Spacer Layer, Phys. Rev. Lett. 79 (1997) 4270–4273. doi:10.1103/PhysRevLett.79.4270.

[120] V. Baltz, B. Dieny, Influence of Pt as Mn diffusion barrier on the distribution of blocking temperature in Co/(Pt)/IrMn exchange biased layers, J. Appl. Phys. 109 (2011) 066102. doi:10.1063/1.3558983.

[121] S. Bandiera, R.C. Sousa, B. Rodmacq, B. Dieny, Enhancement of perpendicular magnetic anisotropy through reduction of Co-Pt interdiffusion in (Co/Pt) multilayers, Appl. Phys. Lett. 100 (2012) 142410. doi:10.1063/1.3701585.

[122] V. Baltz, S. Auffret, B. Dieny, Effect of Top, Bottom, On- and Off-Axis Deposition on the Blocking Temperature Distributions of Exchange Biased Bilayers, IEEE Trans. Magn. 47 (2011) 3308–3311. doi:10.1109/TMAG.2011.2149502.

[123] Y.J. Wang, Some interesting behaviors observed in nanostructured magnetic multilayers with alloy spacers, Appl. Phys. A Mater. Sci. Process. 68 (1999) 231–238. doi:10.1007/s003390050881.

[124] P. Bruno, C. Chappert, Ruderman-Kittel theory of oscillatory interlayer exchange coupling, Phys. Rev. B. 46 (1992) 261–270. doi:10.1103/PhysRevB.46.261.

[125] J. Bass, W.P. Pratt, Spin-diffusion lengths in metals and alloys, and spin-flipping at metal/metal interfaces: an experimentalist's critical review, J. Phys. Condens. Matter. 19 (2007) 183201. doi:10.1088/0953-8984/19/18/183201.

[126] J.H. Lee, S.J. Kim, C.S. Yoon, C.K. Kim, B.G. Park, T.D. Lee, Thermal stability of the exchanged biased CoFe/IrMn electrode for the magnetic tunnel junction as a function of CoFe thickness, J. Appl. Phys. 92 (2002) 6241. doi:10.1063/1.1516623.

[127] J. Cai, W. Lai, J. Teng, F. Shen, Z. Zhang, L. Mei, Long-range oscillatory exchange interaction between antiferromagnetic FeMn layers across a Cu spacer, Phys. Rev. B. 70 (2004) 214428. doi:10.1103/PhysRevB.70.214428.

[128] Y.-Y. Song, D.-H. Kim, S.-C. Yu, P.D. Kim, I.A. Turpanov, L.A. Lee, et al., Observation of nonmonotonic oscillatory interlayer exchange coupling in Co∕Cu∕CoO films with varying Cu spacer thickness, J. Appl. Phys. 103 (2008) 07C112. doi:10.1063/1.2831390.

[129] A. Paul, N. Paul, J. Jutimoosik, R. Yimnirun, S. Rujirawat, B. Höpfner, et al., Change in interface magnetism of an exchange-coupled system due to the presence of nonmagnetic spacers, Phys. Rev. B. 87 (2013) 014431. doi:10.1103/PhysRevB.87.014431.

[130] A. Paul, D.E. Bürgler, M. Luysberg, P. Grünberg, Enhanced exchange bias due to an ultra-thin, non-magnetic insulator spacer layer, Europhys. Lett. 68 (2004) 233–239. doi:10.1209/epl/i2003-10312-y.

[131] D.D. Djayaprawira, K. Tsunekawa, M. Nagai, H. Maehara, S. Yamagata, N. Watanabe, et al., 230% room-temperature magnetoresistance in CoFeB∕MgO∕CoFeB magnetic tunnel junctions, Appl. Phys. Lett. 86 (2005) 092502. doi:10.1063/1.1871344.

[132] T. Takeuchi, K. Tsunekawa, Y. Choi, Y. Nagamine, D.D. Djayaprawira, A. Genseki, et al., Crystallization of Amorphous CoFeB Ferromagnetic Layers in CoFeB/MgO/CoFeB Magnetic Tunnel Junctions, Jpn. J. Appl. Phys. 46 (2007) L623–L626. doi:10.1143/JJAP.46.L623.

[133] Y.-H. Wang, W.-C. Chen, S.-Y. Yang, K.-H. Shen, C. Park, M.-J. Kao, et al., Interfacial and annealing effects on magnetic properties of CoFeB thin films, J. Appl. Phys. 99 (2006) 08M307. doi:10.1063/1.2176108.

[134] Y.M. Lee, J. Hayakawa, S. Ikeda, F. Matsukura, H. Ohno, Giant tunnel magnetoresistance and high annealing stability in CoFeB∕MgO∕CoFeB magnetic tunnel

junctions with synthetic pinned layer, Appl. Phys. Lett. 89 (2006) 042506. doi:10.1063/1.2234720.

[135] L. Lombard, E. Gapihan, R.C. Sousa, Y. Dahmane, Y. Conraux, C. Portemont, et al., IrMn and FeMn blocking temperature dependence on heating pulse width, J. Appl. Phys. 107 (2010) 09D728. doi:10.1063/1.3340452.

[136] C. Papusoi, R. Sousa, B. Dieny, I.L. Prejbeanu, Y. Conraux, K. Mackay, et al., Reversing exchange bias in thermally assisted magnetic random access memory cell by electric current heating pulses, J. Appl. Phys. 104 (2008) 013915. doi:10.1063/1.2951931.

[137] M.J. Carey, A. Kellock, L. Baril, J.R. Childress, T. Le, T. Thompson, et al., Improved corrosion resistance of IrMn by Cr and Ru additions, Appl. Phys. Lett. 81 (2002) 5198. doi:10.1063/1.1526910.

[138] T. Ohtsu, K. Kataoka, M. Torigoe, H. Tanaka, S. Sasaki, D. Hsiao, et al., Robustness Under Mechanical Stress of IrMnCr Heads, IEEE Trans. Magn. 43 (2007) 2211–2213. doi:10.1109/TMAG.2007.894342.

[139] B. Dai, J.W. Cai, W.Y. Lai, Y.Z. Liu, Z. Zhang, F.B. Meng, et al., Large enhancement of exchange bias in CoFe⁄CrPt films through interfacial Mn addition, J. Appl. Phys. 99 (2006) 073902. doi:10.1063/1.2185830.

[140] G.W. Anderson, Y. Huai, Spin valves exchange biased by IrMn/PtMn laminated antiferromagnets, J. Appl. Phys. 87 (2000) 4924. doi:10.1063/1.373204.

[141] S.-S. Lee, Exchange biasing field of NiFe/[IrMn–Mn]/CoFe multilayers depending on Mn content, J. Appl. Phys. 95 (2004) 7525. doi:10.1063/1.1676035.

[142] T. Yamaoka, M. Mekata, H. Takaki, Neutron Diffraction Study of Antiferromagnetism in Face-Centered Cubic Mn-Ir Alloys, J. Phys. Soc. Japan. 31 (1971) 301–301. doi:10.1143/JPSJ.31.301.

[143] Y. Endoh, Y. Ishikawa, Antiferromagnetism of γ Iron Manganes Alloys, J. Phys. Soc. Japan. 30 (1971) 1614–1627. doi:10.1143/JPSJ.30.1614.

[144] P.F. Ladwig, Y.A. Chang, E.S. Linville, A. Morrone, J. Gao, B.B. Pant, et al., Paramagnetic to antiferromagnetic phase transformation in sputter deposited Pt–Mn thin films, J. Appl. Phys. 94 (2003) 979. doi:10.1063/1.1587266.

[145] J. Ventura, J.P. Araujo, J.B. Sousa, A. Veloso, P.P. Freitas, Distribution of blocking temperatures in nano-oxide layers of specular spin valves, J. Appl. Phys. 101 (2007) 113901. doi:10.1063/1.2736290.

[146] Z.M. Zeng, P. Khalili Amiri, G. Rowlands, H. Zhao, I.N. Krivorotov, J.-P. Wang, et al., Effect of resistance-area product on spin-transfer switching in MgO-based magnetic

tunnel junction memory cells, Appl. Phys. Lett. 98 (2011) 072512. doi:10.1063/1.3556615.

[147] Z. Diao, Z. Li, S. Wang, Y. Ding, A. Panchula, E. Chen, et al., Spin-transfer torque switching in magnetic tunnel junctions and spin-transfer torque random access memory, J. Phys. Condens. Matter. 19 (2007) 165209. doi:10.1088/0953-8984/19/16/165209.

[148] S. Fukami, H. Honjo, T. Suzuki, N. Ishiwata, Reduction of Writing Field Distribution in a Magnetic Random Access Memory With Toggle Switching, IEEE Trans. Magn. 43 (2007) 3512–3516. doi:10.1109/TMAG.2007.900573.

[149] Y. Hao, F.J. Castaño, C. a. Ross, B. Vögeli, M.E. Walsh, H.I. Smith, Magnetization reversal in lithographically patterned sub-200-nm Co particle arrays, J. Appl. Phys. 91 (2002) 7989. doi:10.1063/1.1453320.

[150] a. Fernandez, M.. Gibbons, M.. Wall, C.. Cerjan, Magnetic domain structure and magnetization reversal in submicron-scale Co dots, J. Magn. Magn. Mater. 190 (1998) 71–80. doi:10.1016/S0304-8853(98)00267-4.

[151] J.F. Smyth, S. Schultz, D.R. Fredkin, D.P. Kern, S. a. Rishton, H. Schmid, et al., Hysteresis in lithographic arrays of permalloy particles: Experiment and theory (invited), J. Appl. Phys. 69 (1991) 5262. doi:10.1063/1.348071.

[152] J. Gadbois, J.-G. Zhu, W. Vavra, A. Hurst, The effect of end and edge shape on the performance of pseudo-spin valve memories, IEEE Trans. Magn. 34 (1998) 1066–1068. doi:10.1109/20.706358.

[153] R.P. Cowburn, D.K. Koltsov, a. O. Adeyeye, M.E. Welland, Lateral interface anisotropy in nanomagnets, J. Appl. Phys. 87 (2000) 7067. doi:10.1063/1.372933.

[154] J.G. Deak, R.. Koch, The effect of edge roughness on magnetization reversal in micron-sized permalloy thin films, J. Magn. Magn. Mater. 213 (2000) 25–31. doi:10.1016/S0304-8853(99)00603-4.

[155] Y. Katoh, S. Saito, H. Honjo, R. Nebashi, N. Sakimura, T. Suzuki, et al., Analysis of MTJ Edge Deformation Influence on Switching Current Distribution for Next-Generation High-Speed MRAMs, IEEE Trans. Magn. 45 (2009) 3804–3807. doi:10.1109/TMAG.2009.2022336.

# Glossary – acronyms and abbreviations

| | |
|---|---|
| EB | exchange bias |
| F | ferromagnet |
| AF | antiferromagnet |
| FC | field cooling |
| T | temperature |
| $T_N$ | Néel temperature |
| $T_B$ | blocking temperature |
| $DT_B$ | blocking temperature distribution |
| $T_M$ | measurement temperature |
| $T_a$ | annealing temperature |
| $T_{init}$ | initial field cooling temperature |
| TRM | thermoremanent moment |
| GMR | giant magnetoresistance |
| TMR | tunnel magnetoresistance |
| MRAM | magnetic random access memory |
| TA- | thermally assisted- |
| VSM | vibrating sample magnetometer |
| APT | atom probe tomography |
| CDF | cumulative distribution function |
| RA - | resistance area |
| FIMS | field induced magnetic switching |
| CIMS | current induced magnetic switching |
| rest-T | normal operation temperature (writing not involved) |
| STT | spin transfer torque |
| SW | Stoner-Wohlfarth |
| SG | spin-glass |
| HDD | hard disk drive |
| NM | non-magnetic |

# Appendices

## Appendix 1: using single barrier to the diffusion of Mn

As it was discussed in (Chapter 3.1) the Mn diffusion is one of the reasons of interfacial spin-glass formation. At this section the former study of the diffusion barriers is presented. Prior to the dual barriers (Chapter 3.2.1) examination the various materials of different nature were deposited between F and AF layer. In this investigation we employed $DT_B$ procedure to quantify the effectiveness of these materials as a Mn diffusion barriers.

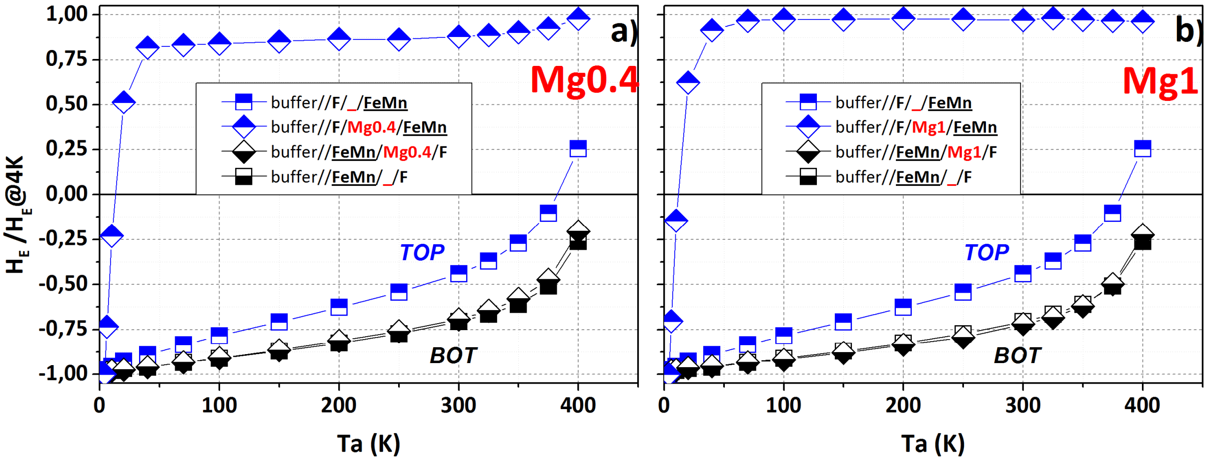

**Figure. 1**

*Blocking temperature distributions after an initial FC from* $T_{init}$ *= 300°C. Rectangles stand for the base compositions with FeMn as AF-material: Ta (5 nm)/Cu (3 nm)/FeMn (12 nm)/ Mg (*$t_{Mg}$*) /NiFe (3 nm)/Ta (0.2 nm)/CoFeB (2 nm)/Mg (1.7 nm)/Ta (5 nm) and reversed Ta (5 nm)/Mg (1.6 nm)/CoFeB (2 nm)/Ta (0.2 nm)/NiFe (3 nm)/ Mg (*$t_{Mg}$*) /FeMn (12 nm)/ Ta (5nm). Additionally to the base-stack, in a) Mg 0.4 nm and b) Mg 1 nm are inserted between F and AF layers (diamonds).*

For this study there were prepared 2 series of stacks deposited by dc magnetron sputtering on Si/SiO2 substrates in the atmosphere of Ar at the level of 2.5 $10^{-3}$ mbar pressure at the rate of between 0.05 and 0.1 nm $s^{-1}$: Ta (5nm)/ Cu (3nm)/ AF / X($t_X$) / NiFe

(3nm)/ Ta (0.2nm) /CoFeB (2nm)/Mg (1.7nm)/Ta (5nm) and reversed Ta (5nm)/ Mg (1.6nm)/ CoFeB (2nm)/ Ta (0.2nm)/NiFe (3nm)/X ($t_X$)/ AF /Ta (5nm) for bottom and top configurations respectively. For the barrier (X) the following materials were selected: CoSi, Ru, Cu, Ta and Mg with 2 fixed thicknesses ($t_X$) equal to 0.4 and 1nm. IrMn 6.5nm and FeMn 12nm were chosen as AF materials. Post deposition annealing in magnetic field of 1.5 kOe at 300°C during 1h was performed. Altering the relative deposition between F and AF layers (so-called top and bottom configuration) and the AF material itself allowed us to account for diverse conditions responsible for EB degradation, but not only the barrier effect.

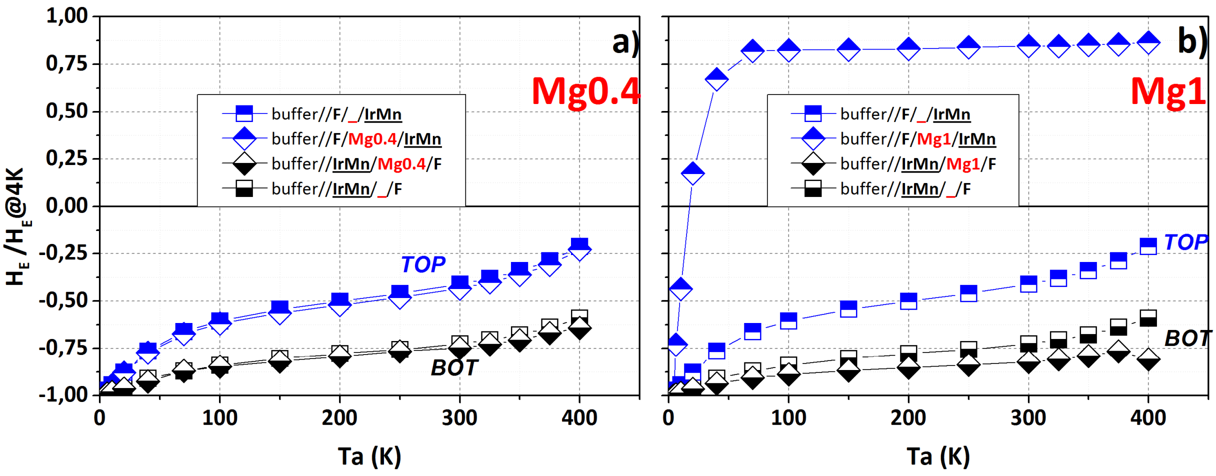

**Figure.2**

*Same as Figure 1 but with IrMn instead of FeMn as AF-material.*

In the all presented figures in this appendix we compare the $DT_B$ curves for the top and bottom base-stacks (i.e. without spacers) plotted with the square symbols, and corresponding samples with inserted Mg barrier, shown in diamonds. The symbols are half-filled with the colour to indicate the mutual orientation of F and AF layers, hence top-filled diamond/rectangle indicates the AF deposited on top of F and vice versa. Actually here the curves are plotted only for the Mg spacer families, even the total number of examined spacers equals to five. We did so because of two reasons – first, Mg barrier shows the trend, common to all measured samples with sufficient magnetic signal and consequently to avoid repetitions the Mg stacks were chosen as representatives. Also, prior to the full $DT_B$ procedure, all samples were measured at RT. Those, the loop shift of which was negligible were discarded due to the very low signal and therefore impossibility to quantify the interfacial quality. To evidence the reasons of vanished EB for the rest samples the deep structural study is required, which is far out of the scope of our study. Nevertheless, such well-known mechanisms as growth of the AF and intensive diffusion are the most probable reasons of the EB loss. For example 0.2nm of the Ta spacer sufficiently decreased the migration of Mn at as-deposited state [A1] (the references for the appendices comes separately at the end), but after annealing the diffusion was evidenced and also showed the discrepancy between top and bottom samples. In our case, twice as thick 0.4nm Ta spacer led to EB vanishing. On Figure 1 the typical distribution for the top/bottom compositions without (square symbols) and with insertion of 0.4 nm Figure 1a) and 1nm Figure 1b) of Mg are shown with FeMn as an AF. First, it is important to note that the both samples without a diffusion barrier (square symbols) already show the discrepancy with top AF configuration having the higher amplitude than the bottom one. This behaviour is more likely related with the growth conditions of the AF, as it will be detailed lately. Now, focusing at the curves for samples with a barrier, the significant difference occurs between the shapes of the top and bottom structures. The drastic change of EB when the FeMn is deposited on top of Mg holds for both thicknesses and is more likely can be explained in terms of crystallography – the loop shift is strongly affected by crystal orientation [A2,A3]. Mg as a seed layer seems to not provide the proper texture to the growth for the FeMn antiferromagnetic order which is sensitive even on the deposition conditions. Contrary to the top orientation, the barrier inserted in the bottom structures does not reflect any changes for the interfacial quality. Indeed, the two black curves (Figure 1(a-b)) with the square and diamond symbols are almost overlapping, thus signifying no significant changes in the interfacial quality. Actually, this trend holds for all revised spacers and is in agreement with previous findings in the literature [A4].

Slightly different behaviour was observed for IrMn-based AF. The $DT_B$ are shown on the Figure 2 (a-b), and the colour code with squares for base structure and diamonds for the barriers is kept in the same manner as in Figure 1. Contrary to FeMn, the insertion of 0.4 nm Mg Figure 2(a) does not impact on the neither of structures, which is reflected on the almost aligned curves with the base structures. Nevertheless, a very similar picture occurs with 1nm Mg barrier. Now, the sharp drop in EB is clearly observed for the top AF stack. As it was noticed for the FeMn the difference occurs already for the samples without any barriers inserted between top and bottom stacks, for IrMn it is also the case. Even if IrMn was more robust for thin insertion of Mg, if the interlayer is sufficiently thick, it also reflects on its growth that has been extensively studied [A5]. Analysing $DT_B$ for the bottom compositions, the Mg insertions 0.4nm (Figure 2(a)) did not show a sufficient improvement. Nevertheless the discrepancy is clearly visible for the thicker 1nm-thick interlayer (Figure 2(b)), while the curve for thinner one is almost overlapping with the base sample stack without spacer. An attempt to further increase Mg barrier thickness led to the vanishing of EB, most probably due to the augmentation between the F and AF layers. To conclude, this appendix showed the great importance of materials choice for the proper implementation in EB structures (e.g. see the dual barrier study in the main text).

# Appendix 2: tuning the interface vs volume contributions via ion irradiations

The aim of the study was to modify the interface vs volume atomic arrangements by means of $He^+$ irradiations at various energies and fluences and probe its influence on the glassy spin character of the interface by means of bimodal distributions of blocking temperature measurements.

In 1998 Chappert et al. [A6] has shown an encouraging study of materials magnetic properties before and after irradiation by He ions. It was evidenced, that changing the irradiation fluence the material magnetic anisotropy can be gradually reduced up to paramagnetic state. This observation raised an incremental interest on irradiations technique as a new possible approach for sub-micron magnetic media patterning [A7]. Lately, the EB structures have been studied, showing the possibility of coercitivity and exchange field tailoring via appropriately chosen irradiation energies and fluences.

From our part, the main interest was concluded in probing this technique to correlate the possible interfacial quality [A8] variation in EB sandwiches with various degree of He ions energies and doses. This was done in collaboration with the Dresden Forschungszentrum Rossendorf and the LPS Orsay, who performed the $He^+$ ion irradiations. For these purposes the following stack common for all the irradiation variations has been chosen: Ta (3 nm)/Cu3 (3 nm)/ IrMn (7 nm)/Co (3 mn)/Al (3 nm). The energies and the fluences of irradiation were 5; 10 and 30 keV and $10^{12}$; $10^{13}$; $10^{14}$ and $10^{15}$ $cm^{-2}$, respectively.

To estimate the energies of interest for our studies the SRIM software [A9] was used. In Figure 3 the comparison between $DT_B$ curves for not irradiated and irradiated samples at a fixed energies with variation of fluence levels are plotted. Neither the energy increase nor the fluence variation did not show any significant curve shape changes. Although the overlapping for 10 keV and 30 keV Figure 3 (b-c) is more pronounced, the more visible changes at 5 keV Figure 3a) can be observed. As it can be clearly seen from the Figure 3 a), there is no clear trend showing for example the degradation of interfacial quality (i.e. the Δ increase) with increase of the fluence or vice versa. The observed behavior looks random, since the increasing Δ obeys the following order of fluence (from Figure 3a): $10^{14}>10^{15}\sim10^{12}>$not irradiated$>10^{13}$ ions/$cm^2$. The intuitive picture of the delta as a function of irradiation influence should look like either a monotonically decreasing /or increasing (with a potential maximum / minimum at some point) with increase of fluence. The obtained values do not show stable monotonic behavior.

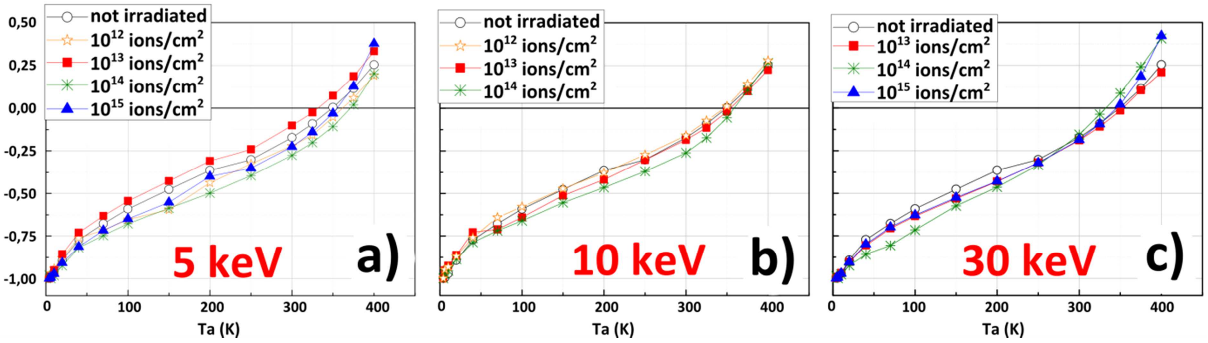

**Figure 3**

*The $DT_B$ curves for irradiated samples with varied fluences at the level of energies equal to: a) 5 keV, b) 10 keV and c) 30 keV, plotted together with not irradiated one. The symbol size corresponds to the error bar.*

As it was previously noticed, the irradiation also may lead to the structural and hence anisotropy changes in the bulk of F or AF materials [A10]. Thus, the normalized by the maximum loop shift, values do not reflect the real bulk changes, like absolute values of exchange do. Even it was slightly out of the scope of the interfacial study (because the glassy character of the interface can be hardly derived from absolute loop shift values), the aim was to get an insight on the changes (if they exist) brought to the system by $He^+$ ions. Hence, we also analyzed the variation of the loop shift at fixed temperature as illustrated in Figure 4 a) $H_E$ at 4K and potential correspondence on Figure 4 b) the amplitude (Δ) calculated at $T_m$=200K.

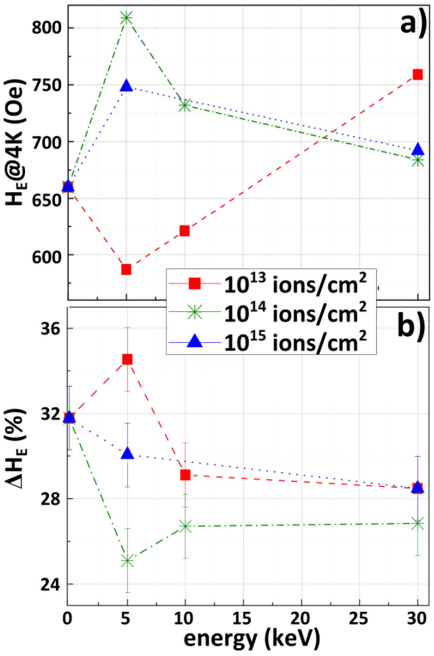

**Figure 4**

*a) Values of exchange bias at 4K for various fluences as a function of $He^+$ ions energy. b) the amplitude Δ, taken at 200K from the $DT_B$s shown on Figure 3. The zero-energy point corresponds to not-irradiated sample.*

Following the curves in Figure 4a) from zero-energy point (not irradiated sample), two different trends are observed. First, initial increase of exchange up to 5 keV as compared to not irradiated sample and following decrease for $10^{14}$ and $10^{15}$ ions/cm$^2$ fluences with higher energies. The curves representing Δ variation with the same color code on Figure 4 b) reflect these peaks with less glassy interface. Accordingly the maxim $H_E$ is obtained for $10^{14}$ ions/cm$^2$ fluence at 5 keV and showing the lowest amount of spin-glass at about of 25% level. The medium $H_E$ value corresponds to the medium among others Δ. Focusing on the red curve with rectangle symbols, the trend is almost opposite. It can be also interpreted as worsening interface with corresponding lowest $H_E$ at 5 keV, and the following improvement of both parameters with higher energies. Due to comparably small variations for the $DT_B$ curves, the above discussion is more likely an attempt of possible interpretation of the results, because there was no homogeneous and consistent trend observed and the discrepancy between two samples explanation is still lacking. Moreover, the changes in the loop shift values ($H_E$) may arise from the bulk [A11] material changes, and it is hard to conclude the exact reason of that from available information and again is out of the scope for this particular investigation. Nevertheless, the further study of irradiated EB structures may be quite promising and may include wider energy range and probably with other sample compositions. Another group though managed such a study by varying the thickness of the cap layer rather than the energy and fluence in order to tune the penetration of the ions [A15].

# Appendix 3: comparing blocking temperature distributions and dichroism results

The aim of this part is the comparison between:

- the amount of frozen spins vs MgO spacer thickness measured by XMLD in Fig. 5 of Phys. Rev. B 86, 064406 (2012) from Berkeley for Ag/ CoO 5ML/MgO tMgO/Fe 20ML //Ag(001) samples

- and the amount of unfrozen spins vs MgO spacer thickness deduced from the low-T blocking temperature distribution ($DT_B$) measured by us for MgO/ CoO 5ML/MgO tMgO/Fe 20ML //MgO(001) samples done by Berkeley

The majority part of the present manuscript employed VSM hysteresis loop measurements with a DTB procedure to quantify interfacial quality of exchange-biased bilayers. Nevertheless, this is not the only technique to obtain the information about the interfacial spins. Although less versatile, XMLD - x-ray magnetic linear dichroism [A12] allows the direct measurement of the interfacial AF spins [A13]. The recent work from Berkeley [A14] has shown an interesting result for the epitaxially grown AF CoO on Fe layer with inserted wedge-shaped MgO interlayer as shown on Figure 3 a), with the following full stack: Ag/ CoO 5ML/MgO $t_{MgO}$/Fe 20ML //Ag(001), where ML – is a monolayer.

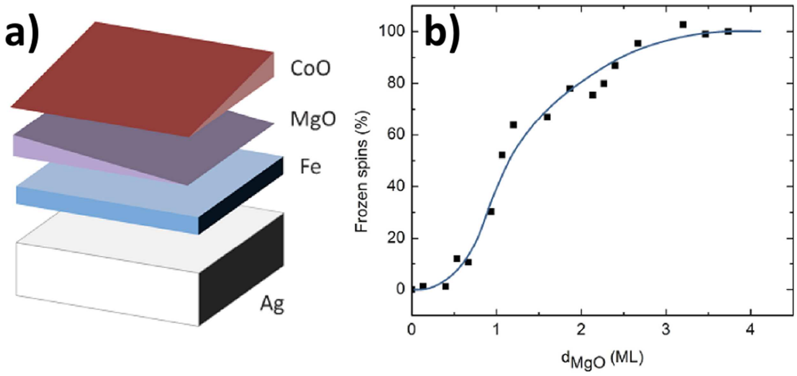

**Figure 5**

*a) Schematically shown the composition of the epitaxially grown CoO on wedge-shaped MgO interlayer. b) Frozen CoO spins with a thickness $d_{CoO}$=5 ML as a function of MgO interlayer thickness for the CoO/MgO/Fe sample structure. After* [14].

Plotted on Figure 5b) is a result of XMLD scan of frozen spins with increasing MgO interlayer thickness [A14]. As it can be seen form the curve, all the AF spins are unfrozen when the CoO is in touch with Fe layer, while gradually they are gradually getting pinned with increasing MgO spacer thickness up to 4 monolayers (ML) where they are all stable. This result encouraged us to correlate this observation with the $DT_B$ method, showing the opposite – relative quantity of unfrozen spins. Slightly modified samples were prepared by Berkeley for our studies with the stack: MgO/ CoO 5ML/MgO $t_{MgO}$/Fe 20ML //MgO(001). First, it is slightly different in composition and for us the MgO thickness was varied by steps, but not like continuous wedge, due to VSM experimental setup difference. To be able to correlate results obtained with two different experimental techniques to fulfil the curve, there were chosen the thicknesses of MgO ($t_{MgO}$) in a range from 0 to 4 ML: 0, 1.2, 2, 3 and 4 ML.

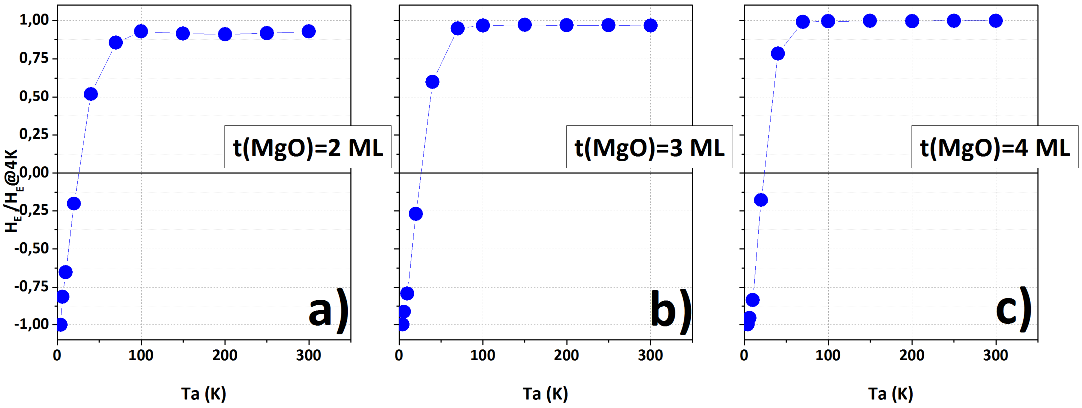

**Figure 6**

The representative $DT_B$ curves for the MgO/ CoO 5ML/MgO $t_{MgO}$/Fe 20ML //MgO(001) stacks with varied F-AF interlayer MgO thicknesses: a) 0 ML, b) 1.2 ML and c) 2 ML

On Figure 6 the selected $DT_B$s for the sample a) without and with b) 1.2 and c) 2 ML of MgO inserted, representing the trend common for all measured thicknesses. The sharp drop of $H_E$ to the opposite direction levels off at the $T_a$ around 80-90 K. It means that above this threshold there is no more contribution for the exchange since the maximum blocking temperature is reached (no more entities with higher $T_B$ contribute to the EB). This suggests, that frozen spins can be seen only within about initial 80K temperature range. It was also confirmed by zero loop shift measured at room temperature. This is however not consistent with the results from the literature. Yet, the samples are not strictly the same: Ag/ CoO 5ML/MgO tMgO/Fe 20ML //Ag(001) for the PRB vs MgO/ CoO 5ML/MgO tMgO/Fe 20ML //MgO(001) here. This may be the cause of the discrepancy and is still under consideration.

[A1] S. Cardoso, R. Ferreira, P.P. Freitas, P. Wei, J.C. Soares, Influence of Ta antidiffusion barriers on the thermal stability of tunnel junctions, Appl. Phys. Lett. 76 (2000) 3792. doi:10.1063/1.126783.

[A2] R. Jungblut, R. Coehoorn, M.T. Johnson, J. aan de Stegge, A. Reinders, Orientational dependence of the exchange biasing in molecular-beam-epitaxy-grown Ni80Fe20/Fe50Mn50 bilayers (invited), J. Appl. Phys. 75 (1994) 6659. doi:10.1063/1.356888.

[A3] H.J. Kim, J.S. Bae, T.D. Lee, H.M. Lee, Effect of sputtering condition and heat treatment in Co/Cu/Co/FeMn spin valve, J. Magn. Magn. Mater. 241 (2002) 173–178. doi:10.1016/S0304-8853(02)00025-2.

[A4] S. van Dijken, J. Moritz, J.M.D. Coey, Correlation between perpendicular exchange bias and magnetic anisotropy in IrMn⁄[Co⁄Pt][sub n] and [Pt⁄Co][sub n]⁄IrMn multilayers, J. Appl. Phys. 97 (2005) 063907. doi:10.1063/1.1861964.

[A5] J. Kanak, T. Stobiecki, S. van Dijken, Influence of Interface Roughness, Film Texture, and Magnetic Anisotropy on Exchange Bias in[Pt/Co]3 IrMn and IrMn [Co/Pt]3Multilayers, IEEE Trans. Magn. 44 (2008) 238–245. doi:10.1109/TMAG.2007.909438.

[A6] C. Chappert, Planar Patterned Magnetic Media Obtained by Ion Irradiation, Science (80-. ). 280 (1998) 1919–1922. doi:10.1126/science.280.5371.1919.

[A7] J. Fassbender, D. Ravelosona, Y. Samson, Tailoring magnetism by light-ion irradiation, J. Phys. D. Appl. Phys. 37 (2004) R179–R196. doi:10.1088/0022-3727/37/16/R01.

[A8] P.F. Carcia, S.I. Shah, W.B. Zeper, Effect of energetic bombardment on the magnetic coercivity of sputtered Pt/Co thin-film multilayers, Appl. Phys. Lett. 56 (1990) 2345. doi:10.1063/1.102912.

[A9] Z.J. F, Biersack J P, L. U, The Stopping and Range of Ions in Solids (New York: Pergamon) SRIM, (1985). http://www.srim.org/SRIM/SRIMINTRO.htm.

[A10] A. Mougin, T. Mewes, M. Jung, D. Engel, A. Ehresmann, H. Schmoranzer, et al., Local manipulation and reversal of the exchange bias field by ion irradiation in FeNi/FeMn double layers, Phys. Rev. B. 63 (2001) 060409. doi:10.1103/PhysRevB.63.060409.

[A11] P. Miltenyi, M. Gierlings, J. Keller, B. Beschoten, G. Guntherodt, U. Nowak, et al., Diluted antiferromagnets in exchange bias: proof of the domain state model, Phys. Rev. Lett. 84 (2000) 4224–7. http://www.ncbi.nlm.nih.gov/pubmed/10990651.

[A12] G. Van Der Laan, Applications of soft x-ray magnetic dichroism, J. Phys. Conf. Ser. 430 (2013) 012127. doi:10.1088/1742-6596/430/1/012127.

[A13] J. Wu, J.S. Park, W. Kim, E. Arenholz, M. Liberati, A. Scholl, et al., Direct Measurement of Rotatable and Frozen CoO Spins in Exchange Bias System of CoO/Fe/Ag(001), Phys. Rev. Lett. 104 (2010) 217204. doi:10.1103/PhysRevLett.104.217204.

[A14] A. Tan, J. Li, C.A. Jenkins, E. Arenholz, A. Scholl, C. Hwang, et al., Exchange bias in epitaxially grown CoO/MgO/Fe/Ag(001), Phys. Rev. B. 86 (2012) 064406. doi:10.1103/PhysRevB.86.064406.

[A15] A. C. Basaran, et al., Exchange bias: the antiferromagnetic bulk matters, Appl. Phys. Lett. 105 (2014) 052403. doi: 10.1063/1.4893457.

# ABSTRACT

Spintronics applications such as magnetic random access memories (MRAM), sensors (e.g.. hard disk drive read head) and logic devices use ferromagnetic/antiferromagnetic (F/AF) exchange bias (EB) interactions to set the reference direction required for the spin of conduction electrons. Thermally-assisted (TA-) MRAM applications even use two F/AF exchange biased bilayers: one for reference and one for storage. Such technological applications involve patterning full sheet wafers into matrix of individual bit-cells. Industrial products qualification imposes stringent requirements on the distributions of the magnetic properties from cell to cell, including those related to EB. It was supposed few years ago that randomly spread spin-glass like phases at the F/AF interface or within the bulk of the AF layer significantly contribute to the distributions of EB properties in devices after processing. This thesis aimed at factually studying the link between spin-glasses spread over F/AF thin films and bit-cell dispersions of EB in corresponding TA-MRAM. Prior to that the origin of the spin-glass like regions and more specifically the role of Mn-diffusion was consolidated. Mn-diffusion was directly observed, understood and the use of complex barriers to reduce such diffusion and consequently to minimize the amount of spin-glass was successfully studied. Mixing AFs as another way to tune the amount of spin-glass like phases was also evidenced in the framework of this thesis. All at once, this last solution also tuned the AF grains thermal stability and this solved another issue related to TA-MRAM, i.e. finding AF-materials with intermediate retention and write properties compared to the AFs presently used. Finally, those mixed antiferromagnets were the mean chosen to tune the amount of spin-glass like phases in real TA-MRAM devices and to factually prove their link with bit-cell distributions of EB properties.

KEYWORDS : ANTIFERROMAGNETIC MATERIALS, EXCHANGE BIAS, SPIN-GLASS, BLOCKING TEMPERATURE, BIMODAL DISTRIBUTION, NANOSTRUCTURES, THERMALLY ASSISTED MAGNETIC RANDOM ACCESS DEVICES.

---

# RESUME

Les applications d’électronique de spin telles les mémoires à accès aléatoire (MRAM), les capteurs (e.g. les têtes de lecture des disques durs d’ordinateurs) et les éléments de logique magnétique utilisent les interactions d’échange ferromagnétique/antiferromagnétique (F/AF) dans le but de définir une direction de référence pour le spin des électrons de conduction. Les MRAM à écriture assistée thermiquement (TA-MRAM) utilisent même deux bicouches F/AF : une pour le stockage de l’information et l’autre comme référence. Ces dernières applications technologiques impliquent des étapes de nanofabrication des couches minces continues pour former une matrice de cellules mémoires individuelles. La qualification industrielle du produit final impose de sérieuses contraintes sur la largeur des distributions des propriétés magnétiques - y compris d’échange F/AF - de cellule mémoire à cellule mémoire. Des phases verres de spin réparties de manière aléatoire sur la couche continue, à l’interface F/AF ou dans le cœur de l’AF pourraient contribuer de manière significative à ces distributions d’échange F/AF dans les dispositifs, après nanofabrication ; comme supposé il y a de cela quelques années. Le but de cette thèse est d’étudier factuellement le possible lien entre verre de spin répartis dans des couches minces F/AF et dispersions de propriétés d’échange de cellule mémoire à cellule mémoire dans les dispositifs TA-MRAM correspondants. Avant cela, l’origine de ces régions verre de spin a été étudiée et une attention plus particulière a été portée au rôle joué par les diffusions de Mn. Ces dernières ont été directement observées, comprises et l’utilisation de barrières complexes pour les réduire et par là même pour diminuer la quantité de phases verre de spin a été mise en œuvre avec succès. En guise d’alternative pour varier la quantité de verres de spin, l’utilisation d’AFs composites a été également étudiée dans le cadre de cette thèse. Ce type d’AF permet du même coup de varier la stabilité thermique des grains AF et de répondre à un autre problème identifié pour les TA-MRAM qui consiste à trouver des matériaux AF avec des propriétés de rétention et d’écriture intermédiaires par rapport aux matériaux actuellement utilisés. Finalement, ces AFs composites ont été utilisés comme moyen de varier la quantité de verres de spin dans des dispositifs TA-MRAM réels et de prouver le lien direct avec la dispersion de propriétés de cellule mémoire à cellule mémoire.

MOTS CLEFS : MATERIAUX ANTIFERROMAGNETIQUES, ANISOTROPIE MAGNETIQUE D’ECHANGE, VERRE DE SPIN, TEMPERATURE DE BLOCAGE, DISTRIBUTION BIMODALE, NANOSTRUCTURES, MEMOIRES MAGNETIQUES A ACCES ALEATOIRE THERMIQUEMENT ASSISTEES.